

Supermode Si/III–V Lasers and Circular Bragg Lasers

Thesis by

Xiankai Sun

In Partial Fulfillment of the Requirements for the

Degree of

Doctor of Philosophy



California Institute of Technology

Pasadena, California

2010

(Defended April 16, 2010)

© 2010

Xiankai Sun

All Rights Reserved

Thesis Committee

Professor Harry A. Atwater (Chair)

Professor Amnon Yariv

Professor Axel Scherer

Professor Kerry Vahala

Professor Bruno Crosignani

Acknowledgments

As the journey of my graduate studies comes close to the end, I find so many people who deserve my thanks as I look back.

First I would like to thank my advisor, Professor Amnon Yariv, for taking me as his student, providing a supportive environment, and enabling me to learn and explore the forefront of scientific research. His panoramic perspective of the optoelectronics research, insightful understanding of optics and physics problems, and persistent pursuit for the practical applications have always been our source of motivation and inspiration. Also, I thank Professors Harry Atwater, Axel Scherer, Kerry Vahala, and Bruno Crosignani for being part of my thesis committee, and Professor Changhuei Yang for being on my candidacy committee.

I am in debt to the postdocs and graduate students that were senior to me. Professor Koby Scheuer was my teacher who led me to the realm of research on circular Bragg lasers. Dr. John Choi trained me in the experimental, taught me how to think, and helped me hone my presentation skills. Dr. Philip Chak's deep understanding of theories and mastery of simulations were impressive, and his assistance in my Matlab coding will never be forgotten. Professors Joyce Poon and Lin Zhu were a great source of guidance and suggestions at the initial stage of my research on the supermode hybrid lasers.

I am fortunate to work with many nice collaborators on different projects. Professor Avi Zadok worked closely with me for two years on the supermode laser project. Those

happy and sad moments during the painstaking trial and error process of fabrication recipe development will forever be imprinted on my memory. A personal friend more than a collaborator, Mike Shearn of Professor Scherer's group brought into the project his unparalleled expertise on mask design, electron-beam lithography, and dry etching. His positive attitude infects everyone around him. I also owe my gratitude to Drs. Ken Diest and Marina Leite of Professor Atwater's group, who have generously taken their time doing wafer bonding for us whenever it was needed. Hsi-Chun Liu is our theory guru. Working with him has always been pleasant from studying the shortest adiabatic taper design to simulating the waveguide losses for iPhoD projects and sharing TA work for several courses. Thanks also to Mike Shearn and Dave Henry; the incredibly huge amount of work on drafting and revising an invited book chapter was only achievable through the synergy of our complementary skill set.

Of course I would not forget the help from other members of the Yariv group: Drs. Reg Lee and T. R. Chen have been excellent counselors over the years. Jacob Sendowski kindly helped in polishing my manuscript and has been a consistent source whenever I am confused with English usage. Christos Santis was my TA partner for two courses and also worked with me on the iPhoD projects for HRL Laboratories. During the past year, I have also enjoyed working with Scott Steger on further developing and expanding the scope of supermode idea. The discussions and suggestions from the "phase-locked team," Dr. Wei Liang, Naresh Satyan, and Arseny Vasilyev are acknowledged. Thanks also go to our dedicated staff, Connie Rodriguez, Ali Ghaffari, and Kevin Cooper.

I am grateful to the China Scholarship Council, the IEEE Photonics Society, and the International Society for Optical Engineering (SPIE) for supporting my graduate studies.

The work presented in this thesis was financially supported by the Natural Science Foundation (NSF) and the Defense Advanced Research Projects Agency (DARPA). The support and infrastructure provided for the experimental work in Part I of this thesis by the Kavli Nanoscience Institute at Caltech are also acknowledged.

I would also like to take this opportunity to thank my friends Dr. Yu Liu and Fan Yang, Dr. Jie Yang, and Dr. Wei Liang who kindly took me to markets for weekly grocery shopping so I was able to survive the difficult days in the first few years.

Finally, I would like to express my deepest gratitude to my parents and wife Hong Yu for their love, sacrifice, and support. They share my ups and downs, joy and sorrow, excitement and frustration. No matter where I am, no matter what I am, I know they are always by my side. Nothing I say here can match how much they have done for me, but I hope they know how appreciative I am.

Xiankai Sun

Pasadena, March 2010

Abstract

Semiconductor lasers are arguably the most important component in optical communications. This thesis investigates two types of semiconductor lasers that are useful in integrated optics. Part I focuses on supermode Si/III–V lasers and Part II discusses circular Bragg lasers for the application as surface-emitting lasers.

Just as optical fibers have largely replaced the traditional copper wires in long-distance applications, people started to consider incorporating optical communication onto chips, primarily because the increased ohmic heating and RC delay associated with the metal interconnection prevent further increase in the data-processing rate. Si is well known to be the integration platform for electronics, and III–V materials (GaAs, InP, etc.) are efficient light emitters. It is natural to bring them together to realize the on-chip optical communication. Among various Si/III–V integration schemes the most promising is the hybrid Si evanescent platform in which a wafer-bonding technique that is compatible with current CMOS processing is used to bring Si and III–V materials together. Part I of this thesis focuses on the application of a novel mode-control method to such hybrid waveguide system to enhance the modal gain, which makes for more efficient and, most importantly, shorter devices that may hold the key to the photonics/electronics integration. The supermode theory is derived, the shortest adiabatic mode transformer is theoretically and numerically studied, and the device design and fabrication are presented, followed by the

experimental demonstration of the performance enhancement in the mode-controlled Si/InGaAsP laser devices.

Vertical cavity surface emitting lasers are a commercial light source for optical communications, but their single-modedness and good emission pattern are guaranteed only over a very small mode area (diameter of several microns) thus they have limitations in high-power applications. As an alternative, circular Bragg lasers can be designed as a superior surface emitting laser that produces high output power with good beam quality. Part II of this thesis presents a comprehensive and systematic theoretical study on the surface-emitting Hankel-phased circular Bragg lasers in various geometries. The analytical and numerical mode-solving methods will be described, followed by near- and above-threshold modal analyses.

Contents

List of Figures	xii
List of Tables	xix
List of Publications	xx
Glossary of Acronyms	xxiv

Part I Supermode Si/III–V Hybrid Lasers: Theory, Design, Fabrication, and

Characterization	1
1 Introduction.....	2
1.1 Motivation of a Laser on Silicon	2
1.2 Review of Various Integration Schemes	4
1.3 Introduction of Si/III–V Evanescent Lasers	10
2 Supermode Theory	13
2.1 Derivation of Supermodes of Coupled Optical Waveguides	13
2.2 Numerical Verification of the Supermode Theory	20
2.3 Proposal of Supermode Si/III–V Lasers and Beyond	25
3 Adiabaticity Theorem and the Shortest Adiabatic Taper Design.....	30
3.1 Derivation of the Adiabaticity Criterion.....	31
3.2 Design of the Shortest Adiabatic Mode Transformer in a Coupled-Waveguide System	37

3.3 Numerical Verification.....	38
4 Device Design and Fabrication	43
4.1 Device Design	43
4.2 Device Fabrication	50
5 Experimental Characterization and Data Analysis	57
5.1 Characterization with Pulsed Current Injection	57
5.2 Continuous-Wave Operation.....	64
6 Conclusion and Outlook	68
 Part II Circular Bragg Lasers: Theory and Design for Large Area, High Power	
Surface Emission Applications.....	70
7 Introduction.....	71
8 Comprehensive Coupled-Mode Theory.....	74
8.1 Derivation of Comprehensive Coupled-Mode Theory for Circular Grating Structure in an Active Medium.....	74
8.2 Grating Design Procedure and Calculations of the Numerical Green's Function $G(z, z')$, Coefficients h_1 , h_2 , and s_1	78
9 Mode-Solving Methods	82
9.1 Analytical Mode-Solving Method	84
9.2 Numerical Mode-Solving Method	87
9.3 Mode-Solving Accuracy Check.....	88
10 Near-Threshold Modal Properties.....	90
10.1 Threshold, Frequency Detuning, and In-Plane Modal Pattern	90

10.2 Radiation Field and Far-Field Pattern.....	92
10.3 Single-Mode Range, Quality Factor, Modal Area, and Internal Emission Efficiency.....	94
11 Above-Threshold Modal Properties.....	101
11.1 Surface Emission Power versus Pump Power Relation.....	101
11.2 Nonuniform Pumping Effects.....	103
11.3 Considerations in Optimal Design.....	106
12 Conclusion and Outlook.....	109
A Derivation of Coupled Local Mode Equations.....	112
A.1 Vector Field.....	112
A.2 Scalar Field.....	119
B Calculation of the Green's Function.....	123
Bibliography	127

List of Figures

1.1. Exponential growth of the heat density on the computer chips. The power density on a silicon chip has already exceeded 100 W cm^{-2}	3
1.2. Edge-emission spectra, cross-sectional SEM picture, and a schematic drawing of the measurement setup for a Ge-on-Si laser	6
1.3. (a) Schematic of recess integration showing a microcleaved laser platelet placed in a recess in silica on silicon and coupled with a waveguide. (b) SEM image of a passive microcleaved ridge waveguide platelet positioned in a dielectric recess on Si substrate and aligned with a silicon oxy-nitride waveguide	6
1.4. Schematic of the heterogeneous microdisk laser structure, showing the disk cavity, SOI wire waveguide, bottom contact layer, tunnel junction, and metal contacts. (b) Cross section of the bonded structure, zooming in at the interface showing BCB as the bonding layer.....	8
1.5. (a) Schematic of a cross-sectional view of the hybrid evanescent laser structure with the optical mode superimposed. (b) Schematic of a side view of the hybrid evanescent laser structure. (c) Vertical index profile and optical mode profile. (d) Confinement factors for the quantum wells (QWs) and silicon waveguide	12
2.1. Refractive index profile for the uncoupled waveguides $n_a(x)$ and $n_b(x)$ and for the coupled-waveguide structure $n_c(x)$	14

2.2. Field profile of the two supermodes E_o and E_e in the three limiting cases: $\delta < 0$, $\delta = 0$, and $\delta > 0$	19
2.3. (a) Index profile of the III–V waveguide. (b) Fundamental mode of the III–V waveguide. (c) Index profile of the Si waveguide. (d) Fundamental mode of the Si waveguide.....	22
2.4. (a) Index profile of the coupled-waveguide system. (b), (d), (f) Even supermode and (c), (e), (g) odd supermode of the coupled-waveguide system as the Si waveguide width W is increased. The phase-matching condition is achieved in (d) and (e) where $\delta \rightarrow 0$ and the modal power in the III–V and Si waveguides is evenly distributed	23
2.5. (a) Confinement factors in the active region (Γ_{act}) and in the Si waveguide (Γ_{Si}) as a function of the Si waveguide width W . (b) Confinement factors in the III–V ($\Gamma_{\text{III-V}}$) and Si waveguide (Γ_{Si}), and the mismatch parameter δ as a function of the Si waveguide width W . (c) Calculated values of $ \delta $ and κ as a function of the Si waveguide width W	24
2.6. Two configurations of supermode Si/III–V lasers. (a) Asymmetric: one adiabatic taper, output comes only from the right Si end facet. (b) Symmetric: two adiabatic tapers, output comes from both left and right Si end facets	25
2.7. (a) Supermode Si/III–V optical amplifier. (b) Supermode Si/III–V photodetector.....	27
2.8. Conception of future large-scale, high-efficiency hybrid optoelectronic circuitry. Devices with different optical functions can be integrated on the Si platform. The	

light transportation from one module to another can be on-chip by Si waveguides or chip-to-chip by optical fibers.....	29
3.1. Model of the adiabatic mode transformer based on two coupled waveguides 1 and 2 , placed in close proximity to each other. The geometry of waveguide 2 is gradually varied along the z direction. The modal profiles of the local modes \mathbf{e}_e and \mathbf{e}_o are listed at the input, phase-matching, and output planes.....	34
3.2. Dispersion curves of the propagation constants along z	35
3.3. Coupling efficiency as a function of the transformer length $L (= z_f - z_i)$ for devices designed with γ distributions of $\tan[\arcsin(u)]$, u , u^3 , and $\sin(u)$ where u is proportional to $z - z_0$. The optimal design with γ distributed with $\tan[\arcsin(u)]$ has the least length for adiabatic mode transformation.....	40
3.4. Fraction of power in the wanted (even) and unwanted (odd) supermodes along the propagation direction in a 200- μm -long mode transformer with the optimal design. The equiripple behavior of both modes indicates that the total scattered power into the odd mode is minimized.....	41
4.1. Refractive index profile and optical mode profile of the InGaAsP epilayer	44
4.2. (a) The InGaAsP epilayer bonded to a Si slab waveguide. (b) Confinement factor for Si waveguide of the slab waveguide structure shown in (a). This is the maximal fraction of modal power in Si if the Si slab is replaced with a channel waveguide	46
4.3. (a) Illustration of the cross-sectional view of the hybrid laser (not to scale). (b) Si waveguide dimensions of the supermode lasers: $L_{\text{end}} = 350 \mu\text{m}$, $L_{\text{taper}} = 200 \mu\text{m}$,	

$L_{\text{ctr}} = 400 \text{ } \mu\text{m}$, $w_{\text{end}} = 1.2 \text{ } \mu\text{m}$, $w_{\text{ctr}} = 0.6, 0.7, 0.8, \text{ or } 0.9 \text{ } \mu\text{m}$. The tapers connecting the end and central sections have linear width variation	47
4.4. Quantum well confinement factor Γ_{QW} as a function of the Si waveguide width w . Inset: Calculated confinement factors of the III–V and the Si waveguide	47
4.5. Fabrication flow chart of supermode hybrid Si/III–V lasers.....	51
4.6. SEM cross-sectional images of the InGaAsP epifilm on SOI by wafer bonding after the InP substrate removal. (a) Zoom at one end of the epifilm. (b) Zoom at middle of the epifilm	53
4.7. Annealing system for fabricating continuous-wave semiconductor lasers.....	55
4.8. (a) Optical microscope image of top view of a fabricated device. (b), (c) SEM images of a cleaved end facet of a fabricated supermode Si/InGaAsP laser: (b) overview of the device, (c) close-up view at the center Si waveguide region. Approximate proton implanted regions are superimposed on the image for illustration	56
5.1. Experimental setup for measuring (a) laser L – I curve, and (b) near-field emission pattern and optical spectrum	58
5.2. Threshold current density J_{th} and slope efficiency η_{ex} as a function of the width of central section of the Si waveguide w_{ctr} . The threshold current density increases monotonically as w_{ctr} , but the slope efficiency presents a local maximum at $w_{\text{ctr}} = 0.8 \text{ } \mu\text{m}$	59

5.3. Bonding interfacial layer confinement factor Γ_{BL} as a function of the Si waveguide width w . The maximal confinement to the bonding interfacial layer is achieved at $w = 0.73 \mu\text{m}$	60
5.4. (a) Optical spectrum of a typical device. (b) Evolution of the optical spectrum as the pump current (voltage) increases. Higher pump level results in the expansion of the range of lasing modes to the longer wavelength side. Spectra in both (a) and (b) were measured with pulsed current injection.....	61
5.5. Near-field patterns of the edge emission from a device operated (a) below threshold, (b) at threshold, and (c) above threshold. The modal confinement to the Si waveguide (especially when the mode is lasing) is obvious	63
5.6. Threshold voltage of evanescent Si/InGaAsP lasers with constant Si waveguide widths. Measurements were taken in pulsed mode at 15°C , with d_c denoting the duty cycle of the applied voltage	63
5.7. (a) $L-I-V$ curve of a $960\text{-}\mu\text{m}$ -long evanescent laser under CW operation at 15°C . (b) Lasing threshold current (in log scale) as a function of temperature (blue “+” signs) with a linear fit (red dashed line).....	66
5.8. (a) Optical spectrum of a Si/InGaAsP evanescent laser (in dB scale). (b) Evolution of the optical spectrum as the pump current increases. The emission lines shift to longer wavelength side and the envelope broadens with higher pump levels. Spectra in both (a) and (b) were measured with CW current injection	67

7.1. Surface-emitting circular Bragg lasers: (a) circular DFB laser; (b) disk Bragg laser; (c) ring Bragg laser. Laser emission is coupled out of the resonator plane in the vertical direction via the Bragg gratings	73
8.1. Real part of the Green's function $G(z, z')$ with $-\infty < z < \infty$ and z' between the top and bottom surfaces of the laser resonator	79
8.2. Radiation coupling coefficient h_1 and feedback coupling coefficient h_2 as a function of the duty cycle d_c of the Hankel-phased rectangular grating	81
9.1. Two types of boundary conditions for calculating reflectivities. (a) $A(0) = B(0)$, $r_1(L) = A(L)/B(L)$; (b) $B(L) = 0$, $r_2(x_0, L) = B(x_0)/A(x_0)$	85
10.1. Far-field intensity patterns of the fundamental mode of (a) circular DFB, (b) disk, and (c) ring Bragg lasers	94
10.2. Evolution of threshold gains of the 5 lowest-order modes of (a) circular DFB, (b) disk, and (c) ring Bragg lasers	95
10.3. Unnormalized quality factor of circular DFB, disk, and ring Bragg lasers	97
10.4. Modal area of circular DFB, disk, and ring Bragg lasers. The top surface area of the laser resonator (πx_b^2) is also plotted as a reference	98
10.5. Internal emission efficiency of circular DFB, disk, and ring Bragg lasers	99
11.1. Surface emission power P_{em} (in units of P_{sat}) versus pump power level P_{pump} for the fundamental mode of circular DFB laser ($x_b = 200$) under uniform pumping. The laser threshold P_{th} is defined as the pump level at the onset of surface laser emission. The external emission efficiency η_{ex} is defined as the slope of the linear fit of the simulated data points up to $P_{\text{em}} = 10P_{\text{sat}}$	102

11.2. Illustration of different pump profiles: (a) uniform; (b) Gaussian; (c) annular	103
11.3. Device-size-dependent pump level P_{pump} and frequency detuning factor δ of the 3 lowest-order modes, under uniform pump profile, of (a) circular DFB, (b) disk, and (c) ring Bragg lasers	107

List of Tables

4.1. InGaAsP epiwafer layer structure	44
5.1. Test results of supermode (varying-width) lasers and evanescent (constant-width) lasers	59
8.1. Approximated layer structure for numerical study	79
10.1. Modal field patterns, along with their threshold gains (g_A) and frequency detuning factors (δ), of the circular DFB, disk, and ring Bragg lasers. All the three types of lasers have an exterior boundary radius of $x_b = 200$	91
11.1. Threshold pump level P_{th} (in units of P_0) and external emission efficiency η_{ex} (in units of P_{sat}/P_0) of circular DFB, disk, and ring Bragg lasers under different pump profiles	105

List of Publications

Invited Book Chapters

- (1) **Xiankai Sun** and Amnon Yariv, “Surface-emitting circular Bragg lasers – a promising next-generation on-chip light source for optical communications,” in *Frontiers in Guided Wave Optics and Optoelectronics*, Bishnu Pal (ed.), Intech, 2010. ISBN: 978-953-7619-82-4.
- (2) Michael Shearn, **Xiankai Sun**, M. David Henry, Amnon Yariv, and Axel Scherer, “Advanced plasma processing: etching, deposition, and wafer bonding techniques for semiconductor applications,” in *Semiconductor Technologies*, Jan Grym (ed.), Intech, 2010. ISBN: 978-953-307-080-3 (in press).
- (3) Jacob Scheuer and **Xiankai Sun**, “Radial Bragg resonators,” in *Photonic Microresonator Research and Applications*, Ioannis Chremmos, Otto Schwelb, and Nikolaos Uzunoglu (eds.), Springer, 2010. ISBN: 978-1-4419-1743-0 (in press).

Refereed Journal Papers

- (1) Michael Shearn, Kenneth Diest, **Xiankai Sun**, Avi Zadok, Harry Atwater, Amnon Yariv, and Axel Scherer, “Advanced silicon processing for active planar photonic devices,” *Journal of Vacuum Science & Technology B*, **27** (6): 3180–3182, Nov./Dec. 2009.
- (2) **Xiankai Sun** and Amnon Yariv, “Surface-emitting circular DFB, disk-, and ring-Bragg resonator lasers with chirped gratings. III: gain saturation effects and above-threshold analysis,” *Optics Express*, **17** (12): 10119–10125, Jun. 2009.
- (3) **Xiankai Sun**, Avi Zadok, Michael J. Shearn, Kenneth A. Diest, Alireza Ghaffari, Harry A. Atwater, Axel Scherer, and Amnon Yariv, “Electrically pumped hybrid evanescent Si/InGaAsP lasers,” *Optics Letters*, **34** (9): 1345–1347, May 2009.
- (4) **Xiankai Sun**, Hsi-Chun Liu, and Amnon Yariv, “Adiabaticity criterion and the shortest adiabatic mode transformer in a coupled-waveguide system,” *Optics Letters*, **34** (3): 280–282, Feb. 2009.

- (5) **Xiankai Sun** and Amnon Yariv, “Surface-emitting circular DFB, disk-, and ring-Bragg resonator lasers with chirped gratings. II: nonuniform pumping and far-field patterns,” *Optics Express*, **17** (1): 1–6, Jan. 2009.
- (6) **Xiankai Sun** and Amnon Yariv, “Surface-emitting circular DFB, disk-, and ring-Bragg resonator lasers with chirped gratings: a unified theory and comparative study,” *Optics Express*, **16** (12): 9155–9164, Jun. 2008. (Selected for *Virtual Journal of Ultrafast Science*, **7** (8), Aug. 2008)
- (7) **Xiankai Sun** and Amnon Yariv, “Engineering supermode silicon/III–V hybrid waveguides for laser oscillation,” *Journal of the Optical Society of America B*, **25** (6): 923–926, Jun. 2008.
- (8) Lin Zhu, **Xiankai Sun**, Guy A. DeRose, Axel Scherer, and Amnon Yariv, “Room temperature continuous wave operation of single-mode, edge-emitting photonic crystal Bragg lasers,” *Optics Express*, **16** (2): 502–506, Jan. 2008.
- (9) **Xiankai Sun** and Amnon Yariv, “Modal properties and modal control in vertically emitting annular Bragg lasers,” *Optics Express*, **15** (25): 17323–17333, Dec. 2007 (also in the Virtual Focus Issue on Physics and Applications of Microresonators).
- (10) Lin Zhu, **Xiankai Sun**, Guy A. DeRose, Axel Scherer, and Amnon Yariv, “Spatial modal control of two dimensional photonic crystal Bragg lasers,” *Optics Letters*, **32** (16): 2273–2275, Aug. 2007.
- (11) Amnon Yariv and **Xiankai Sun**, “Supermode Si/III-V hybrid lasers, optical amplifiers and modulators: a proposal and analysis,” *Optics Express*, **15** (15): 9147–9151, Jul. 2007.
- (12) Lin Zhu, **Xiankai Sun**, Guy A. DeRose, Axel Scherer, and Amnon Yariv, “Continuous-wave operation of electrically-pumped, single-mode, edge-emitting photonic crystal lasers,” *Applied Physics Letters*, **90** (26): 261116, Jun. 2007.
- (13) **Xiankai Sun**, Jacob Scheuer, and Amnon Yariv, “Optimal design and reduced threshold in vertically emitting circular Bragg disk resonator lasers,” *IEEE Journal of Selected Topics in Quantum Electronics*, **13** (2): 359–366, Mar./Apr. 2007 (Special Issue on Optical Micro- and Nanosystems).

Refereed Conference Papers

- (1) **Xiankai Sun**, Michael J. Shearn, Avi Zadok, Marina S. Leite, Scott T. Steger, Harry A. Atwater, Axel Scherer, and Amnon Yariv, “Electrically pumped supermode Si/InGaAsP hybrid lasers,” *CLEO/QELS 2010*, San Jose, CA, May 2010.

- (2) **Xiankai Sun** and Amnon Yariv, "Above-threshold analysis of large-area, high-power, vertically-emitting circular Bragg lasers," *Frontiers in Optics 2009*, San Jose, CA, Oct. 2009.
- (3) **Xiankai Sun** and Amnon Yariv, "A comparative study of modal properties of surface-emitting circular Bragg micro-lasers," *CLEO/Pacific Rim 2009*, Shanghai, China, Aug. 2009.
- (4) **Xiankai Sun** and Amnon Yariv, "Supermode control in integrated hybrid Si/III-V optoelectronic circuits for modal gain enhancement," *CLEO/Pacific Rim 2009*, Shanghai, China, Aug. 2009.
- (5) **Xiankai Sun**, Hsi-Chun Liu, and Amnon Yariv, "How short can an adiabatic mode transformer be in a coupled waveguide system?" *CLEO/IQEC 2009*, Baltimore, MD, May 2009.
- (6) Michael Shearn, Kenneth Diest, **Xiankai Sun**, Avi Zadok, Amnon Yariv, Axel Scherer, "Advanced silicon processing for active integrated photonic devices," *EIPBN 2009*, Marco Island, FL, May 2009.
- (7) **Xiankai Sun**, Avi Zadok, Michael J. Shearn, Kenneth A. Diest, Alireza Ghaffari, Harry A. Atwater, Axel Scherer, and Amnon Yariv, "Hybrid electrically pumped evanescent Si/InGaAsP lasers," *OFC/NFOEC 2009*, San Diego, CA, Mar. 2009.
- (8) **Xiankai Sun** and Amnon Yariv, "A unified theory for surface emitting chirped circular grating lasers," *SPIE Photonics West 2009*, San Jose, CA, Jan. 2009.
- (9) **Xiankai Sun** and Amnon Yariv, "Engineering surface-emitting annular Bragg lasers for single-mode, high-efficiency, high-power applications," *LEOS Annual Meeting 2008*, Newport Beach, CA, Nov. 2008.
- (10) **Xiankai Sun** and Amnon Yariv, "Designing large-area, high-efficiency, single-defect-mode vertically-emitting annular Bragg lasers," *Frontiers in Optics 2008*, Rochester, NY, Oct. 2008.
- (11) Lin Zhu, **Xiankai Sun**, Guy DeRose, Axel Scherer, and Amnon Yariv, "Room temperature continuous wave operation of single-mode, edge-emitting photonic crystal Bragg lasers," *CLEO/QELS 2008*, San Jose, CA, May 2008.
- (12) **Xiankai Sun**, Jacob Scheuer, and Amnon Yariv, "Optimal design of vertically emitting circular Bragg disk resonator lasers," *SPIE Photonics West 2008*, San Jose, CA, Jan. 2008.

Patents

- (1) Amnon Yariv and Xiankai Sun, “Hybrid Waveguide Systems and Related Methods,” US/PCT 12/110,310, pending, filed 2008.

Glossary of Acronyms

AlGaInAs: aluminum gallium indium arsenide

BC: boundary condition

BCB: benzocyclobutene

CMOS: complementary metal–oxide–semiconductor

CW: continuous wave

DBR: distributed Bragg reflector

DFB: distributed feedback

e-beam: electron beam

GaAs: gallium arsenide

GaP: gallium phosphide

InGaAsP: indium gallium arsenide phosphide

InP: indium phosphide

IR: infrared

MQW: multiple quantum well

QW: quantum well

RC: resistive–capacitive

SEM: scanning electron microscope

SOI: silicon on insulator

VCSEL: vertical cavity surface emitting laser

WDM: wavelength division multiplexing

Part I

Supermode Si/III-V Hybrid Lasers: Theory, Design, Fabrication, and Characterization

Chapter 1

Introduction

1.1 Motivation of a Laser on Silicon

The voracious appetite for a higher rate of data processing and transmission of computers and networks has resulted in an ever-increasing density of the silicon (Si) large-scale integration. However, this technology is approaching a bottleneck because of the inherent problems associated with the copper interconnections.

The electronic integration with higher device density consumes more power and at the same time generates more heat in a unit area on the chip. It is difficult to find an effective way to dissipate the generated heat. Figure 1.1 is a graph from Professor Bahram Jalali's paper in *Nature Photonics* [1]. It demonstrates clearly the exponential growth of the heat density on the computer chips. The heat dissipation density is exceeding that of a hot plate, and in fact it is not far away from that of a nuclear reactor. The heat dissipation issue itself sets a limitation on the future growth of the integration density.

Because of the concern of heat dissipation, the processor manufacturers gradually abandoned the higher transistor count strategy, turning to multiple core processing. Even though each processor is very powerful, their cooperation runs into a communication barrier: moving data between different cores takes too long due to the resistive-capacitive

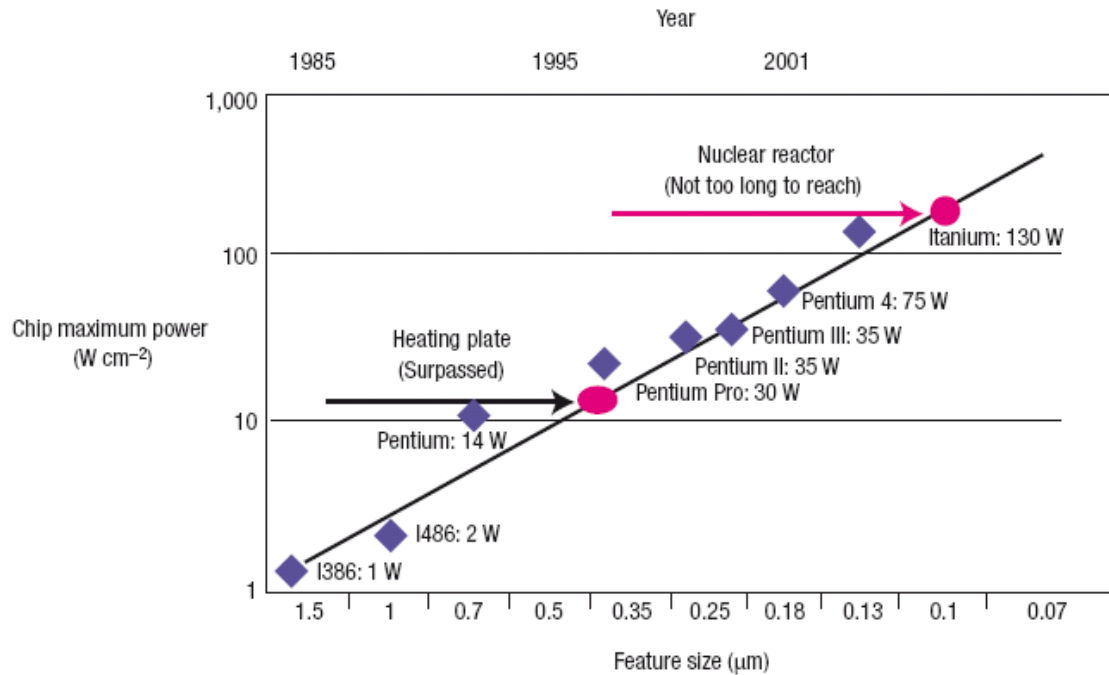


Fig. 1.1. Exponential growth of the heat density on the computer chips. The power density on a silicon chip has already exceeded 100 W cm^{-2} . Reprinted with permission from [1], © 2007 Macmillan Publishers Ltd.

(RC) delay. When the data rates approach 10 Gb s^{-1} and beyond, optical communication becomes a superior and perhaps even the only solution on the horizon simply because of its considerably larger operational bandwidth. This is the underlying driving force of the research of Si photonics.

In a photonic circuit, one should have various functional devices for light generation, guiding, modulation, amplification, filtering, and detection. Indeed, an on-chip integrable laser is an indispensable element in active photonic circuits. Unfortunately, Si is a poor converter of electricity to light, due to its indirect semiconductor bandgap. In addition, the epitaxial growth of standard GaAs- and InP-based direct bandgap materials on Si substrates has proven to be a major obstacle, due to the mismatch in lattice constants and in thermal

expansion coefficients [2]. Despite these difficulties, recent years witnessed a reawakening of the interest in Si-integrated lasers, with various approaches toward its practical realization.

1.2 Review of Various Integration Schemes

Numerous avenues have been followed toward obtaining Si-integrated lasers, including Raman amplification [3], rare-earth doping [4], and nanocrystalline Si structures [5]. Since III–V semiconductor compounds have been well known as efficient light emitting materials, integration of these materials on Si platform is considered as the most promising approach, although band-engineered epitaxial germanium (Ge) has recently been shown to be a potential laser material. In the following we will review several schemes that are being implemented to integrate the active materials on Si.

Direct Growth of Active Materials on Si

Due to the large lattice mismatch between Si and GaAs (4.1%) or InP (8.1%), heteroepitaxial growth of III–V on Si has been very difficult for producing material with high quality because the density of threading dislocations in the epitaxial layers is too high, which greatly reduces the lifetime of fabricated devices [6]. A possible way to overcome this difficulty is to use buffer layers to fully relax the stress during the growth so as to prevent the dislocations from extending into the useful active layers. Since the difference between the lattice constants of GaP and Si is only 0.3%, using GaP as the buffer layer for the epigrowth of GaP-based compound materials on Si is a good choice. Electrically

injected lasers grown by metal organic vapor phase epitaxy have been demonstrated for GaP-based broad-area Ga(NAsP)/GaP single-quantum-well heterostructures near room temperature [7]. The work on growing the dilute nitride Ga(NAsP) on Si substrate using GaP as the buffer layer to achieve lasing for practical uses is still underway [8].

In the meantime, the study of using Ge as the active material on Si substrate has made good progress [9-11]. Due to its pseudodirect gap properties and compatibility with Si complementary metal–oxide–semiconductor (CMOS) technology, Ge may also be used in the electronic–photonic integration. It has been shown that Ge can be band engineered by tensile strain and n -type doping to achieve efficient light emission and optical gain from its direct gap transition. Indeed, the optical gain in the wavelength range of 1600–1608 nm from n^+ tensile-strained epitaxial Ge on Si (100) substrate has been observed [9]. Optical pumped lasing action at room temperature edge-emitted from such Ge waveguides has recently been achieved [11]. The laser threshold is still very high, and further investigation on p -type doping in Ge is necessary to achieve an electrically pumped device. Figure 1.2 shows the emission spectra, cross-sectional scanning electron microscope (SEM) image of the Ge waveguide and a schematic drawing of the experimental setup for optical pumping.

Recess Integration of Lasers with Waveguides on Si

In the recess integration scheme, III–V ridge waveguide gain elements such as diode lasers and semiconductor optical amplifiers are coaxially aligned with, and coupled to, silicon oxy-nitride (SiO_xN_y) waveguides on silicon substrates [12]. This method is

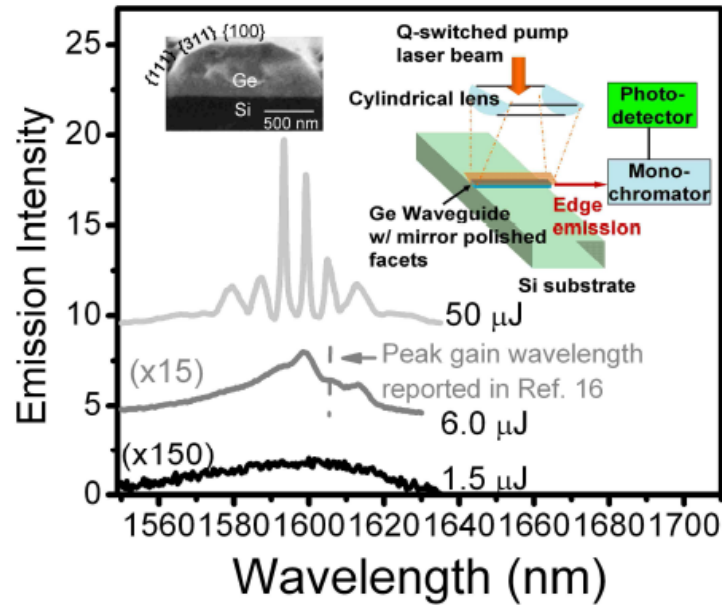


Fig. 1.2. Edge-emission spectra of a Ge waveguide with mirror polished facets under 1064 nm excitation from a *Q*-switched laser with a pulse duration of 1.5 ns and a repetition rate of 1 kHz. The three spectra at 1.5, 6.0, and 50 μJ /pulse pumping power correspond to spontaneous emission, threshold for lasing, and laser emission. The inset shows a cross-sectional SEM picture of the Ge waveguide and a schematic drawing of the experimental setup for optical pumping. Reprinted with permission from [11], © 2010 OSA.

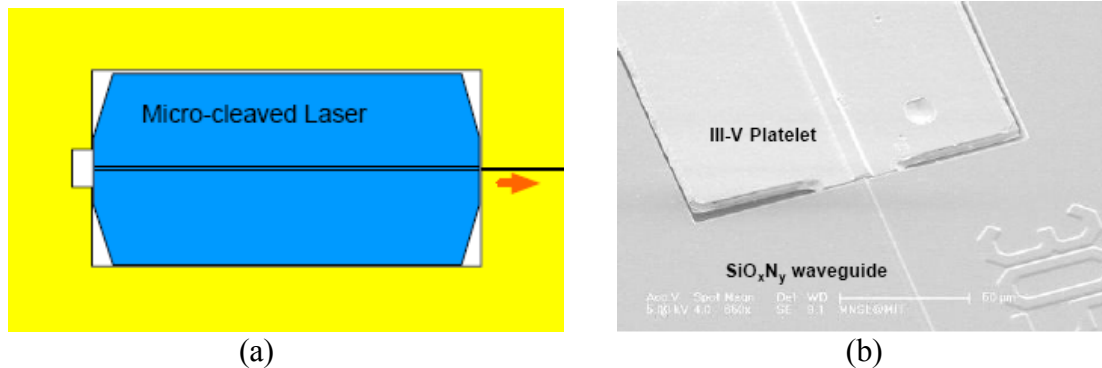


Fig. 1.3. (a) Schematic of recess integration: a microcleaved laser platelet is placed in a recess in silica on silicon. The laser emission is coupled into the silicon oxy-nitride waveguide for light transportation. (b) Scanning electron microscope (SEM) image of a passive microcleaved ridge waveguide platelet positioned in a dielectric recess on Si substrate and aligned with a SiO_xN_y waveguide. The image is a close-up view of one end of a platelet in a recess showing a well-aligned pair of waveguides. Reprinted with permission from [12], © 2008 SPIE.

claimed to be highly modular and consistent with standard Si-CMOS front- and back-end processing.

The process starts with fabricating silicon oxy-nitride waveguides in silicon oxide and then etching recesses for the laser platelets. The ridge waveguide lasers, prefabricated from typical III–V materials, were cleaved by a novel microcleaving technique to produce 6 μm thick, 100 μm wide, 300 μm long platelets with good end facets. These laser platelets were manually picked and bonded into the recesses, after which the top contact was fabricated. The light emitted from the laser is coaxially coupled to the silicon oxy-nitride waveguide for chip transport. As expected, the biggest obstacle of this scheme is the high coupling loss arising from the misalignment between the laser and the waveguide.

Figure 1.3(a) is a schematic drawing of the recess integration. Figure 1.3(b) is a SEM image of a microcleaved III–V ridge waveguide platelet positioned in a dielectric recess on Si substrate and aligned with a silicon oxy-nitride waveguide.

Integrating III–V Materials with Si by Wafer Bonding

To overcome the problems encountered in the epitaxial growth or thin-film deposition, wafer bonding is introduced in photonic integration, which provides a way to join together two disparate materials without the restriction of matching lattice constants. Based on the different applications, two types of wafer bonding are usually used to integrate the III–V materials on Si platform: (1) adhesive bonding (also known as “polymer bonding”) and (2) direct bonding (also known as “fusion bonding” or “molecular bonding”). The

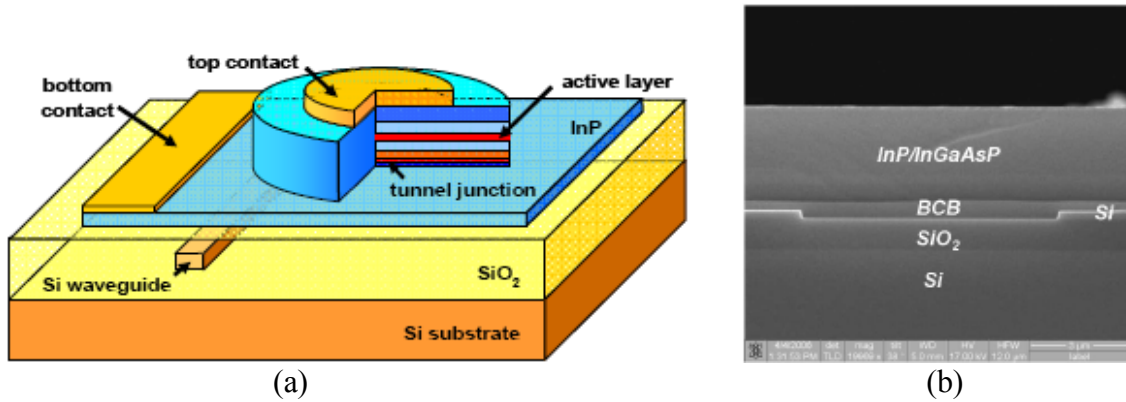


Fig. 1.4. Schematic of the heterogeneous microdisk laser structure, showing the disk cavity, SOI wire waveguide, bottom contact layer, tunnel junction, and metal contacts. (b) Cross section of the bonded structure, zooming in at the interface showing benzocyclobutene (BCB) as the bonding layer. Reprinted with permission from [13, 14], © 2006, 2007 OSA.

successful examples of using these two types of wafer bonding techniques are shown below.

In [13, 14], an InP/InGaAsP thin film epitaxial layer was bonded to a silicon-on-insulator (SOI) waveguide circuit by adhesive bonding using divinyl-tetramethyldisiloxane-benzocyclobutene (DVS-BCB). Lasers and photodetectors were fabricated in the bonded InP/InGaAsP epitaxial layer. Light emitted from the laser is vertically coupled into the Si waveguide with an inverted taper approach. Figure 1.4(a) shows an electrically injected InGaAsP microdisk laser coupled with an underlying submicron Si wire waveguide. The microdisk laser has a diameter of $7.5\ \mu\text{m}$ and a thickness of $1\ \mu\text{m}$. The laser with emission wavelength at $1.6\ \mu\text{m}$ has a low threshold current of $0.5\ \text{mA}$ under continuous-wave operation at room temperature, and a SOI-coupled maximum unidirectional output power of $10\ \mu\text{W}$. Figure 1.4(b) is a SEM image

showing the cross section of the wafer-bonded structure with DVS-BCB as the bonding interlayer.

In applications that require direct contact of the two materials, i.e., with no intermediate bonding layers, the above adhesive bonding is inapplicable when direct coupling is required through bonding. The direct wafer bonding is a process in which the adhesion between two semiconductor surfaces occurs as a result of chemical bonds established between the atoms and molecules from the two surfaces. The adhesion is weak at room temperature (because of the Van der Waals forces) and this can be greatly enhanced with a high-temperature thermal annealing to transform the weak bonds into stronger covalent bonds. However, this high-temperature annealing step induces material degradation and is incompatible with back-end Si CMOS processing. For this purpose, many efforts have been put into reducing the annealing temperature while keeping a strong bonding [15-17]. A special surface preparation process (surface activation) is usually performed to change and control the bonding mechanism by controlling the surface chemistry. Surface activation can be performed by a dip of the substrates in chemical solutions (wet activation) [18] or by a plasma treatment of the surface (dry activation) [19].

For Si-to-InP wafer bonding, a prebonding oxygen (O_2) plasma surface treatment has been demonstrated to yield a very spontaneous bonding at room temperature [19]. This plasma aims to have a high density of chemically active species arrive at the surface with a low incident power to minimize surface damages. The postbonding annealing temperature can be below 200 °C while the interface strength can be as high as the bulk fracture energy of InP. The plasma affects the bonding surfaces both physically and chemically. The O_2 plasma is used to remove hydrocarbon and water molecules so as to reduce the probability

of the formation of interfacial bubbles and voids during postbonding annealing. Additionally, the plasma treatment generates a very smooth and reactive thin oxide layer that helps in bonding process. As a powerful tool of heterogeneous photonic integration, this low-temperature O_2 plasma-assisted wafer bonding technique has given birth to a series of hybrid Si/III–V photonic devices, among which the Si evanescent laser will be introduced in the next section as a representative.

1.3 Introduction of Si/III–V Evanescent Lasers

Using the direct wafer bonding technique, an active AlGaInAs material is transferred onto a prepatterned Si-on-insulator wafer. The top AlGaInAs layers, which include multiple quantum wells (MQWs), are then patterned postbonding to produce Fabry–Pérot [20], racetrack [21] and distributed-feedback (DFB) lasers [22]. The bonded structure is designed to support a joint optical mode, whose profile overlaps both materials. During operation, this optical mode is guided in a Si waveguide and is amplified by its *evanescent* penetration into a III–V slab waveguide, which provides optical gain when electric current is injected [see Fig. 1.5(a) and (b)], and thus these devices are referred to as Si/AlGaInAs evanescent lasers [20].

The reliance on the small evanescent tail penetrating into the III–V slab waveguide to obtain optical gain is a major drawback: the trade-off between the modal confinement factors in the Si and in the III–V prevents efficient use of the gain from the III–V material, which makes the lasers operate with substantially lower efficiency than the traditional semiconductor lasers [see Fig. 1.5(c) and (d)]. Because of the inefficient use of gain, the

lasers had to be fabricated very long, whose large footprint reduces the density of photonic integration on a chip. This is the major hurdle to be overcome before this hybrid Si/III–V technology can be industrialized.

In the following chapters we will apply a novel mode control method to such hybrid waveguide system to enhance the modal gain, which makes for more efficient and, most importantly, shorter devices that may hold the key to the photonics/electronics integration. The supermode theory will be presented, based on which the modal control method will be described. The shortest adiabatic mode transformer (also known as “taper,” “mode converter,” or “mode adapter”) will be studied. The device design procedure and fabrication process will be elaborated, followed by the experimental demonstration of the performance enhancement in the mode-controlled Si/InGaAsP laser devices. This modal control method can also be extended to design other hybrid Si/III–V photonic devices and circuits whose performances are expected to be significantly improved by the gain enhancement.

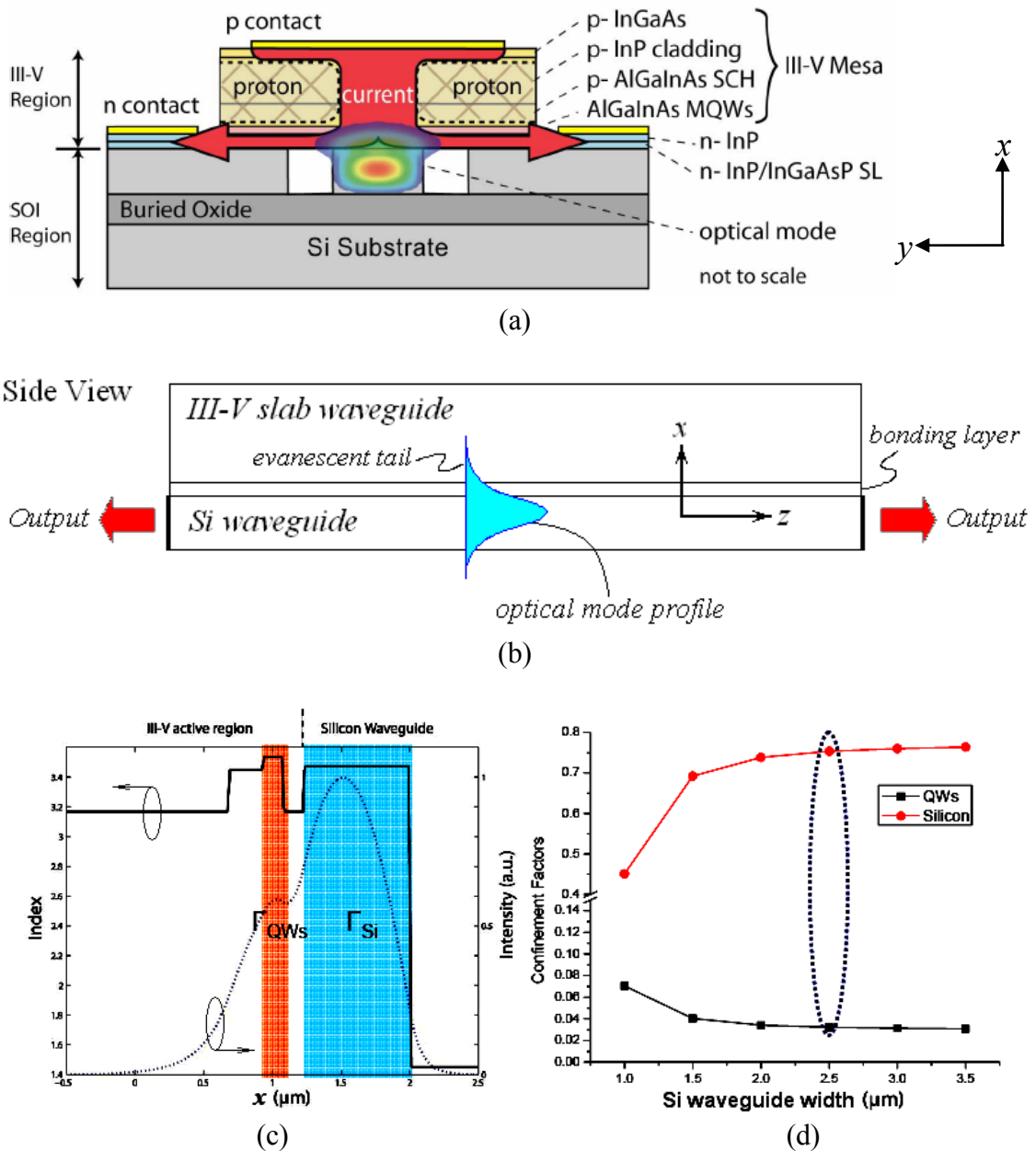


Fig. 1.5. (a) Schematic of a cross-sectional view of the hybrid evanescent laser structure with the optical mode superimposed. (b) Schematic of a side view of the hybrid evanescent laser structure. The optical mode is amplified by the penetration of the small *evanescent* tail into the III-V slab waveguide to obtain the optical gain. (c) Vertical index profile and optical mode profile. (d) Confinement factors for the quantum wells (QWs) and silicon waveguide. (a), (c), and (d) courtesy of Professor John E. Bowers, University of California, Santa Barbara.

Chapter 2

Supermode Theory

The term “supermode” was initially introduced by Kapon et al. to analyze the modes propagating in semiconductor laser arrays [23]. The formalism was used formally in the textbook *Optical Electronics in Modern Communications* [24]. Here the “supermodes” refer to the eigenmodes of a system of two (or even more) coupled optical waveguides. In this chapter we will first derive the supermodes of a coupled optical waveguide system, then show the numerical simulation results based on a hybrid waveguide structure to support the theory.

This chapter is reproduced and adapted with permission from [25-27], © 2007, 2008 OSA, © 2009 IEEE.

2.1 Derivation of Supermodes of Coupled Optical Waveguides

We start with the Maxwell’s equations,

$$\begin{cases} \nabla \times \vec{H} = \frac{\partial}{\partial t}(\epsilon_0 \vec{E} + \vec{P}), \\ \nabla \times \vec{E} = -\frac{\partial}{\partial t}(\mu_0 \vec{H} + \vec{M}) = -\frac{\partial}{\partial t}(\mu \vec{H}). \end{cases} \quad (2.1)$$

Taking the curl of the second equation of (2.1) and using the first equation leads to

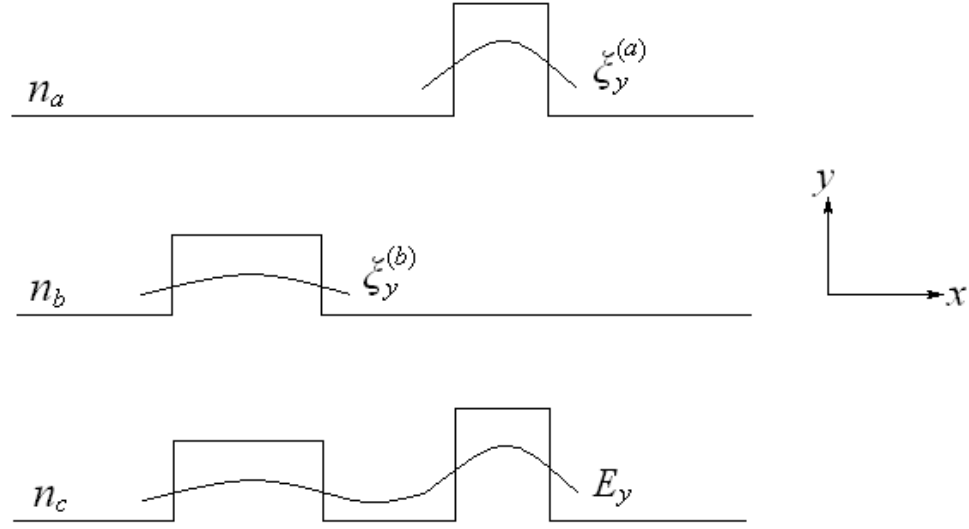


Fig. 2.1. Refractive index profile for the uncoupled waveguides $n_a(x)$ and $n_b(x)$ and for the coupled-waveguide structure $n_c(x)$.

$$\begin{aligned}
 \nabla \times (\nabla \times \vec{E}) &= -\frac{\partial}{\partial t} (\mu \nabla \times \vec{H}) = -\mu \frac{\partial^2}{\partial t^2} (\varepsilon_0 \vec{E} + \vec{P}) \\
 &= -\mu \frac{\partial^2}{\partial t^2} (\varepsilon_0 \vec{E} + \vec{P}_0 + \vec{P}_{pert}) = -\mu \frac{\partial^2}{\partial t^2} (\varepsilon \vec{E} + \vec{P}_{pert}).
 \end{aligned} \tag{2.2}$$

Using vector identity and $\nabla \cdot \vec{E} = 0$,

$$\nabla \times (\nabla \times \vec{E}) = \nabla (\nabla \cdot \vec{E}) - \nabla^2 \vec{E} = -\nabla^2 \vec{E}, \tag{2.3}$$

we have

$$\nabla^2 \vec{E} - \mu \varepsilon \frac{\partial^2 \vec{E}}{\partial t^2} = \mu \frac{\partial^2 \vec{P}_{pert}}{\partial t^2}. \tag{2.4}$$

Without loss of generality, we consider the case of two uncoupled 1-D (slab) waveguides with refractive index distributions $n_a(x)$ and $n_b(x)$ (see Fig. 2.1). The normalized transverse eigenmodes of each waveguide are $\xi_y^{(a)}(x)$ and $\xi_y^{(b)}(x)$, and their

propagation constants are β_a and β_b . The modal field of the coupled guide structure with an index distribution $n_c(x)$ can be expressed as a superposition of the uncoupled fields,

$$E_y(x, z) = A(z)\xi_y^{(a)}(x)e^{i(\omega t - \beta_a z)} + B(z)\xi_y^{(b)}(x)e^{i(\omega t - \beta_b z)}, \quad (2.5)$$

where $\xi_y^{(a)}(x)$ and $\xi_y^{(b)}(x)$ satisfy

$$\begin{aligned} \left(\frac{\partial^2}{\partial x^2} - \beta_a^2 \right) \xi_y^{(a)}(x) + \omega^2 \mu \varepsilon_0 n_a^2(x) \xi_y^{(a)}(x) &= 0, \\ \left(\frac{\partial^2}{\partial x^2} - \beta_b^2 \right) \xi_y^{(b)}(x) + \omega^2 \mu \varepsilon_0 n_b^2(x) \xi_y^{(b)}(x) &= 0. \end{aligned} \quad (2.6)$$

Substitution of (2.5) into (2.4) yields

$$e^{i\omega t} \left[-2i \left(\beta_a \frac{\partial A}{\partial z} \xi_y^{(a)} e^{-i\beta_a z} + \beta_b \frac{\partial B}{\partial z} \xi_y^{(b)} e^{-i\beta_b z} \right) \right] = \mu \frac{\partial^2 \bar{P}_{pert}}{\partial t^2}, \quad (2.7)$$

where we have used (2.6) and the “slow-varying” approximations $\left| \frac{\partial^2 A}{\partial z^2} \right| \ll \beta_a \left| \frac{\partial A}{\partial z} \right|$ and

$\left| \frac{\partial^2 B}{\partial z^2} \right| \ll \beta_b \left| \frac{\partial B}{\partial z} \right|$. The perturbation polarization is

$$\begin{aligned} P_{pert}(\vec{r}, t) &= P(\vec{r}, t) - P_0(\vec{r}, t) = \varepsilon_0 \varepsilon_r^{coup} E(\vec{r}, t) - \varepsilon_0 \varepsilon_r^{orig} E(\vec{r}, t) \\ &= \varepsilon_0 n_c^2(x) \left[A(z) \xi_y^{(a)}(x) e^{i(\omega t - \beta_a z)} + B(z) \xi_y^{(b)}(x) e^{i(\omega t - \beta_b z)} \right] \\ &\quad - \varepsilon_0 n_a^2(x) A(z) \xi_y^{(a)}(x) e^{i(\omega t - \beta_a z)} - \varepsilon_0 n_b^2(x) B(z) \xi_y^{(b)}(x) e^{i(\omega t - \beta_b z)} \\ &= e^{i\omega t} \varepsilon_0 \left[A(z) \xi_y^{(a)}(x) (n_c^2(x) - n_a^2(x)) e^{-i\beta_a z} + B(z) \xi_y^{(b)}(x) (n_c^2(x) - n_b^2(x)) e^{-i\beta_b z} \right]. \end{aligned} \quad (2.8)$$

Plugging (2.8) into (2.7), multiplying both sides by $\xi_y^{(a)}(x)$, then integrating over all x

leads to

$$\begin{aligned}
-4i\omega \frac{dA}{dz} e^{-i\beta_a z} = \varepsilon_0 \frac{\partial^2}{\partial t^2} \left[\int_{-\infty}^{\infty} \left(\xi_y^{(a)}(x) \right)^2 \left(n_c^2(x) - n_a^2(x) \right) dx A(z) e^{-i\beta_a z} \right. \\
\left. + \int_{-\infty}^{\infty} \xi_y^{(a)}(x) \xi_y^{(b)}(x) \left(n_c^2(x) - n_b^2(x) \right) dx B(z) e^{-i\beta_b z} \right], \quad (2.9)
\end{aligned}$$

where we have used the mode orthogonality condition,

$$\int_{-\infty}^{\infty} \xi_y^{(a)}(x) \xi_y^{(b)}(x) dx = \frac{2\omega\mu}{\beta_a} \delta_{a,b}. \quad (2.10)$$

Likewise,

$$\begin{aligned}
-4i\omega \frac{dB}{dz} e^{-i\beta_b z} = \varepsilon_0 \frac{\partial^2}{\partial t^2} \left[\int_{-\infty}^{\infty} \xi_y^{(a)}(x) \xi_y^{(b)}(x) \left(n_c^2(x) - n_a^2(x) \right) dx A(z) e^{-i\beta_a z} \right. \\
\left. + \int_{-\infty}^{\infty} \left(\xi_y^{(b)}(x) \right)^2 \left(n_c^2(x) - n_b^2(x) \right) dx B(z) e^{-i\beta_b z} \right]. \quad (2.11)
\end{aligned}$$

If we introduce the definitions,

$$\begin{aligned}
\kappa_{ab,ba} &= \frac{\omega\varepsilon_0}{4} \int_{-\infty}^{\infty} \left[n_c^2(x) - n_{b,a}^2(x) \right] \xi^{(a)}(x) \xi^{(b)}(x) dx, \\
M_{a,b} &= \frac{\omega\varepsilon_0}{4} \int_{-\infty}^{\infty} \left[n_c^2(x) - n_{a,b}^2(x) \right] \left(\xi^{(a,b)}(x) \right)^2 dx, \quad (2.12)
\end{aligned}$$

then we have

$$\begin{cases} \frac{dA}{dz} = -i\kappa_{ab} B e^{-i(\beta_b - \beta_a)z} - iM_a A, \\ \frac{dB}{dz} = -i\kappa_{ba} A e^{-i(\beta_a - \beta_b)z} - iM_b B. \end{cases} \quad (2.13)$$

To simplify (2.13), we introduce $A = \tilde{A} e^{-iM_a z}$ and $B = \tilde{B} e^{-iM_b z}$ and define $\beta'_{a,b} = \beta_{a,b} + M_{a,b}$,

then we get

$$E_y(x, z) = e^{i\omega t} \left(\tilde{A} e^{-i\beta'_a z} \xi_y^{(a)} + \tilde{B} e^{-i\beta'_b z} \xi_y^{(b)} \right), \quad (2.14)$$

and

$$\begin{cases} \frac{d\tilde{A}}{dz} = -i\kappa_{ab}\tilde{B}e^{-i(\beta'_b-\beta'_a)z}, \\ \frac{d\tilde{B}}{dz} = -i\kappa_{ba}\tilde{A}e^{i(\beta'_b-\beta'_a)z}. \end{cases} \quad (2.15)$$

Eq. (2.14) can be expressed in the basis of $\{\xi_y^{(a)}, \xi_y^{(b)}\}$ as a column vector,

$$\underline{E} = \begin{pmatrix} E^{(1)} \\ E^{(2)} \end{pmatrix} = \begin{pmatrix} \tilde{B}e^{-i\beta'_bz} \\ \tilde{A}e^{-i\beta'_az} \end{pmatrix}, \quad (2.16)$$

so that

$$\frac{d\underline{E}}{dz} = \begin{pmatrix} -i\beta'_b & -i\kappa_{ba} \\ -i\kappa_{ab} & -i\beta'_a \end{pmatrix} \begin{pmatrix} E^{(1)} \\ E^{(2)} \end{pmatrix} = \underline{C}\underline{E}. \quad (2.17)$$

A propagating supermode, *by its definition*, is a field solution whose z (the propagation direction) dependence is only through a propagation phase factor $e^{i\gamma z}$, i.e.,

$\underline{E}(z) = \underline{E}(0)e^{i\gamma z}$, so

$$\frac{d\underline{E}}{dz} = i\gamma\underline{E}. \quad (2.18)$$

Combining (2.17) and (2.18) yields

$$(\underline{C} - i\gamma\underline{I})\underline{E} = 0, \quad (2.19)$$

i.e.,

$$\begin{vmatrix} -i\beta'_b - i\gamma & -i\kappa_{ba} \\ -i\kappa_{ab} & -i\beta'_a - i\gamma \end{vmatrix} \begin{pmatrix} E^{(1)} \\ E^{(2)} \end{pmatrix} = 0. \quad (2.20)$$

To have nontrivial solutions, we require that

$$\begin{vmatrix} -i\beta'_b - i\gamma & -i\kappa_{ba} \\ -i\kappa_{ab} & -i\beta'_a - i\gamma \end{vmatrix} = -\beta'_b\beta'_a - \gamma^2 - \gamma(\beta'_a + \beta'_b) + |\kappa|^2 = 0, \quad (2.21)$$

where $|\kappa| \equiv (\kappa_{ab}\kappa_{ba})^{\frac{1}{2}}$, leading to

$$\gamma = -\frac{\beta'_a + \beta'_b}{2} \pm \frac{1}{2} \sqrt{(\beta'_b - \beta'_a)^2 + 4|\kappa|^2}. \quad (2.22)$$

Let $\bar{\beta} = \frac{\beta'_a + \beta'_b}{2}$, $\delta = \frac{\beta'_b - \beta'_a}{2}$, and $S = \sqrt{\delta^2 + |\kappa|^2}$, then $\gamma_{1,2} = -\bar{\beta} \pm S$, and the

corresponding eigenfields (supermodes) are

$$\begin{aligned} \underline{E}_1 &= \begin{vmatrix} E_1^{(1)} \\ E_1^{(2)} \end{vmatrix} = \begin{vmatrix} i\kappa_{ba} \\ -i\beta'_b - i\gamma_1 \end{vmatrix} e^{i\gamma_1 z} = \begin{vmatrix} -\frac{\kappa_{ba}}{\delta + S} \\ 1 \end{vmatrix} e^{-i(\bar{\beta} - S)z}, \\ \underline{E}_2 &= \begin{vmatrix} E_2^{(1)} \\ E_2^{(2)} \end{vmatrix} = \begin{vmatrix} i\kappa_{ba} \\ -i\beta'_b - i\gamma_2 \end{vmatrix} e^{i\gamma_2 z} = \begin{vmatrix} -\frac{\kappa_{ba}}{\delta - S} \\ 1 \end{vmatrix} e^{-i(\bar{\beta} + S)z}. \end{aligned} \quad (2.23)$$

There are three limiting cases of our special interest:

(1) $\delta < 0, |\delta| \gg |\kappa|$,

so $S = |\delta| \left(1 + \frac{|\kappa|^2}{|\delta|^2} \right)^{\frac{1}{2}} \approx |\delta| \left(1 + \frac{1}{2} \frac{|\kappa|^2}{|\delta|^2} \right) = -\delta - \frac{|\kappa|^2}{2\delta}$, and

$$\begin{aligned} \underline{E}_1 &= \begin{vmatrix} 2\delta \\ \kappa_{ab} \\ 1 \end{vmatrix} e^{-i\beta'_b z} = \begin{vmatrix} 1 \\ \varepsilon_1 \\ 1 \end{vmatrix} e^{-i\beta'_b z}, \\ \underline{E}_2 &= \begin{vmatrix} -\frac{\kappa_{ba}}{2\delta} \\ 1 \end{vmatrix} e^{-i\beta'_a z} = \begin{vmatrix} \varepsilon_2 \\ 1 \end{vmatrix} e^{-i\beta'_a z}. \end{aligned} \quad (2.24)$$

where $\varepsilon_1 \equiv \frac{\kappa_{ab}}{2|\delta|}$, $\varepsilon_2 \equiv \frac{\kappa_{ba}}{2|\delta|}$ and $0 < \varepsilon_1, \varepsilon_2 \ll 1$.

(2) $\delta = 0$,

so $S = |\kappa|$, and

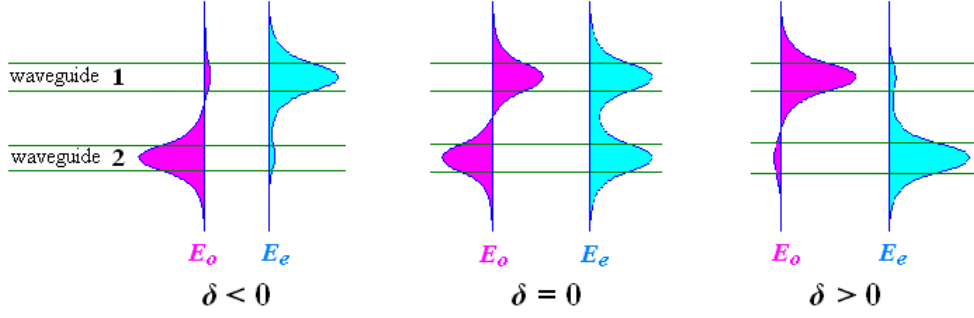


Fig. 2.2. Field profile of the two supermodes E_o and E_e in the three limiting cases: $\delta < 0$, $\delta = 0$, and $\delta > 0$.

$$\begin{aligned} \underline{E}_1 &= \begin{vmatrix} -\frac{\kappa_{ba}}{|\kappa|} \\ 1 \end{vmatrix} e^{-i(\bar{\beta}-|\kappa|)z} = \begin{vmatrix} -\eta \\ 1 \end{vmatrix} e^{-i\beta_o z}, \\ \underline{E}_2 &= \begin{vmatrix} \frac{\kappa_{ba}}{|\kappa|} \\ 1 \end{vmatrix} e^{-i(\bar{\beta}+|\kappa|)z} = \begin{vmatrix} \eta \\ 1 \end{vmatrix} e^{-i\beta_e z}. \end{aligned} \quad (2.25)$$

where $\eta \equiv \left(\frac{\kappa_{ba}}{\kappa_{ab}} \right)^{\frac{1}{2}} \approx 1$.

(3) $\delta > 0, \delta \gg |\kappa|$,

so $S = \delta \left(1 + \frac{|\kappa|^2}{\delta^2} \right)^{\frac{1}{2}} \approx \delta + \frac{|\kappa|^2}{2\delta}$, and

$$\begin{aligned} \underline{E}_1 &= \begin{vmatrix} -\frac{\kappa_{ba}}{2\delta} \\ 1 \end{vmatrix} e^{-i\beta'_a z} = \begin{vmatrix} -\epsilon_2 \\ 1 \end{vmatrix} e^{-i\beta'_a z}, \\ \underline{E}_2 &= \begin{vmatrix} \frac{2\delta}{\kappa_{ab}} \\ 1 \end{vmatrix} e^{-i\beta'_b z} = \begin{vmatrix} \frac{1}{\epsilon_1} \\ 1 \end{vmatrix} e^{-i\beta'_b z}. \end{aligned} \quad (2.26)$$

The field profiles of the supermodes in the three cases are illustrated in Fig. 2.2, where the subscripts “o” (odd) and “e” (even) refer to the modal symmetry.

2.2 Numerical Verification of the Supermode Theory

To numerically verify the supermode theory, the III–V wafer structure employed in the work of Fang et al. (see the detailed epiwafer structure in Table 1 of [20]) is used here as an example. The thickness of the separate confinement heterostructure (SCH) layer and the n -layer are modified to be 80 and 200 nm, respectively, to increase the modal confinement to the quantum wells. Additionally, we will design the Si waveguide to be a ridge rather than a rib waveguide to facilitate the coupling between the III–V and Si.

The supermodes of the hybrid waveguides arise from the coupling between all the original modes of the III–V waveguide and the Si waveguide. However, we are interested in the two lowest-order supermodes, which result from the coupling between the fundamental modes of the III–V and the Si waveguides. In the simulation, the III–V waveguide has a width of 3.30 μm . The effective index n_{eff} is 3.2588 at the wavelength 1.55 μm as calculated with a mode solver. Figure 2.3(a) and (b) show the index profile and the fundamental mode of the III–V waveguide. For Si waveguide, we use a typical SOI ridge waveguide with a fixed height H and a longitudinally varying width W . Figure 2.3(c) and (d) show the index profile and the fundamental mode of the SOI waveguide. The composite hybrid structure consists of the III–V and Si waveguides separated by a 10-nm-thick layer of silica, as shown in Fig. 2.4(a). The thin silica layer is considered to assist in a low-temperature wafer bonding process [19]. Figure 2.4(b) through (g) show the modal

profiles of the even and odd supermodes of the hybrid waveguides in the three representative cases. The phase-matching condition ($\delta \rightarrow 0$) is satisfied in Fig. 2.4(d) and (e) where the Si waveguide has a height $H = 0.84 \mu\text{m}$ and a width $W = 0.65 \mu\text{m}$ with n_{eff} of 3.2529. In this case, for both even and odd supermodes, the modal power is roughly evenly divided between the III–V and the Si waveguides, as predicted by the supermode theory.

Now we understand that the even and odd supermodes coexist in the coupled-waveguide system, though propagating at different phase velocities. In practice, we want a single mode to be in operation in such a system. We can separate the two supermodes by adiabatically tapering the Si waveguide width to provide different amount of feedback to different modes. Only the mode having stronger feedback will lase. Figure 2.5(a) shows the confinement factors in the active region (including quantum wells and barriers in between) Γ_{act} , and in the Si waveguide Γ_{Si} , for the lowest-order even supermode, as a function of the Si waveguide width W . Figure 2.5(b) plots the confinement factors in the whole III–V waveguide $\Gamma_{\text{III-V}}$ and in the Si waveguide Γ_{Si} , and the mismatch parameter δ as a function of Si waveguide width W . As expected, these three curves intersect at one point where the phase is matched ($\delta \rightarrow 0$) and the modal power is also evenly distributed in each waveguide. Figure 2.5(c) displays the absolute value of the mismatch parameter $|\delta|$ and the coupling coefficient κ in the same plot so that their magnitudes can easily be compared.

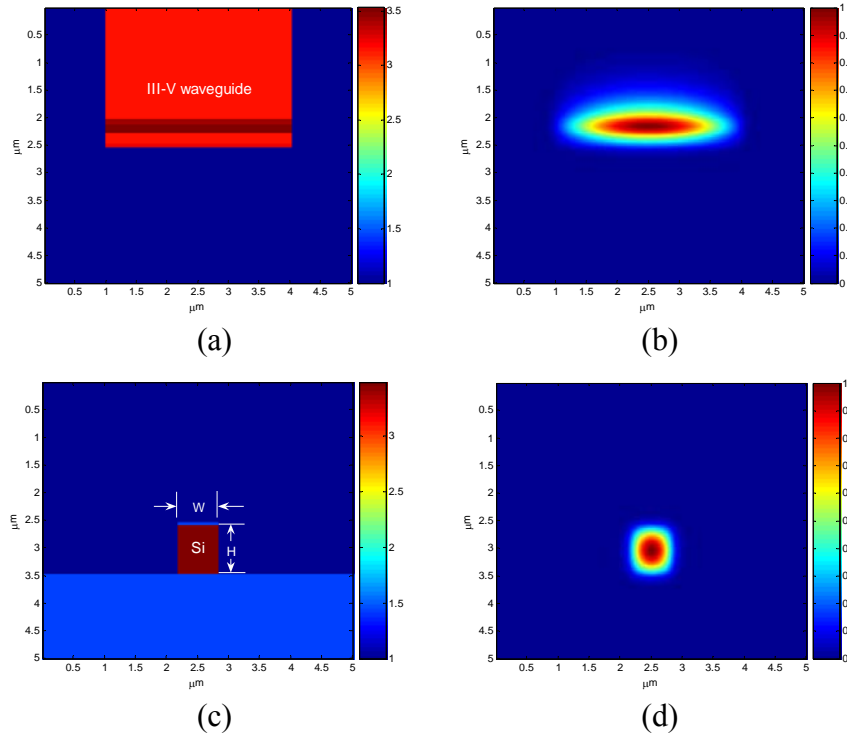


Fig. 2.3. (a) Index profile of the III-V waveguide. (b) Fundamental mode of the III-V waveguide. (c) Index profile of the Si waveguide. (d) Fundamental mode of the Si waveguide.

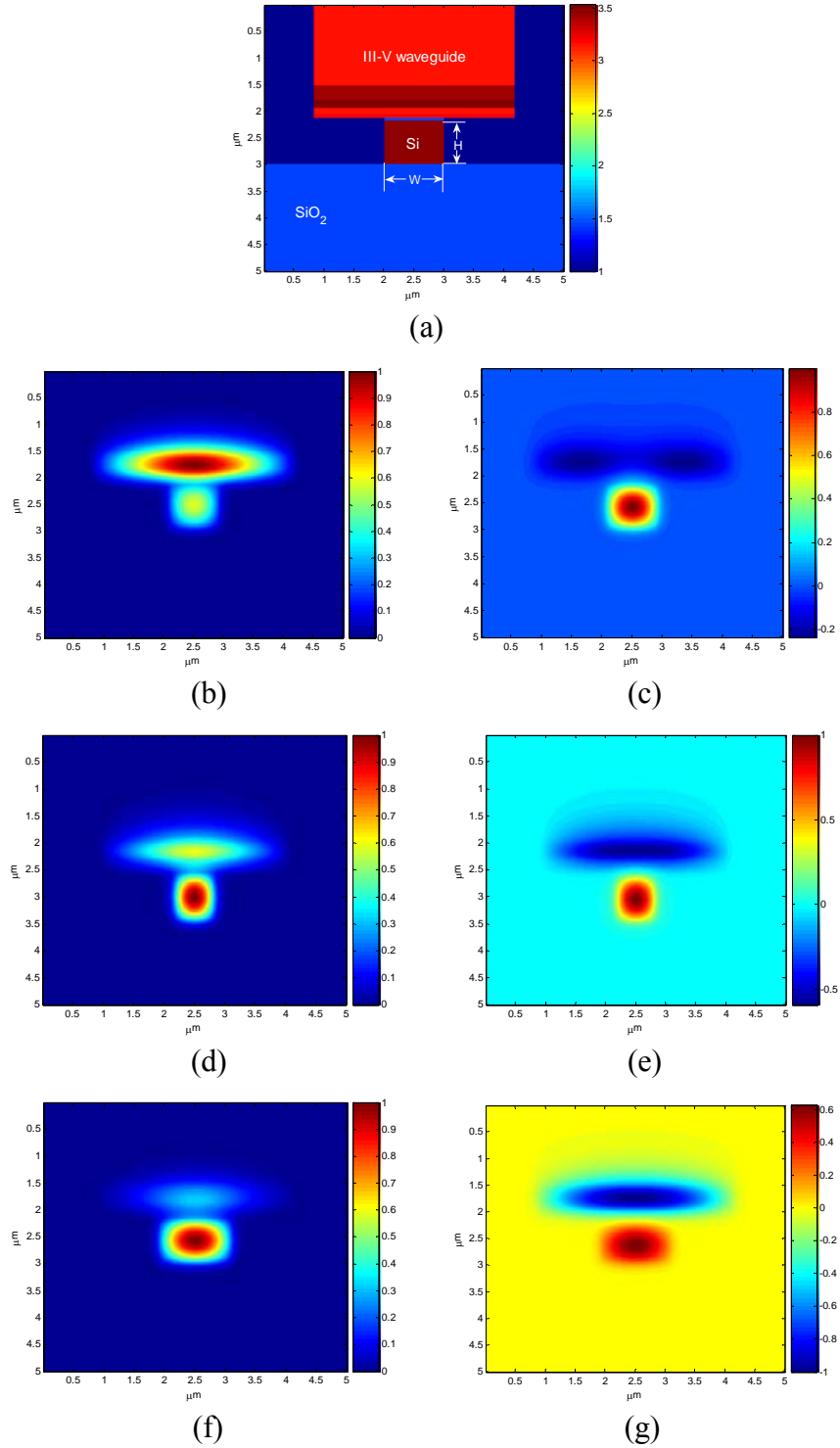
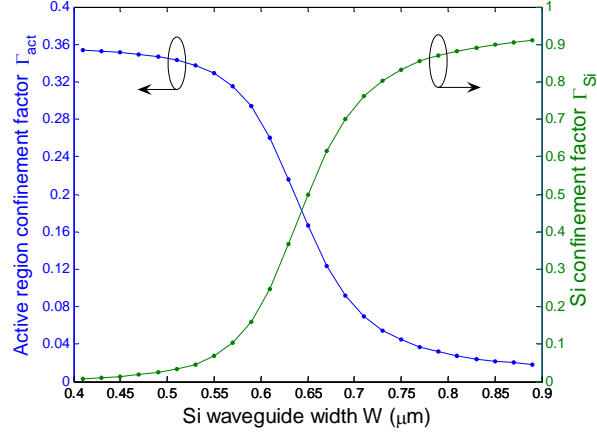
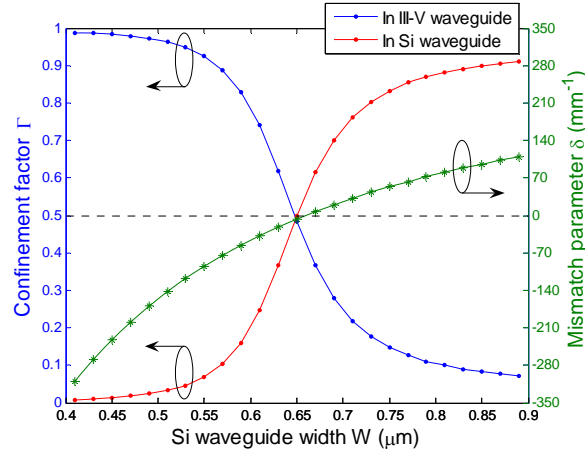


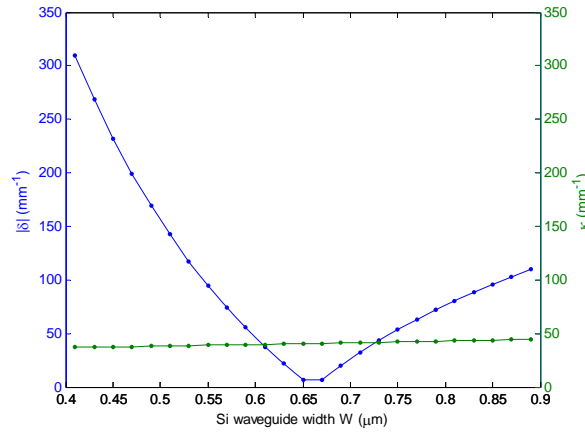
Fig. 2.4. (a) Index profile of the coupled-waveguide system. (b), (d), (f) Even supermode and (c), (e), (g) odd supermode of the coupled-waveguide system as the Si waveguide width W is increased. The phase-matching condition is achieved in (d) and (e) where $\delta \rightarrow 0$ and the modal power in the III-V and Si waveguides is evenly distributed.



(a)



(b)



(c)

Fig. 2.5. (a) Confinement factors in the active region (Γ_{act}) and in the Si waveguide (Γ_{Si}) as a function of the Si waveguide width W . (b) Confinement factors in the III-V ($\Gamma_{\text{III-V}}$) and Si waveguide (Γ_{Si}), and the mismatch parameter δ as a function of the Si waveguide width W . (c) Calculated values of $|\delta|$ and κ as a function of the Si waveguide width W .

2.3 Proposal of Supermode Si/III–V Lasers and Beyond

As shown in Figs. 2.4 and 2.5, with a proper choice of the Si waveguide width, we can direct the modal power to the amplifying III–V waveguide or to the Si waveguide, thereby avoiding the degraded performance that results from the reliance on the evanescent field. At the in/out coupling regions, the modal power is diverted to the Si waveguide by adiabatically increasing its width. This makes for efficient coupling to the

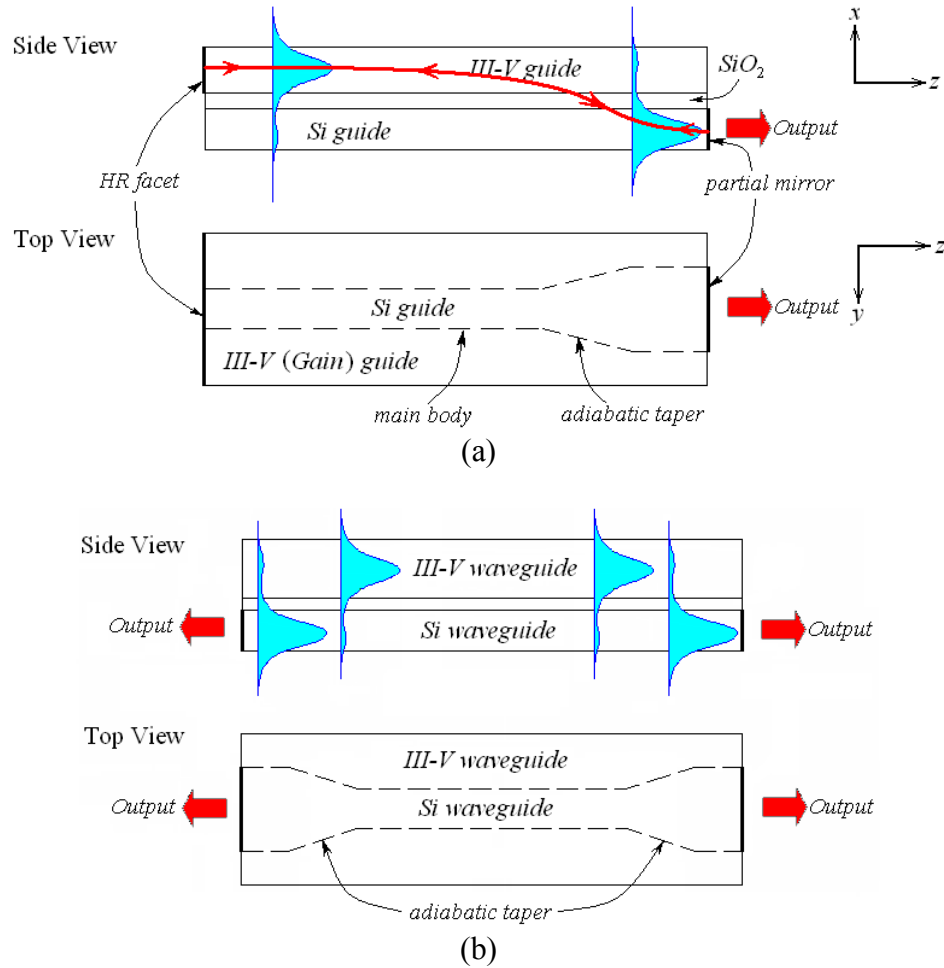


Fig. 2.6. Two configurations of supermode Si/III–V lasers. (a) Asymmetric: one adiabatic taper, output comes only from the right Si end facet. (b) Symmetric: two adiabatic tapers, output comes from both left and right Si end facets.

outside Si photonic circuit.

As marked with the red line in Fig. 2.6(a), the mode starts propagating from left to right in the upper left III–V waveguide where it is amplified. It then enters the adiabatic transformer section where the width of the Si waveguide increases so as to cause δ to change from $\delta < 0$ to $\delta > 0$. This causes the modal power to shift to the lower low-loss Si waveguide where it is partially reflected from the right output facet. The reflected field retraces its path till reflected from the upper left facet thus completing the round trip. The other mode is suppressed due to the high distributed loss along the path and the absence of feedback mechanism. A considerable enhancement of modal gain is the most direct advantage of the supermode control. Based on the calculated modal confinement factors in the active region Γ_{act} and in the Si waveguide Γ_{Si} for different Si waveguide widths [Fig. 2.5(a)], the modal gain can be increased up to five times, if the adiabatic tapers are efficient in mode transformation and designed as short as possible [26].

The main advantage of this “spatial switching” of the modal power is to obtain maximum achievable gain from the inverted medium since the peak modal field and not just an evanescent tail induce the amplifying transitions in the gain (III–V) region. Bearing in mind the idea of supermode control, we can make another laser configuration [Fig. 2.6(b)] that is more symmetric in the longitudinal extension. The laser light emits from both left and right Si end facets, and two adiabatic tapers are used to transform the supermode between Si and III–V.

With a little modification, the same principle of spatial switching of the modal power can be used to make other functional devices. We can also have supermode optical amplifier, modulator, and photodetector. To make an optical amplifier or modulator

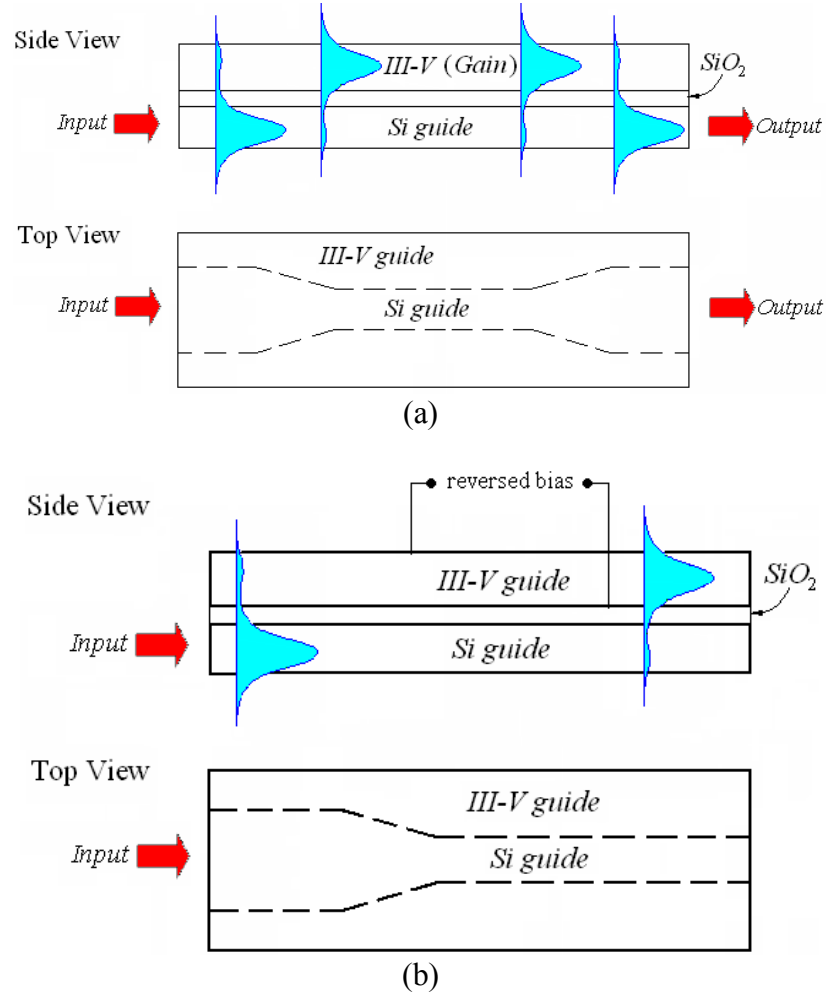


Fig. 2.7. (a) Supermode Si/III-V optical amplifier. (b) Supermode Si/III-V photodetector.

[Fig. 2.7(a)], light is first coupled into the Si waveguide ($\delta > 0$), then switched to the upper III-V section ($\delta < 0$) for amplification or modulation, finally coupled back to Si waveguide ($\delta > 0$) for output coupling. This principle can also be applied to make a photodetector [Fig. 2.7(b)]: as the light is spatially switched from the Si waveguide to the upper III-V waveguide, which under reversed bias is highly absorbing, extra electron-hole pairs will be

excited across the p - n junction contributing to the conductivity, which reflects in the change of current in the outside electric circuit.

It is envisioned that once the individual optical functional devices are achieved in a much more efficient fashion by using the supermode control, the next-generation, large-scale, high-efficiency Si/III-V hybrid circuitry will not be far away (see Fig. 2.8), and we expect a thorough revolution in the development of optical communications.

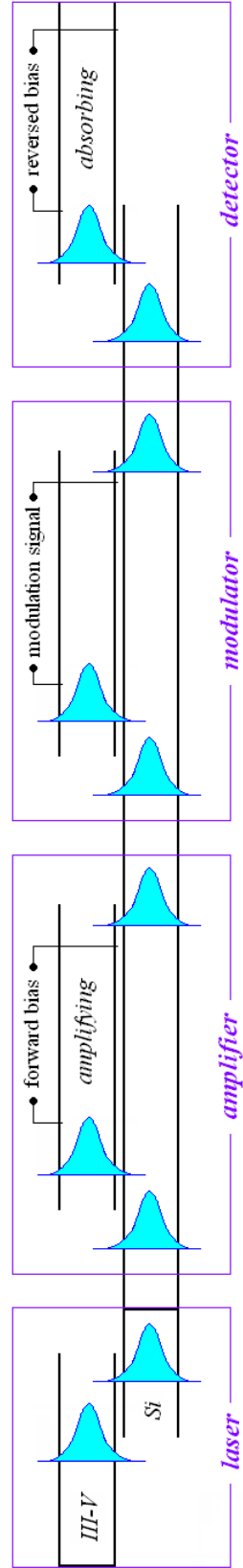


Fig. 2.8. Conception of future large-scale, high-efficiency hybrid optoelectronic circuitry. Devices with different optical functions can be integrated on the Si platform. The light transportation from one module to another can be on-chip by Si waveguides or chip-to-chip by optical fibers.

Chapter 3

Adiabaticity Theorem and the Shortest Adiabatic Taper Design

In Chapter 2 we have shown that as the refractive index profile $n(x, y)$ of the coupled-waveguide system varies along the longitudinal direction (z), the corresponding local normal modes (supermodes) $E_e(x, y)$ and $E_o(x, y)$ will change accordingly. For such longitudinally variant waveguide structure, these supermodes are actually z dependent, and each cross section of the waveguide system has its own set of supermodes. In analogy to the famous adiabaticity theorem in quantum mechanics, if the change in $n(x, y)$, which can be the variation in waveguide geometry and/or refractive index, is *slow enough* along the propagation direction (z), we are able to approximate the solutions of the Maxwell equations in the real configuration by means of “stationary” supermodes of the local waveguide structure. In such a case, a particular supermode at a z plane will go over continuously into the corresponding supermode at any other z plane.

One question arises: How slow is considered “slow enough”? The answer to this question is definitely nontrivial and is at the heart of designing the supermode hybrid circuits for maximal device performance. Obviously the transforming region that connects the two states $[\delta < 0, |\delta| \gg \kappa]$ and $[\delta > 0, |\delta| \gg \kappa]$ should be designed to be as short as

possible while keeping the scattering to other unwanted modes as low as possible. In this chapter we derive a universal criterion for designing such adiabatic mode transformers based on a perturbation approach. The criterion relates ε , the fraction of power scattered into the unwanted mode, to waveguide design parameters and gives the shortest possible length of an adiabatic mode transformer that is approximately $2/\pi\varepsilon^{1/2}$ times the distance of maximal power transfer between the waveguides. After that the numerical results obtained based on a transfer-matrix formalism are presented to support this theoretical derivation.

This chapter is reproduced and adapted with permission from [28], © 2009 OSA.

3.1 Derivation of the Adiabaticity Criterion

Mode transformers have been widely used in optical communications to efficiently route and transmit light between different optical functional devices on a chip or from an on-chip device to an optical fiber. By varying the modal shape and size from input to output, these transformers enable efficient and alignment-tolerant coupling between different components and thus reduce the packaging costs. During the past two decades, they have been extensively studied in the form of tapered fibers [29, 30], and “spot-size converter” (also referred to as “mode converter/expander/adaptor”) integrated laser diodes [31, 32], modulators [33, 34], optical amplifiers [35], WDM filters [36], and optical switches [37]. Nowadays, with the development of new concepts and techniques, coupling of light between different photonic devices in hybrid material systems assumes an ever increasing importance [25, 38-40].

Two schemes have been implemented to realize the mode transformation—resonant coupling and adiabatic coupling. In a resonant coupler, optical power is mostly distributed in the fundamental and the second-order supermodes of the coupled-waveguide system; by designing the coupling region to be of a half beat length, the light transfers from one waveguide to the other [40]. The coupler length can be made very short in this manner, however, the beat length depends critically on the refractive indices and the dimensions of the waveguides. In practice there are always unavoidable variations in layer composition, thickness and feature dimensions during material growth and device fabrication. Moreover, the refractive indices also depend on injected current levels for an active device. These uncertainties make it practically difficult to determine the exact beat length, rendering the efficiency of power transfer uncertain and the resulting devices of dubious value. An adiabatic coupler, on the other hand, does not require a precise definition of power-transfer length [30, 41, 42]. By changing the geometry of the waveguides gradually, an optical field that is launched into a local mode (supermode) at the input will remain in the local mode even as the waveguide parameters change. This can be used to move the optical power spatially from one waveguide to the other. The downside of an adiabatic coupler is that it has to be sufficiently long to satisfy the adiabatic condition to reduce the coupling of power into other unwanted modes. Clearly a longer coupler not only reduces the component density, but also suffers from higher transmission losses, such as the material absorption and sidewall roughness scattering, and higher probability of material defects and fabrication imperfections. Therefore it is desirable to design the shortest possible adiabatic coupler given the maximal tolerated scattering from the wanted mode into other modes during power transfer.

The optimal design procedure of adiabatic mode transformers has been proposed in different ways. Love et al. first studied the fiber tapers, suggesting that for a given taper length the optimal delineating curve should have the local taper angle inversely proportional to the local beat length [30, 43]. This design principle was also employed in [42] and [44] in experiments. Another design concept is based on equalization of the single step loss (defined as the overlap integral of the modes in two adjacent segments) along the taper [45, 46]. Since those analyses depended on the stationary field distributions and did not include the wave propagation behavior, they did not point out the optimal taper length with which a certain coupling efficiency could be achieved. Taking into account the supermode propagating behavior, we will derive a universal criterion for the adiabatic mode transition in a coupled-waveguide system and suggest the shortest possible length of an adiabatic mode transformer for any given power transfer efficiency.

The mode transformer to be analyzed here is based on a coupled-waveguide system shown in Fig. 3.1. It consists of two waveguides, namely waveguide **1** and waveguide **2**, placed in close proximity to each other. The refractive index or geometry of at least one waveguide is gradually varied along the propagation direction z . Light is coupled into this transformer at input plane $z = z_i (= 0)$ and out at output plane $z = z_f$. As discussed in Chapter 2, the normalized local modes (or “supermodes”), denoted as \mathbf{e}_e for the even mode and \mathbf{e}_o for the odd mode, of this coupled-waveguide system are expressed as column vectors with their components denoting the amplitudes of the two individual uncoupled waveguide modes respectively [47],

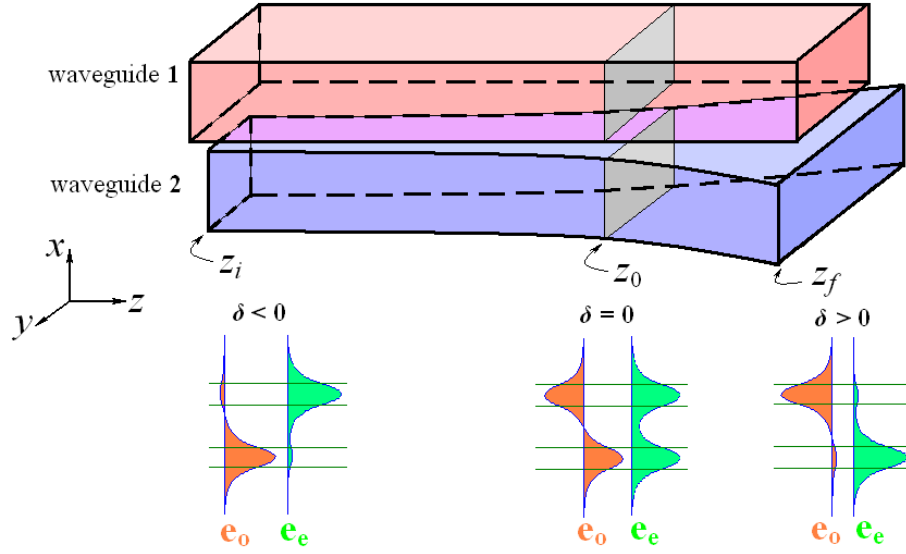


Fig. 3.1. Model of the adiabatic mode transformer based on two coupled waveguides **1** and **2**, placed in close proximity to each other. The geometry of waveguide **2** is gradually varied along the z direction. Light is coupled in at plane $z = z_i$ ($= 0$) and out at plane $z = z_f$. The modal profiles of the local modes \mathbf{e}_e and \mathbf{e}_o are listed at the input, phase-matching, and output planes.

$$\mathbf{e}_e(z) = \frac{1}{\sqrt{2}} \begin{pmatrix} \left(1 - \frac{\delta}{S}\right)^{\frac{1}{2}} \\ \left(1 + \frac{\delta}{S}\right)^{\frac{1}{2}} \end{pmatrix} e^{-i\beta_e z} = \tilde{\mathbf{e}}_e e^{-i\beta_e z} \text{ and } \mathbf{e}_o(z) = \frac{1}{\sqrt{2}} \begin{pmatrix} -\left(1 + \frac{\delta}{S}\right)^{\frac{1}{2}} \\ \left(1 - \frac{\delta}{S}\right)^{\frac{1}{2}} \end{pmatrix} e^{-i\beta_o z} = \tilde{\mathbf{e}}_o e^{-i\beta_o z}, \quad (3.1)$$

where $\delta = (\beta_2 - \beta_1)/2$ is the mismatch of propagation constants between the individual uncoupled waveguide modes, $2S = 2(\delta^2 + \kappa^2)^{1/2} = \beta_e - \beta_o$ is the difference of propagation constants of the supermodes, and κ is the coupling strength between waveguides **1** and **2**. Figure 3.2 plots the corresponding dispersion curve of the propagation constants along z . Note that the modal profiles (3.1) of the supermodes are z dependent through the parameters δ and S . For both supermodes \mathbf{e}_e and \mathbf{e}_o , when $\delta < 0$ and $|\delta| \gg \kappa$, the mode substantially resides in one waveguide, and when $\delta > 0$ and $\delta \gg \kappa$, the mode is

substantially in the other waveguide. At the phase-matching point z_0 where $\delta = 0$ the optical power is evenly distributed in the two waveguides [25]. Our task is to design this coupled-waveguide system such that a supermode can transform adiabatically in the shortest distance with the parameter δ sweeping from a negative value to a positive value, while keeping the coupling to the other supermode below a certain level.

The total field in the mode transformer can be expressed as a linear combination of the supermodes with their phases accumulated,

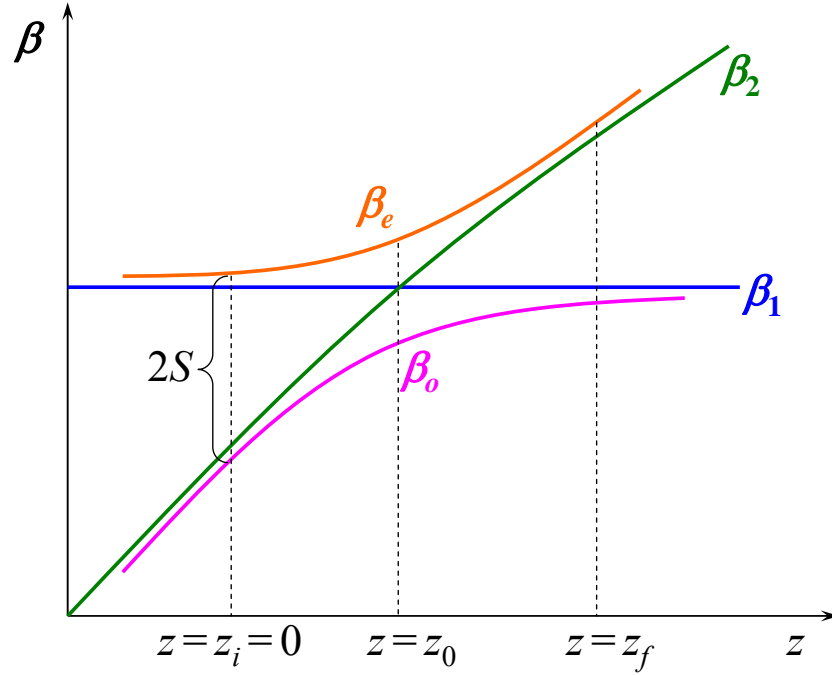


Fig. 3.2. Dispersion curves of the propagation constants along z . β_1 and β_2 correspond to the propagation constants of the individual uncoupled waveguide modes. They cross at the phase-matching point z_0 . β_e and β_o are the propagation constants of the even and odd supermodes of the coupled-waveguide system. $2S = \beta_e - \beta_o$ denotes the difference between them. At the phase-matching point z_0 the optical power is evenly distributed in the two waveguides for both even and odd supermodes.

$$\mathbf{E}(z) = \sum_{j=e,o} a_j(z) \tilde{\mathbf{e}}_j \exp \left[-i \int_0^z \beta_j(z') dz' \right]. \quad (3.2)$$

Considering a guided optical wave paraxially propagating along the $+z$ direction in a slowly varying waveguide, the total field satisfies the Fresnel equation [48],

$$i \partial_z \mathbf{E}(z) = \hat{B} \mathbf{E}(z), \quad (3.3)$$

where \hat{B} is the Fresnel operator. The local modes $\mathbf{e}_e(z)$ and $\mathbf{e}_o(z)$ shown in (3.1) by their definitions satisfy

$$\hat{B} \tilde{\mathbf{e}}_e(z) = \beta_e(z) \tilde{\mathbf{e}}_e(z), \quad \hat{B} \tilde{\mathbf{e}}_o(z) = \beta_o(z) \tilde{\mathbf{e}}_o(z). \quad (3.4)$$

Introducing (3.2) into (3.3) and utilizing (3.4) yield

$$\sum_{j=e,o} \left[\left(\partial_z a_j \right) \tilde{\mathbf{e}}_j + a_j \left(\partial_z \tilde{\mathbf{e}}_j \right) \right] \exp \left[-i \int_0^z \beta_j(z') dz' \right] = 0. \quad (3.5)$$

Without loss of generality, if we consider the case of adiabatically transforming the mode \mathbf{e}_e , then only \mathbf{e}_e is excited and the power coupled into \mathbf{e}_o is negligible, we can take $a_e \approx 1$ and $a_o \approx 0$ so that (3.5) becomes

$$\left(\partial_z a_o \right) \tilde{\mathbf{e}}_o \exp[2i\bar{S}z] + \left(\partial_z a_e \right) \tilde{\mathbf{e}}_e + \partial_z \tilde{\mathbf{e}}_e = 0, \quad (3.6)$$

where $\bar{S}(z) = \frac{1}{z} \int_0^z S(z') dz'$ and $S = (\beta_e - \beta_o)/2$. Taking the inner product of (3.6) with $\tilde{\mathbf{e}}_o^*$

yields $\frac{da_o}{dz} = -(\tilde{\mathbf{e}}_o^* \cdot \partial_z \tilde{\mathbf{e}}_e) e^{-2i\bar{S}z}$. Introducing a normalized mismatch parameter $\gamma \equiv \delta/\kappa$, it can

be shown from (3.1) that $\tilde{\mathbf{e}}_o^* \cdot \partial_z \tilde{\mathbf{e}}_e = \frac{1}{2(1+\gamma^2)} \frac{d\gamma}{dz}$. Then we have

$$\frac{da_o}{dz} = \left(\frac{1}{4i\kappa(1+\gamma^2)^{3/2}} \frac{d\gamma}{dz} \right) \frac{d}{dz} \left(e^{-2i\bar{S}z} \right), \quad (3.7)$$

where $\frac{d}{dz}(\bar{S}z) = S$ and $S = \kappa(1 + \gamma^2)^{1/2}$ have been used. Since the factor in the first bracket

in the right-hand side of (3.7) varies slowly compared to the exponential term $e^{-i\bar{S}z}$, Eq.

(3.7) is integrated over z resulting in $a_o = -\left(\frac{1}{2\kappa(1 + \gamma^2)^{3/2}} \frac{d\gamma}{dz}\right) e^{-i\bar{S}z} \sin(\bar{S}z)$, so that

$$|a_o| \leq \frac{1}{2\kappa(1 + \gamma^2)^{3/2}} \frac{d\gamma}{dz}, \quad (3.8)$$

which imposes an upper bound on the amplitude of a_o .

In an adiabatic mode transformer, we require that the fraction of power in the unwanted mode \mathbf{e}_o be less than a certain value ε or, equivalently $|a_o| < \varepsilon^{1/2}$ along the propagation. Following (3.8), we arrive at the *adiabaticity criterion* in this two-mode coupled-waveguide system,

$$\frac{1}{2\kappa(1 + \gamma^2)^{3/2}} \frac{d\gamma}{dz} \leq \varepsilon^{1/2}. \quad (3.9)$$

3.2 Design of the Shortest Adiabatic Mode Transformer in a Coupled-Waveguide System

Since we are aiming at the shortest possible adiabatic mode transformer, we want $\frac{d\gamma}{dz}$ to be

as large as possible provided (3.9) is satisfied. In the case that the separation between the two waveguides does not change, κ depends very weakly on the variation of structure and can be regarded as a constant [see Fig. 2.5(c)]. It is straightforward to show that the largest

possible $\frac{d\gamma}{dz}$ is achieved when $\frac{1}{2\kappa(1 + \gamma^2)^{3/2}} \frac{d\gamma}{dz} = \varepsilon^{1/2}$, the solution of which is

$$\gamma = \frac{2\kappa\varepsilon^{1/2}(z-z_0)}{\sqrt{1-(2\kappa\varepsilon^{1/2}(z-z_0))^2}} = \tan\left[\arcsin\left(2\kappa\varepsilon^{1/2}(z-z_0)\right)\right], \quad (3.10)$$

where z_0 is the phase-matching point corresponding to a zero γ . If κ cannot be regarded as a constant, then the factor $\kappa(z-z_0)$ should be replaced by $\int_{z_0}^z \kappa(z')dz'$ in (3.10). It follows from (3.10) that as $z-z_0$ varies from $-\frac{1}{2\kappa\varepsilon^{1/2}}$ to $\frac{1}{2\kappa\varepsilon^{1/2}}$, γ covers $-\infty$ to ∞ , which means that the mode \mathbf{e}_e transfers from being localized completely in waveguide **1** to waveguide **2**. A transformer designed following (3.10) with length $L = \frac{1}{\kappa\varepsilon^{1/2}}$ can transform the mode \mathbf{e}_e from waveguide **1** at the input to waveguide **2** at the output with the fraction of power of the unwanted mode \mathbf{e}_o below ε . In other words, with this optimal design, ε has the least value $\left(\frac{1}{\kappa L}\right)^2$, which is in agreement with previous studies indicating the scattered power being proportional to L^{-2} [41]. Considering that in a resonant coupler the distance of maximal power transfer from one waveguide to the other is $\frac{\pi}{2\kappa}$, it takes approximately $\frac{2}{\pi\varepsilon^{1/2}}$ times this distance to adiabatically transform the wanted mode \mathbf{e}_e . It should be noted that this ratio is κ independent, which is about 6.37, for example, if we assume $\varepsilon = 0.01$.

3.3 Numerical Verification

To verify the above theory, we employ a transfer-matrix formalism to investigate the coupling efficiency of adiabatic mode transformers with different distributions of γ along z . For the coupled-waveguide system shown in Fig. 3.1, the amplitudes of each waveguide mode, $b_1(z)$ and $b_2(z)$, satisfy the coupled-mode equations,

$$\frac{d}{dz} \begin{bmatrix} b_1 \\ b_2 \end{bmatrix} = \begin{bmatrix} -i\beta_1 & -i\kappa \\ -i\kappa & -i\beta_2 \end{bmatrix} \begin{bmatrix} b_1 \\ b_2 \end{bmatrix} \equiv \mathbf{C} \begin{bmatrix} b_1 \\ b_2 \end{bmatrix}, \quad (3.11)$$

which leads to the transfer relation for small Δz ,

$$\begin{bmatrix} b_1(z + \Delta z) \\ b_2(z + \Delta z) \end{bmatrix} = \exp(\mathbf{C}(z) \cdot \Delta z) \begin{bmatrix} b_1(z) \\ b_2(z) \end{bmatrix}, \quad (3.12)$$

where

$$\mathbf{C}(z) = -i\bar{\beta}(z)\mathbf{I} + i\kappa \begin{bmatrix} \gamma(z) & -1 \\ -1 & -\gamma(z) \end{bmatrix},$$

with \mathbf{I} being the identity matrix and $\bar{\beta} = (\beta_1 + \beta_2)/2$. Only the second term in the expression of $\mathbf{C}(z)$ is important since the first term just provides an overall phase factor for both b_1 and b_2 . Light is launched into the transformer at the input plane z_i with the mode substantially resident in waveguide **1** so that $b_1(z_i) = 1$ and $b_2(z_i) = 0$. The coupling efficiency of the mode transformer is defined as $|b_2(z_f)|^2$, the fraction of power in waveguide **2** at the output plane z_f . We may take κ to be 40 mm^{-1} , as calculated from the Si/III–V coupled-waveguide structure used for simulation in Section 2.2 [see Fig. 2.5(c)], and assume a practical γ to vary from -10 to 10 across the mode transformer. Figure 3.3 plots in blue the coupling efficiency as a function of the transformer length $L (= z_f - z_i)$ for devices designed with γ distributed along z according to (3.10). A transformer with length $L = 200 \text{ }\mu\text{m}$ is sufficiently adiabatic to transfer the power from waveguide **1** to waveguide **2**. Using $\kappa = 40 \text{ mm}^{-1}$ and $L = 200 \text{ }\mu\text{m}$, the fraction of power scattered from \mathbf{e}_e to \mathbf{e}_o is $(\frac{1}{8})^2$ based on $\varepsilon = (\frac{1}{\kappa L})^2$. The length ratio between this adiabatic coupler and a resonant coupler should be $\frac{2}{\pi\varepsilon^{1/2}} \approx 5.09$. However, as seen from the oscillatory behavior of the blue curve, the

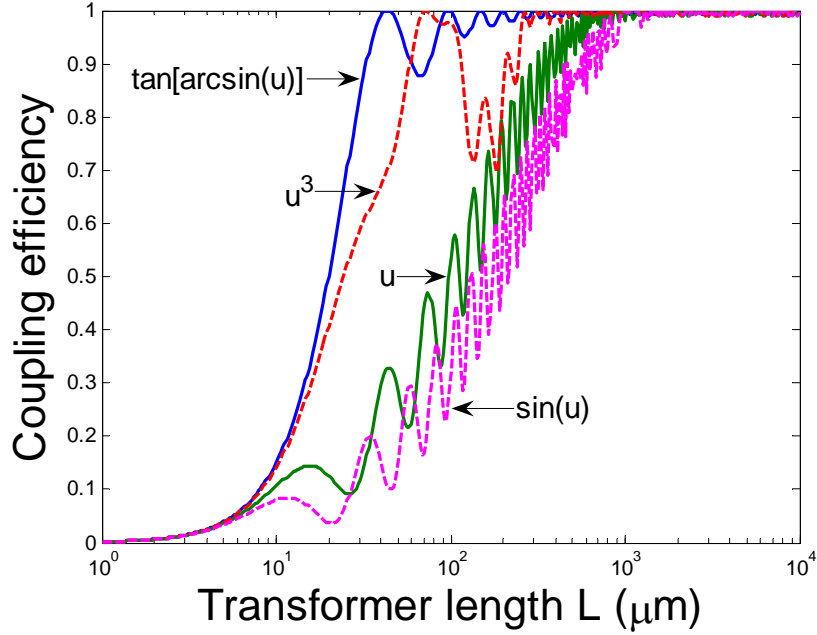


Fig. 3.3. Coupling efficiency as a function of the transformer length $L (= z_f - z_i)$ for devices designed with γ distributions of $\tan[\arcsin(u)]$, u , u^3 , and $\sin(u)$ where u is proportional to $z - z_0$. The coupling strength κ is taken to be 40 mm^{-1} and the normalized mismatch parameter γ is assumed to vary from -10 to 10 across the mode transformer. The optimal design with γ distributed with $\tan[\arcsin(u)]$ has the least length for adiabatic mode transformation.

length $200 \text{ } \mu\text{m}$ appears to be 7 times the distance of maximal power transfer between the waveguides. The discrepancy is considered to be attributed to the shortened effective resonant coupling length since the local coupling length is $\frac{\pi}{2S}$ rather than $\frac{\pi}{2\kappa}$, and $S \geq \kappa$. Also displayed in Fig. 3.3 are the coupling efficiencies for devices with γ distributed according to some common odd functions such as u , u^3 , and $\sin(u)$ (here u is proportional to $z - z_0$), all of which require a substantially longer coupler than in the case of the optimal distribution $\tan[\arcsin(u)]$ for adiabatic mode transformation.

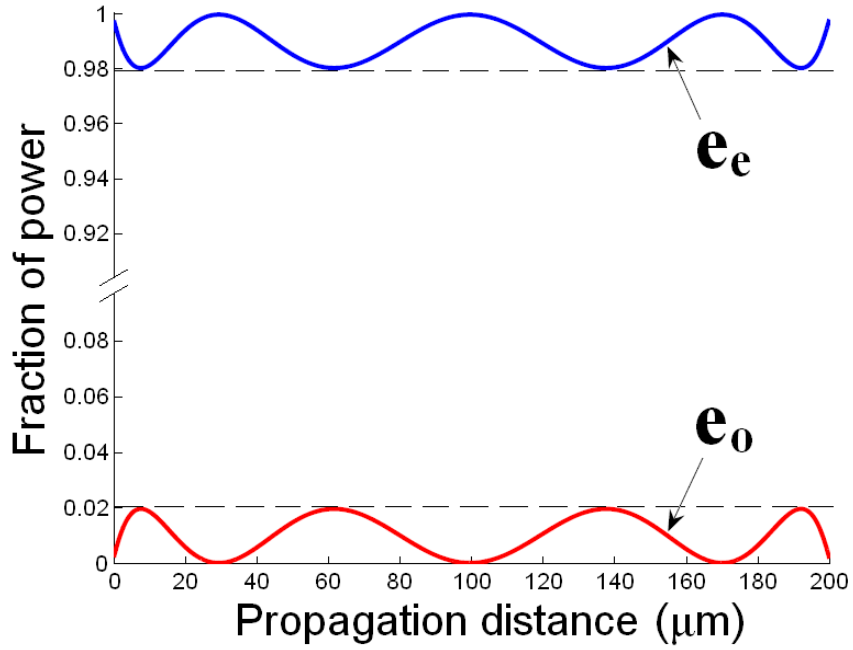


Fig. 3.4. Fraction of power in the wanted (even) and unwanted (odd) supermodes along the propagation direction in a 200- μm -long mode transformer with the optimal design. The equiripple behavior of both modes indicates that the total scattered power into the odd mode is minimized.

The fundamental reason that an adiabatic mode transformer favors the $\tan[\arcsin(u)]$ -shaped γ distribution is that only by following this distribution can the power scattered into the unwanted mode have the smallest least upper bound, which minimizes the total scattering of power into the unwanted mode. In this numerical case, since the γ value of -10 leads to $|a_o| \approx \frac{1}{20}$ at the input plane z_i and the fraction of power coupled from \mathbf{e}_e to \mathbf{e}_o is $(\frac{1}{8})^2$ during the transformation, it is expected that at the output plane z_f the maximal fraction of power in the mode \mathbf{e}_o satisfies $(\frac{1}{8} - \frac{1}{20})^2 \leq |a_o|_{\max}^2 \leq (\frac{1}{8} + \frac{1}{20})^2$, the specific value depending on the propagation phase in the transformer. Figure 3.4 shows the fraction of power in the wanted (even) and unwanted (odd) supermodes calculated from the transfer-

matrix method for a 200- μm -long mode transformer with the optimal shape. The equiripple behavior of both modes is evident, and the fraction of power in the odd supermode is bounded by 0.02, which falls in the expected range.

In conclusion, we derived a universal criterion for designing adiabatic mode transformer based on the supermode control in a coupled-waveguide system. By optimally distributing the design parameter γ along the light propagation direction z , we obtain the shortest possible adiabatic mode transformer needed to keep the fraction of power scattered into the unwanted mode below ε . This length is approximately $2/\pi\varepsilon^{1/2}$ times the distance of maximal power transfer between the two waveguides. The numerical calculations based on a transfer-matrix formalism compared coupling efficiency of devices with different designs and demonstrated the superiority of the optimal design.

Chapter 4

Device Design and Fabrication

This chapter is reproduced and adapted with permission from [49, 50], © 2009, 2010 OSA.

4.1 Device Design

Choosing III–V Material System

As we have elaborated in previous chapters, the hybrid laser consists of a III–V waveguide in close proximity (by wafer bonding) to a Si waveguide. The first step in device design is to choose an appropriate III–V material system and design the specific layers for efficient conversion of injected current to light emission.

The AlGaInAs material system as used in [20] is advantageous in uncooled laser operation at high temperatures, due to the large conduction band offset [51]. However, high-quality AlGaInAs layers are relatively more difficult to obtain, and the reliability of Al containing lasers remains a concern [51, 52]. In addition, Al alloys could be prone to nonradiative surface recombination, which may elevate the lasing threshold current. In our work we choose InGaAsP quaternary compounds as the III–V material.

Table 4.1. InGaAsP epiwafer layer structure

Layer	Material	Thickness (nm)	Bandgap (eV)	Doping (cm ⁻³)
<i>p</i> -side contact layer	<i>p</i> -In _{0.53} Ga _{0.47} As	200	0.77	$p > 10^{19}$
Upper cladding layer	<i>p</i> -InP	1500	1.34	$p = 10^{18} \rightarrow 5 \times 10^{17}$
Separate confinement layers	InGaAsP InGaAsP	40 40	1.08 0.99	undoped
Quantum wells (1% compressive strain)	InGaAsP ($\times 5$)	7	0.83	
Barriers (0.3% tensile strain)	InGaAsP ($\times 4$)	10	0.99	
Separate confinement layers	InGaAsP InGaAsP	40 40	0.99 1.08	
<i>n</i> -side contact layer	<i>n</i> -InP	110	1.34	$n = 10^{18}$
Superlattice	<i>n</i> -InGaAsP ($\times 2$)	7.5	1.13	$n = 10^{18}$
	<i>n</i> -InP ($\times 2$)	7.5	1.34	$n = 10^{18}$
Bonding layer	<i>n</i> -InP	10	1.34	$n = 10^{18}$

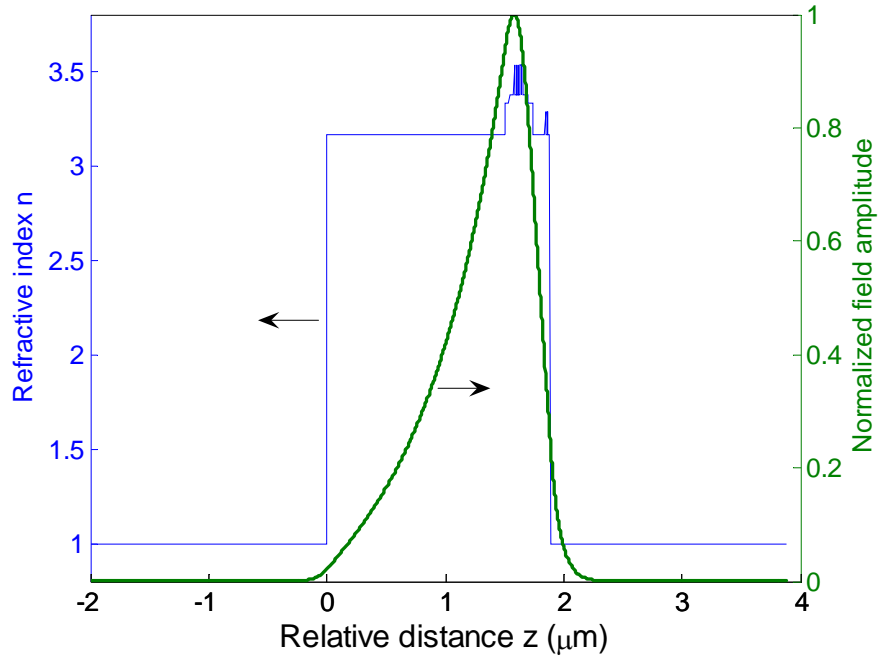


Fig. 4.1. Refractive index profile and optical mode profile of the InGaAsP epilayer.

Table 4.1 lists the InGaAsP epiwafer layer structure. This design facilitates the dual confinement of photons and electrons in vertical (layer growth) direction. Figure 4.1 plots the corresponding refractive index profile and optical mode profile of the InGaAsP epilayer.

Designing the SOI wafer

Since high-quality SOI wafers are commercially available, the Si waveguide as a part of our lasers should naturally be designed based on this platform. For the previous given InGaAsP epiwafer structure (Table 4.1), the SOI waveguides have to be designed accordingly.

As described in detail in Chapter 2, altered Si waveguide width changes its effective index, thus can vary the fractions of modal power in both the III–V and the Si waveguide to achieve the supermode transform. However, for a given Si waveguide height (or, the thickness of the Si device layer of a SOI wafer), there is an upper limit for the maximally achievable fraction of modal power in Si, which corresponds to an infinite width, i.e., a slab waveguide. Figure 4.2(a) illustrates the slab waveguide model and Fig. 4.2(b) plots the maximal fraction of power in Si waveguide as a function of the Si waveguide height. To enable the supermode transform (i.e., to achieve a large range of variation of the modal confinement), the Si waveguide height must be larger than 0.7 μm . This means we have to choose a SOI wafer with its Si device layer thicker than 0.7 μm .

To be conservative, in our experiment we choose a SOI wafer with 0.9- μm -thick Si device layer on 2- μm -thick buried SiO_2 oxide layer.

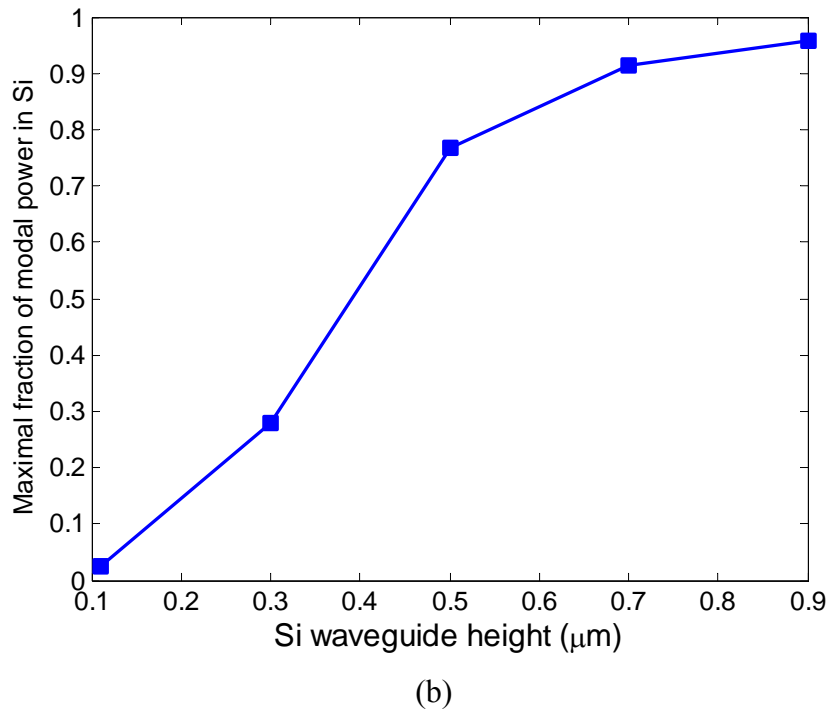
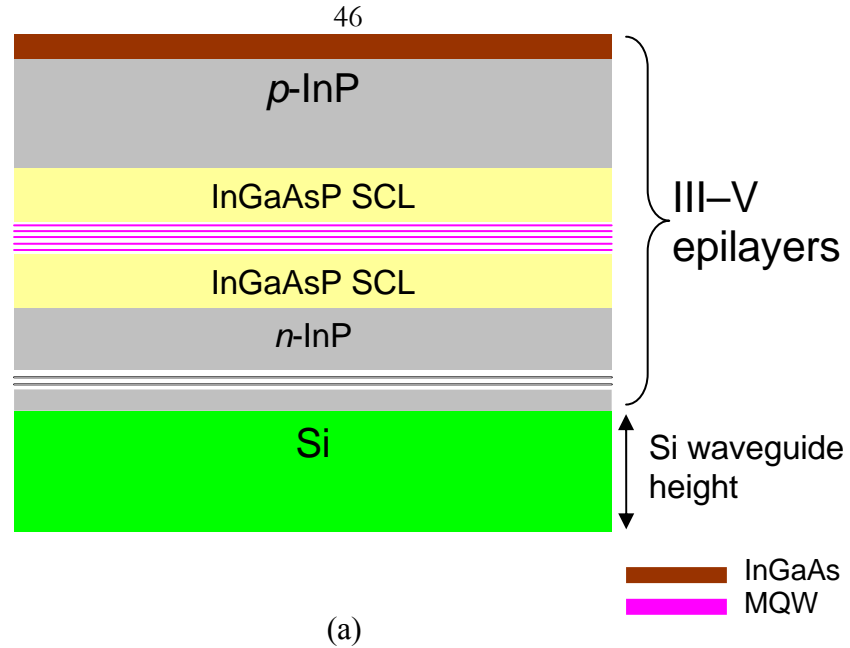


Fig. 4.2. (a) The InGaAsP epilayer bonded to a Si slab waveguide. (b) Confinement factor for Si waveguide of the slab waveguide structure shown in (a). This is the maximal fraction of modal power in Si if the Si slab is replaced with a channel waveguide.

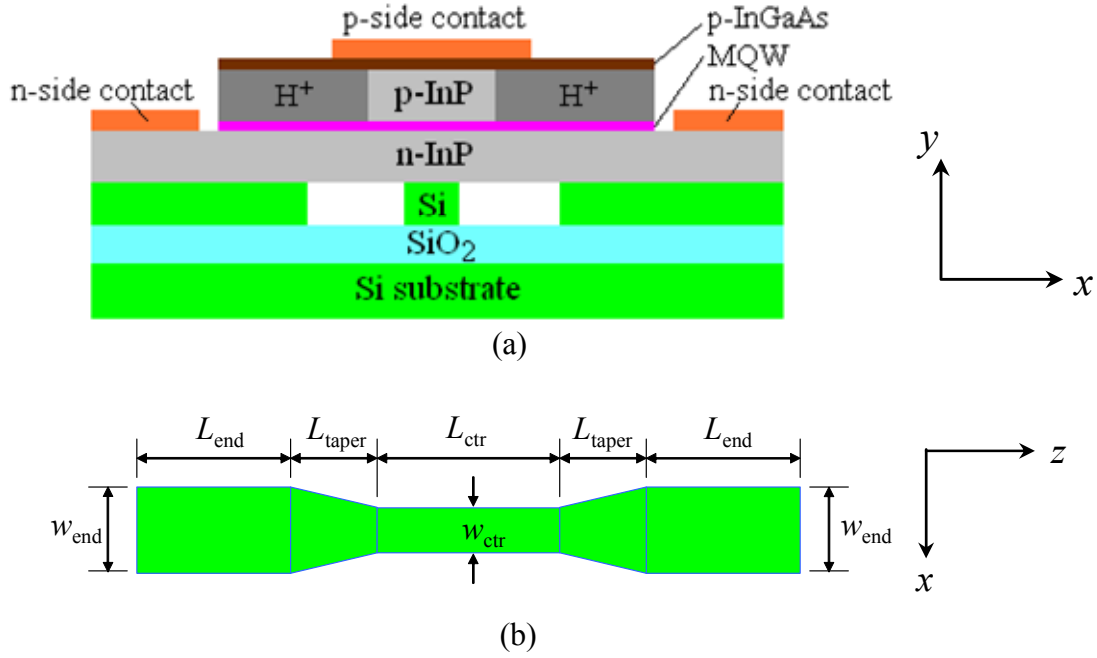


Fig. 4.3. (a) Illustration of the cross-sectional view of the hybrid laser (not to scale). (b) Si waveguide dimensions of the supermode lasers: $L_{\text{end}} = 350 \mu\text{m}$, $L_{\text{taper}} = 200 \mu\text{m}$, $L_{\text{ctr}} = 400 \mu\text{m}$, $w_{\text{end}} = 1.2 \mu\text{m}$, $w_{\text{ctr}} = 0.6, 0.7, 0.8, \text{ or } 0.9 \mu\text{m}$. The tapers connecting the end and central sections have linear width variation.

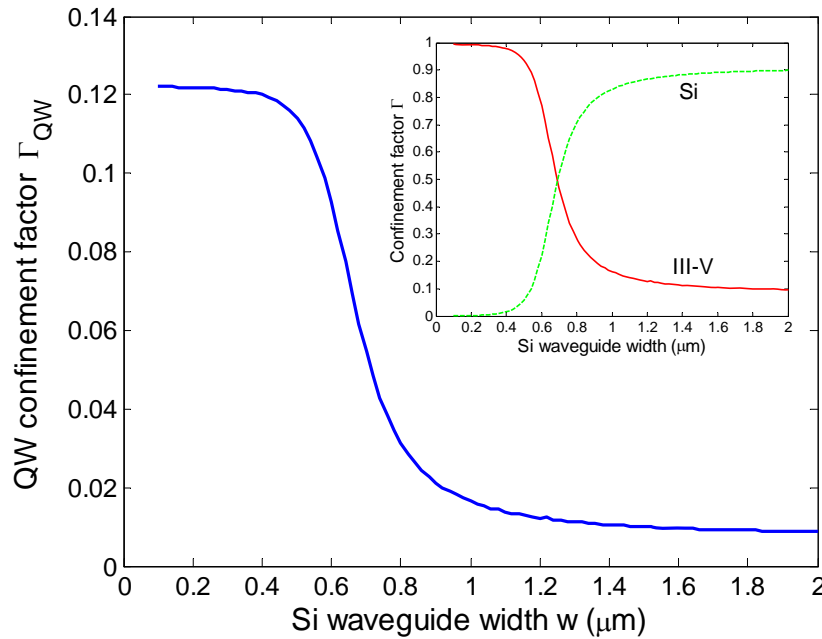


Fig. 4.4. Quantum well confinement factor Γ_{QW} as a function of the Si waveguide width w . Inset: Calculated confinement factors of the III-V and the Si waveguide.

Designing the Si Waveguide for Supermode Control

Now we will understand from the supermode theory that changing the effective index of the Si waveguide by altering its width changes the spatial distribution of the supermodes of the Si/III–V waveguide system (Fig. 2.4). By proper choice of the Si waveguide width, it is possible to localize the supermode mostly in the III–V waveguide or mostly in the Si waveguide. The supermode lasers are designed such that the modal power is localized in the Si waveguide near the ends for output coupling and in the active III–V waveguide in the central portion to obtain maximal gain. The efficient mode transformation between the two states is realized by the shortest possible adiabatic tapers as discussed in Chapter 3. Therefore, the designed Si waveguide has a fixed height of $0.9\ \mu\text{m}$, while exhibiting a dumbbell shape [looking from top as shown in Fig. 4.3(b)] that comprises a central region of width w_{ctr} , two end regions of width w_{end} , and two tapered connecting regions of length L_{taper} .

Based on the InGaAsP epiwafer layer structure (Table 4.1) and given dimensions of the SOI waveguide (fixed Si waveguide height and varying Si waveguide width), the cross-sectional supermode field profile $E(x, y)$ of the hybrid laser was numerically obtained. The modal confinement factor Γ_j defined as [53]

$$\Gamma_j = \frac{\iint_j E^*(x, y)E(x, y)dxdy}{\iint_{\infty} E^*(x, y)E(x, y)dxdy} \quad (4.1)$$

is also referred to as the fraction of modal power confined to region j . The quantum well confinement factor Γ_{QW} was calculated as a function of the Si waveguide width w and the results are plotted in Fig. 4.4. At the phase-matching point the modal power should be

distributed evenly between the III–V and Si waveguides. As shown in the inset of Fig. 4.4, the curves of $\Gamma_{\text{III-V}}$ and Γ_{Si} intersect at $w_0 = 0.69 \text{ } \mu\text{m}$, indicating the phase-matching condition is met there. The laser threshold condition is given by equating the modal gain to the modal loss [54]:

$$\gamma_{\text{th}} \Gamma_{\text{QW}} = \alpha_{\text{III-V}} \Gamma_{\text{III-V}} + \alpha_{\text{Si}} \Gamma_{\text{Si}} + \alpha_s + L^{-1} \ln R^{-1}, \quad (4.2)$$

where γ_{th} denotes the threshold gain, $\alpha_{\text{III-V}}$ and α_{Si} denote respectively the absorption loss in the III–V and the Si waveguide, and α_s represents the scattering loss. $L^{-1} \ln R^{-1}$ is well understood to be the mirror loss for Fabry–Pérot lasers with L the cavity length and R the field reflectivity of the end facets. Varying in the longitudinal (z) direction, all the confinement factors in Eq. (4.2) must be replaced with their effective values that are averaged along the laser cavity $\Gamma_j^{\text{eff}} \equiv L^{-1} \int_0^L \Gamma_j(z) dz$. Therefore, we can keep a high output coupling while taking advantage of the maximal available gain by increasing the $\Gamma_{\text{QW}}^{\text{eff}}$ using the longitudinal modal control.

Several rules must be followed when designing the Si waveguide width: (1) a large w_{end} should be chosen to ensure large Γ_{Si} for output coupling; (2) a small w_{ctr} should be chosen to ensure large Γ_{QW} to obtain high optical gain; however, (3) w_{ctr} should be large enough to ensure mechanical stability of the Si waveguide; and (4) w_{ctr} and w_{end} should be as close as necessary to minimize the additional modal loss arising from the tapering. Designed with these principles and the results in Fig. 4.4, the fabricated supermode lasers have the Si waveguide widths of $w_{\text{end}} = 1.2 \text{ } \mu\text{m}$ and $w_{\text{ctr}} = 0.6, 0.7, 0.8, \text{ or } 0.9 \text{ } \mu\text{m}$. For demonstration of concept, the tapers are simply designed to be linear in width variation.

The lengths associated with the cavity are $L_{\text{end}} = 350 \text{ } \mu\text{m}$, $L_{\text{taper}} = 200 \text{ } \mu\text{m}$, and $L_{\text{ctr}} = 400 \text{ } \mu\text{m}$ for a total device length of $1500 \text{ } \mu\text{m}$. As a control, the evanescent lasers with a constant Si waveguide width of $1.2 \text{ } \mu\text{m}$ and the same total length of $1500 \text{ } \mu\text{m}$ were also fabricated. The calculated effective quantum well (QW) confinement factors $\Gamma_{\text{QW}}^{\text{eff}}$ for these supermode and evanescent lasers are listed in Table 5.1. As can be seen, all the supermode lasers possess considerably higher modal gain than the evanescent laser due to the higher $\Gamma_{\text{QW}}^{\text{eff}}$ in the laser cavity. For example, the supermode laser with $w_{\text{ctr}} = 0.6 \text{ } \mu\text{m}$ and $w_{\text{end}} = 1.2 \text{ } \mu\text{m}$ has its modal gain enhanced by a factor of 3.15 compared to the evanescent laser with a constant Si waveguide width of $1.2 \text{ } \mu\text{m}$.

4.2 Device Fabrication

The fabrication of the hybrid Si/III–V lasers involves multiple processes mainly consisting of SOI waveguides fabrication, InGaAsP epilayer transfer by wafer bonding, InGaAsP mesa formation, current channel definition, and electrode deposition. A detailed fabrication flow chart can be found in Fig. 4.5.

SOI Waveguides Fabrication

Due to the small critical dimensions and the required sidewall quality, the Si waveguides are fabricated by using electron-beam lithography and plasma reactive ion etching. The layout of the Si waveguides is programmed and generated by L-Edit. The layout is then transferred to the e-beam resist ZEP with the exposure of 100 keV electron beam. After the exposure and development, the remaining patterned ZEP serves as the mask for the

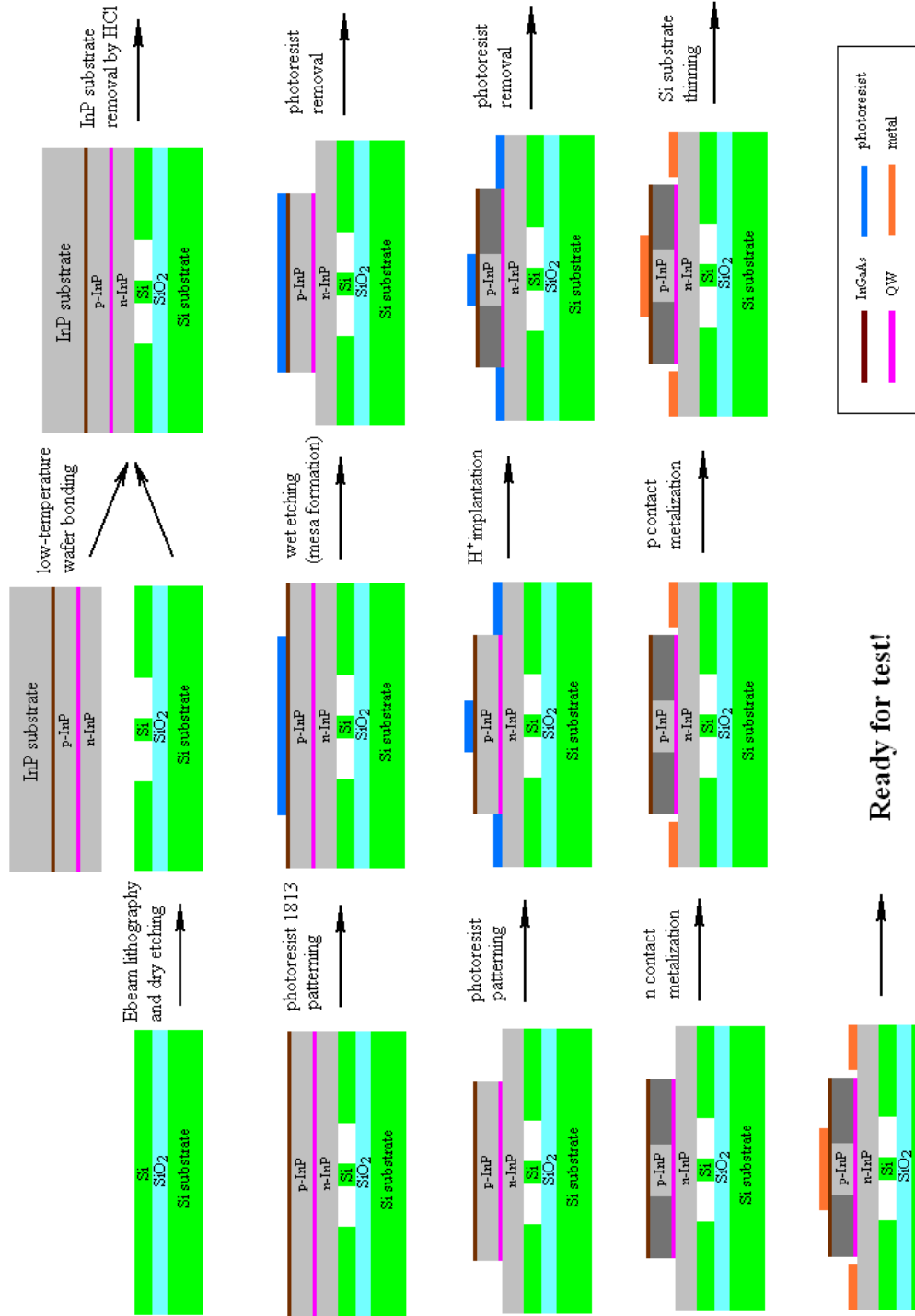


Fig. 4.5. Fabrication flow chart of supermode hybrid Si/III-V lasers.

subsequent $\text{SF}_6/\text{C}_4\text{F}_8$ plasma reactive ion etching, during which the Si to the two sides of the waveguide is entirely etched down to the SiO_2 layer. For more details on the plasma reactive ion etching mechanism and recipes, see [55].

Wafer Bonding and InGaAsP Epilayer Transfer

The next step is to transfer the InGaAsP epilayer from its InP substrate to the patterned SOI wafer. This is achieved by an oxygen plasma-assisted low-temperature wafer bonding process and the subsequent InP substrate removal.

After etching, the SOI wafer is cleaned by organic solvents and then a 3:1 $\text{H}_2\text{SO}_4:\text{H}_2\text{O}_2$ mixture (10 min at 170 °C). In terms of chemical composition, the InGaAsP epifilm as shown in Table 4.1 consists of an InGaAs contact layer at the top, a p -InP upper cladding layer at middle followed by an InGaAsP active layer and then an n -InP lower cladding layer at the bottom. The total thickness of this epifilm is $\sim 2\text{ }\mu\text{m}$.

The wafer bonding procedure begins with solvent cleaning of the surfaces of both the SOI wafer and the InGaAsP epiwafer. A 10-nm-thick oxide layer is grown on top of the SOI wafer to enhance the bonding strength. The surfaces of the two wafers are then activated through exposure to oxygen plasma, and bonded together under a pressure of 0.1 MPa at 150 °C for 2 h. Following the bonding process, the InP substrate is removed by HCl wet etching.

Figure 4.6 clearly shows the cross-sectional structure consisting of the remaining InGaAsP epifilm bonded onto the SOI wafer. The bonding interface between the epifilm and Si is thin and smooth. Figure 4.6(a) focuses on one end of the epifilm: it is evident

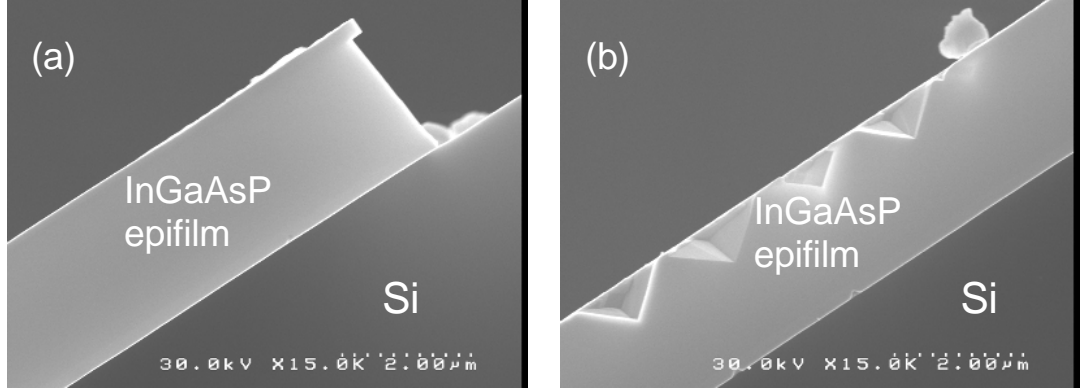


Fig. 4.6. SEM cross-sectional images of the InGaAsP epilayer on SOI by wafer bonding after the InP substrate removal. The InGaAsP epilayer consists of an InGaAs contact layer at the top, a p -InP upper cladding layer at middle followed by an InGaAsP active layer and then an n -InP lower cladding layer at the bottom. (a) Zoom at one end of the epilayer. The top InGaAs layer is protrusive at the end due to its different composition from the p -InP layer below. (b) Zoom at middle of the epilayer. The pyramids at the top of p -InP layer are results of HCl wet etching during InP substrate removal due to the damaged outer InGaAs layer.

that the top InGaAs layer is protrusive at the end due to its different composition from the p -InP layer below. Figure 4.6(b) focuses on a middle part of the epilayer. The pyramids at the top of p -InP layer are results of HCl wet etching during InP substrate removal due to the damaged outer InGaAs layer.

Subsequent Processing of the Bonded InGaAsP Epilayer

With the active III–V epilayer bonded on the SOI wafer, the subsequent processing is in the InGaAsP compound. An 80- μm -wide mesa structure is formed in the InGaAsP layers, centered above the Si waveguide, through photolithography and subsequent three-phase wet etching, down to the n -InP contact layer (see the structure in Table 4.1). The etching

solutions are (a) 1:1:10 mixture of $\text{H}_2\text{SO}_4\text{:H}_2\text{O}_2\text{:H}_2\text{O}$ ($p\text{-InGaAs}$ layer, 60 s), (b) 2:1 mixture of $\text{HCl:H}_2\text{O}$ ($p\text{-InP}$ layer, 30 s), and (c) 1:1:10 mixture of $\text{H}_2\text{SO}_4\text{:H}_2\text{O}_2\text{:H}_2\text{O}$ (quaternary layers, 4 min). After the mesa formation, a 5- μm -wide center current channel by means of proton (H^+) implantation on its two sides is created to enable efficient current injection [56]. The implantation dosage and proton energy are $5 \times 10^{14} \text{ cm}^{-2}$ and 170 keV, respectively. Metal contacts are then deposited by thermal evaporation for the p -side ($\text{Cr/AuZn/Au} = 3.6/7.5/180 \text{ nm}$) on top of the remaining $p\text{-InGaAs}$ layer, and for the n -side ($\text{Cr/AuGe/Au} = 3.6/7.5/180 \text{ nm}$) on the exposed $n\text{-InP}$ layer to the two sides of the mesa. In a working device, the injected current starts from the top p -side contact, passes through the center current channel in the $p\text{-InP}$ cladding and the InGaAsP active region, then bifurcates in the $n\text{-InP}$ layer until it reaches the n -side contacts on both sides.

Device Completion

Finally, the Si substrate is lapped down to a thickness of $\sim 50 \mu\text{m}$ for cleaving facets. Rapid thermal annealing for metal contacts using the setup shown in Fig. 4.7 is usually performed to achieve continuous-wave (CW) devices. The annealed devices are usually die-bonded onto a C-mount, which can be mounted on a temperature controlled stage for testing.

Figure 4.8 shows a top view optical microscope image and cross-sectional SEM images of a fabricated device.

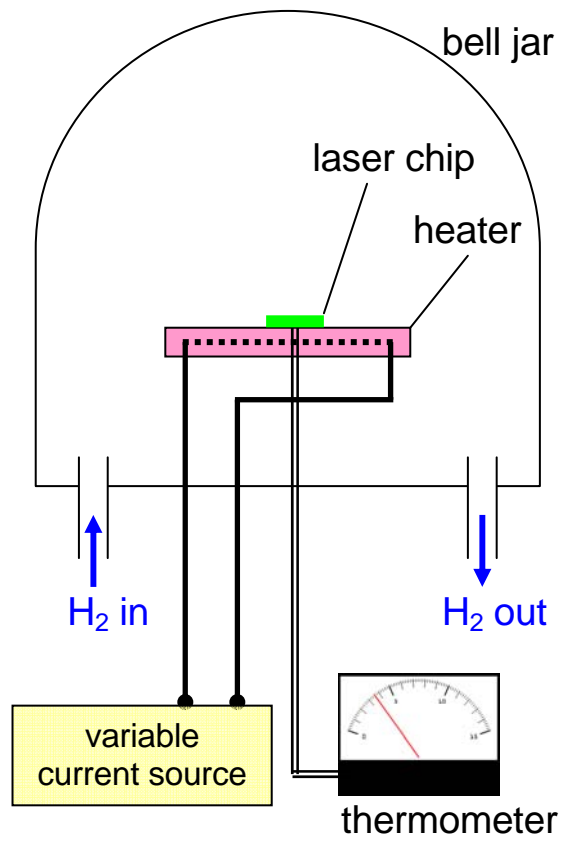
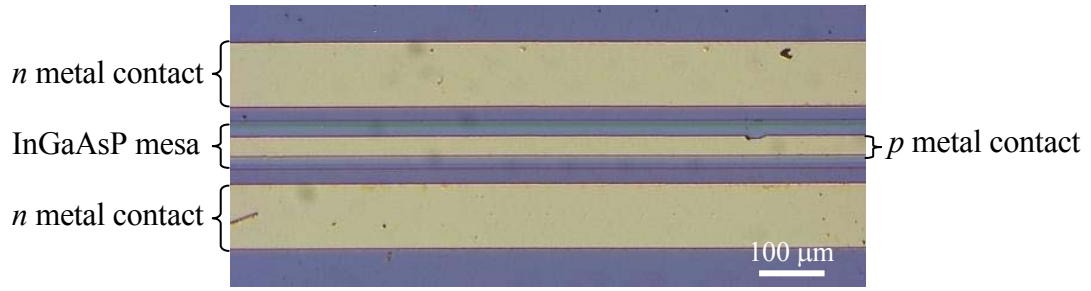
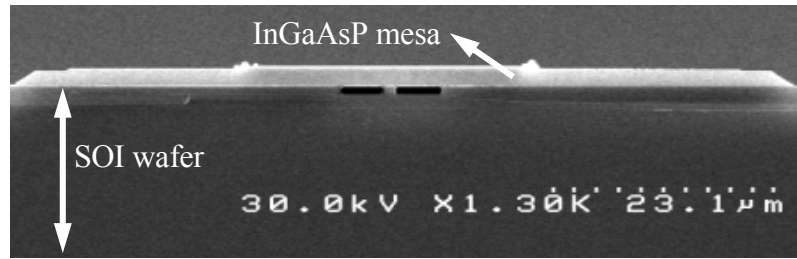


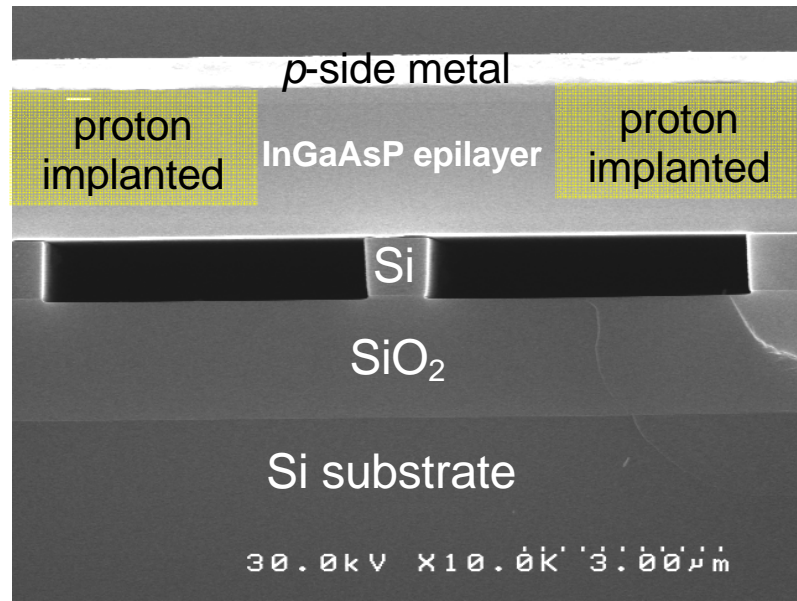
Fig. 4.7. Annealing system for fabricating continuous-wave (CW) semiconductor lasers.



(a)



(b)



(c)

Fig. 4.8. (a) Optical microscope image of top view of a fabricated device. (b), (c) SEM images of a cleaved end facet of a fabricated supermode Si/InGaAsP laser: (b) overview of the device, (c) close-up view at the center Si waveguide region. Approximate proton implanted regions are superimposed on the image for illustration.

Chapter 5

Experimental Characterization and Data Analysis

This chapter is reproduced and adapted with permission from [49, 50, 57], © 2009, 2010 OSA, © 2009 American Vacuum Society.

5.1 Characterization with Pulsed Current Injection

Comparison of Thresholds and Slope Efficiencies

The threshold and slope efficiency were obtained from the $L-I$ curve, which was taken with the setup shown in Fig. 5.1(a). The total emitted power from the laser was collected by an integrating sphere power head, which was connected to a power meter to get the reading. The fabricated laser devices were tested at room temperature under pulsed current injection of 1% duty cycle. The data reported in Table 5.1 were collected from the best device out of many of the same design in order to minimize the impact of unpredictable and uncontrollable fabrication imperfections, which can arbitrarily degrade device performance. As the supermode and evanescent lasers were fabricated and tested on the same platform, direct comparison of results is meaningful. The supermode lasers

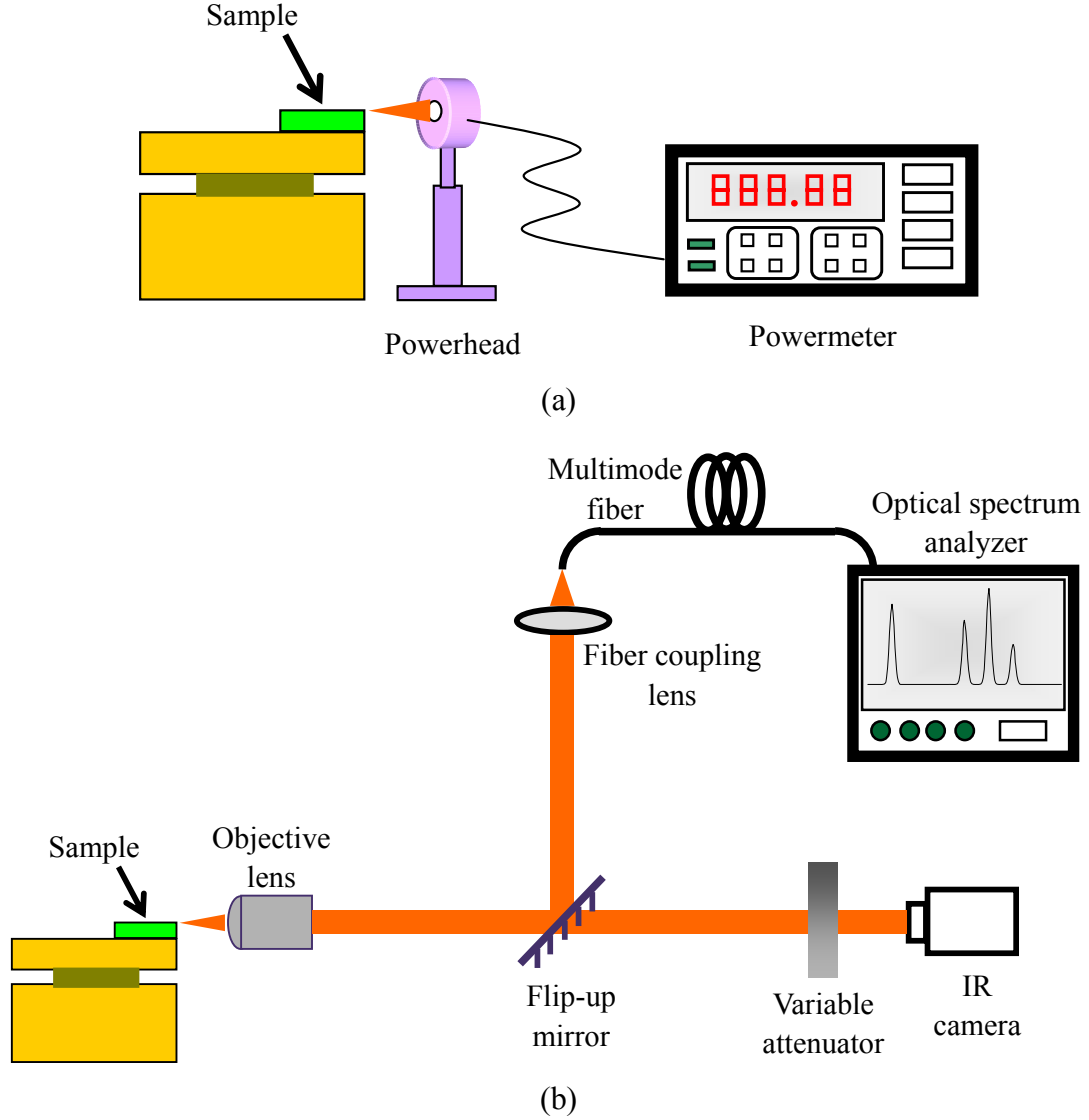


Fig. 5.1. Experimental setup for measuring (a) laser $L-I$ curve, and (b) near-field emission pattern and optical spectrum.

have substantially lower thresholds (in voltage V_{th} or in current density J_{th}) and higher slope efficiencies (η_{ex}) than the evanescent laser.

The threshold behavior of the hybrid lasers is expected: a higher Γ_{QW}^{eff} leads to a lower threshold current density and voltage, which is in agreement with what the

Table 5.1. Test results of supermode (varying-width) lasers and evanescent (constant-width) lasers

Si waveguide type	w_{end} (μm)	w_{ctr} (μm)	$\Gamma_{\text{QW}}^{\text{eff}}$	V_{th} (V)	J_{th} (kA cm^{-2})	η_{ex} (%)
Varying-width	1.2	0.6	0.0388	3.0	1.47	1.06
Varying-width	1.2	0.7	0.0264	4.0	2.20	1.88
Varying-width	1.2	0.8	0.0189	5.0	3.85	2.31
Varying-width	1.2	0.9	0.0155	9.0	11.7	1.50
Constant-width	1.2	1.2	0.0123	11.0	11.9	0.36

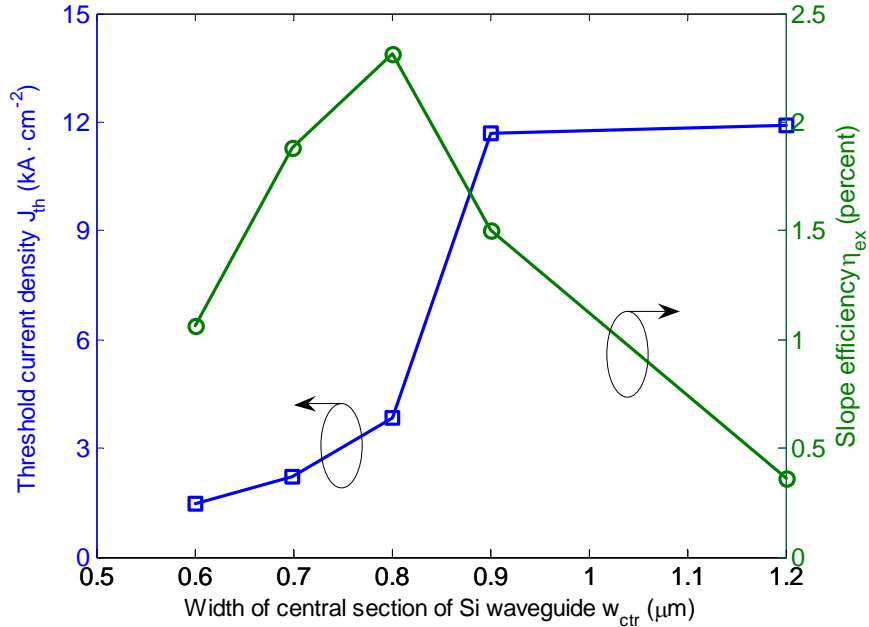


Fig. 5.2. Threshold current density J_{th} and slope efficiency η_{ex} as a function of the width of central section of the Si waveguide w_{ctr} . The threshold current density increases monotonically as w_{ctr} , but the slope efficiency presents a local maximum at $w_{\text{ctr}} = 0.8 \mu\text{m}$.

threshold condition Eq. (4.2) predicts. However, the behavior of the slope efficiency η_{ex} is interesting: shown in Fig. 5.2, as w_{ctr} decreases ($1.2 \rightarrow 0.6 \mu\text{m}$) and $\Gamma_{\text{QW}}^{\text{eff}}$ increases, η_{ex} presents a local maximum at $w_{\text{ctr}} = 0.8 \mu\text{m}$. In traditional III–V lasers the threshold and slope efficiency are usually inversely related, meaning a monotonically decreased

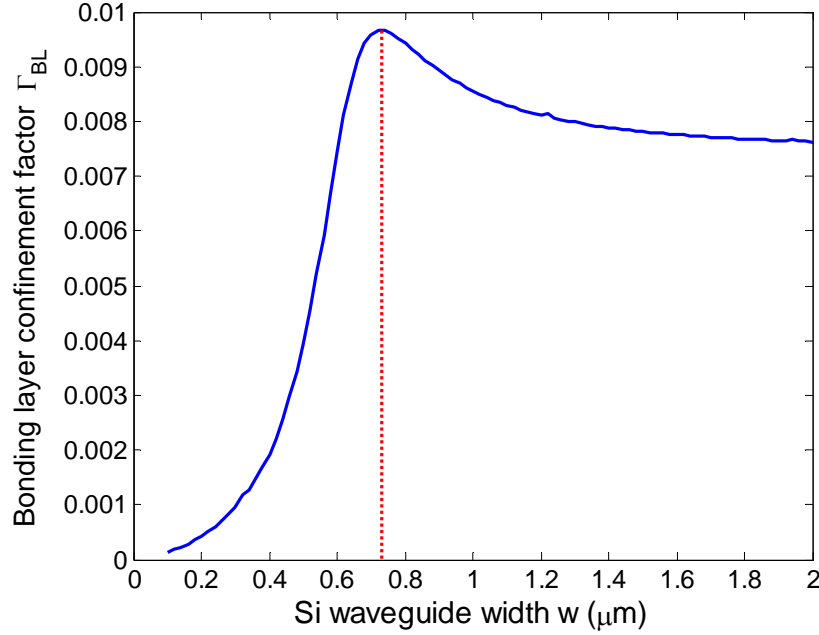


Fig. 5.3. Bonding interfacial layer confinement factor Γ_{BL} as a function of the Si waveguide width w . The maximal confinement to the bonding interfacial layer is achieved at $w = 0.73 \mu\text{m}$.

threshold should be associated with a monotonically increased slope efficiency. The abnormal trend of η_{ex} observed in the hybrid lasers suggests that the end facet loss might not be the only contribution for output coupling. As many interfacial defects were introduced during the wafer bonding step, the coupling from the guided mode to the radiation field should not be neglected, and this scattering loss might provide another source for the laser output. Since this scattering loss obviously depends on the modal confinement to the bonding interfacial layer Γ_{BL} , we calculated its value as a function of the Si waveguide width. As shown in Fig. 5.3, there is indeed a turning with the maximum achieved at $w = 0.73 \mu\text{m}$. This well explains the turning of η_{ex} happening probably at somewhere between $w_{\text{ctr}} = 0.7$ and $0.8 \mu\text{m}$.

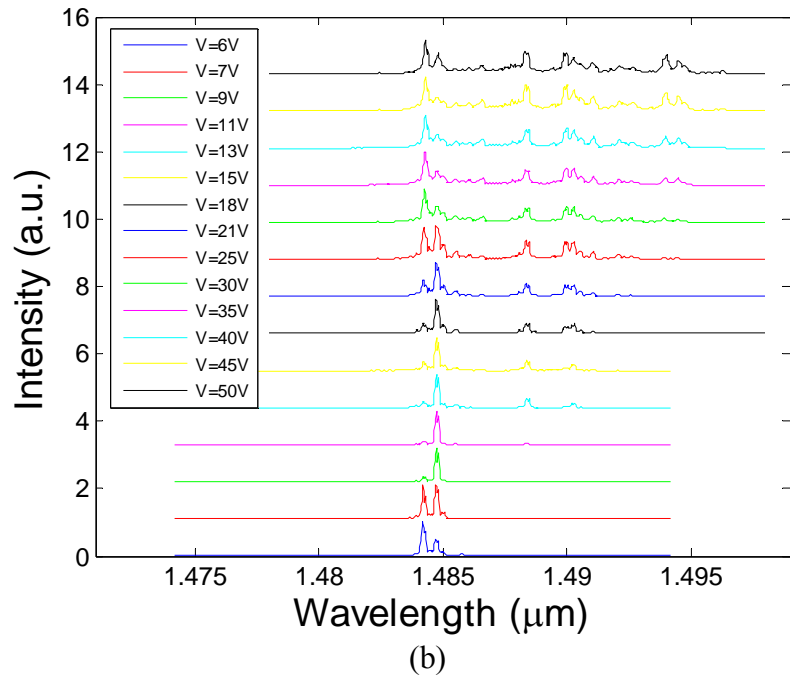
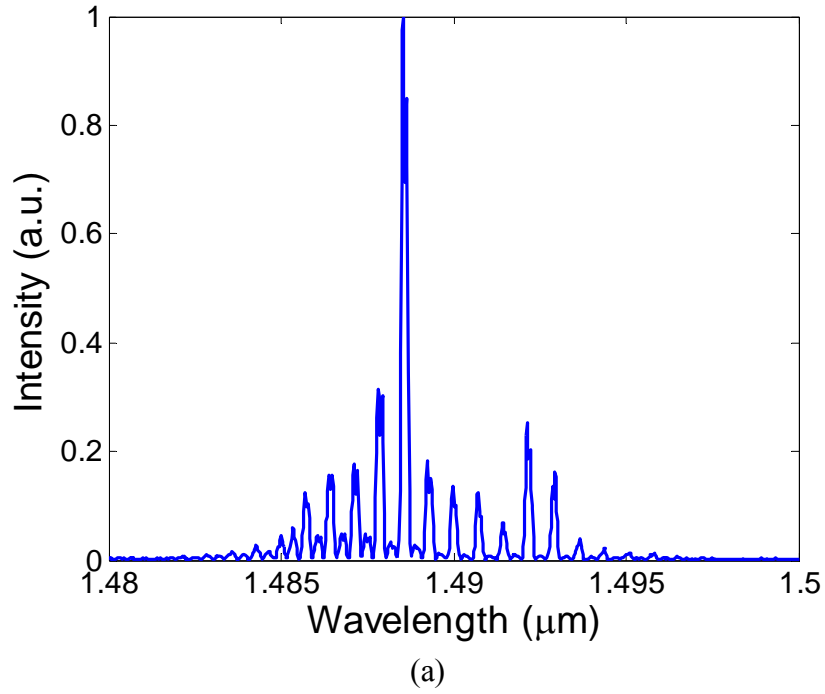


Fig. 5.4. (a) Optical spectrum of a typical device. (b) Evolution of the optical spectrum as the pump current (voltage) increases. Higher pump level results in the expansion of the range of lasing modes to the longer wavelength side. Spectra in both (a) and (b) were measured with pulsed current injection.

Laser Emission Spectra

Shown in Fig. 5.1(b), the laser emission was coupled via multimode fiber to an optical spectrum analyzer to obtain the laser spectrum. Figure 5.4(a) shows the optical spectrum of a laser device. The equidistant multiple peaks are the typical feature of a Fabry–Pérot laser. The separation between the adjacent peaks in the spectrum is the free spectrum range of the Fabry–Pérot cavity. Figure 5.4(b) displays the evolution of the optical spectrum as the pump current (voltage) increases. Higher pump level results in the expansion of the range of lasing modes to the longer wavelength side. This is because the gain spectrum broadens to the longer wavelength side so that those modes can lase once their modal losses are compensated by gain.

Near-Field Emission Patterns

Using the same setup shown in Fig. 5.1(b), the laser near-field emission patterns were obtained by focusing the laser emission to an IR camera with a typical lens imaging system. We can see the mode is mostly confined to the lower Si waveguide at the end facet. As the pump current increases, the mode tends to concentrate more in the Si waveguide, which is potentially good for outcoupling to other devices in a photonic circuit. These images provide a striking illustration to the confinement of the lasing mode in the Si waveguide.

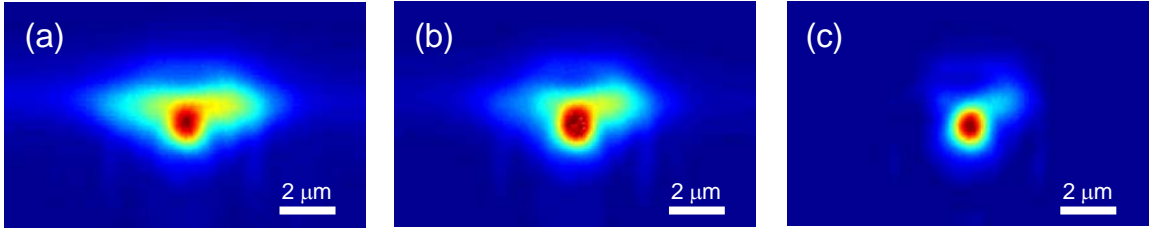


Fig. 5.5. Near-field patterns of the edge emission from a device operated (a) below threshold, (b) at threshold, and (c) above threshold. The modal confinement to the Si waveguide (especially when the mode is lasing) is obvious.

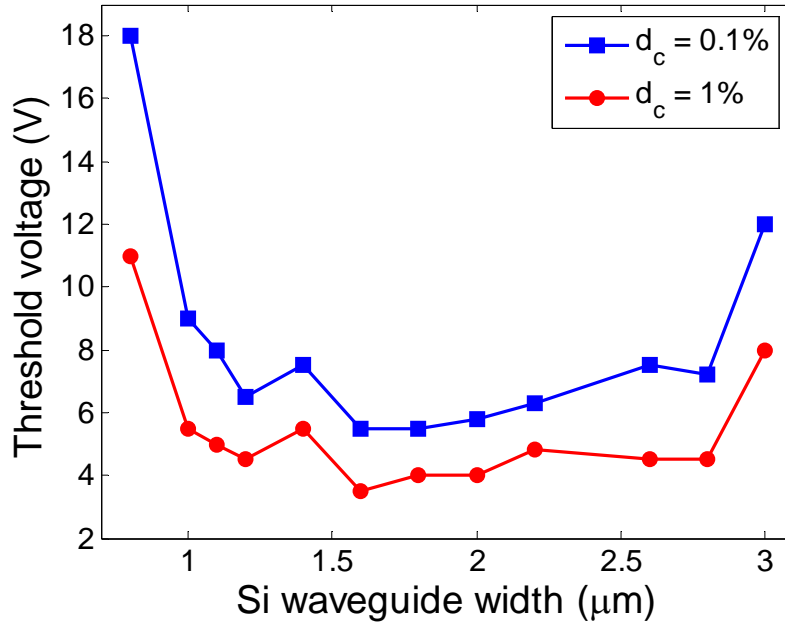


Fig. 5.6. Threshold voltage of evanescent Si/InGaAsP lasers with constant Si waveguide widths. Measurements were taken in pulsed mode at 15 °C, with d_c denoting the duty cycle of the applied voltage.

Threshold Dependence on the Si Waveguide Width of Evanescent Devices

On varying the Si waveguide width w , V_{th} was found to have a local minimum at $w \sim 1.5 \mu\text{m}$, with dependence shown in Fig. 5.6. This behavior can be understood qualitatively by considering the two limiting cases of waveguide width. As width decreases, less of the mode resides in the silicon, and thus experiences less feedback from the Si facets, which are of higher reflectivity than those in the III–V. On the other hand, as width increases, the mode is less confined to the quantum well region and thus requires a higher pump level to reach threshold.

5.2 Continuous-Wave Operation

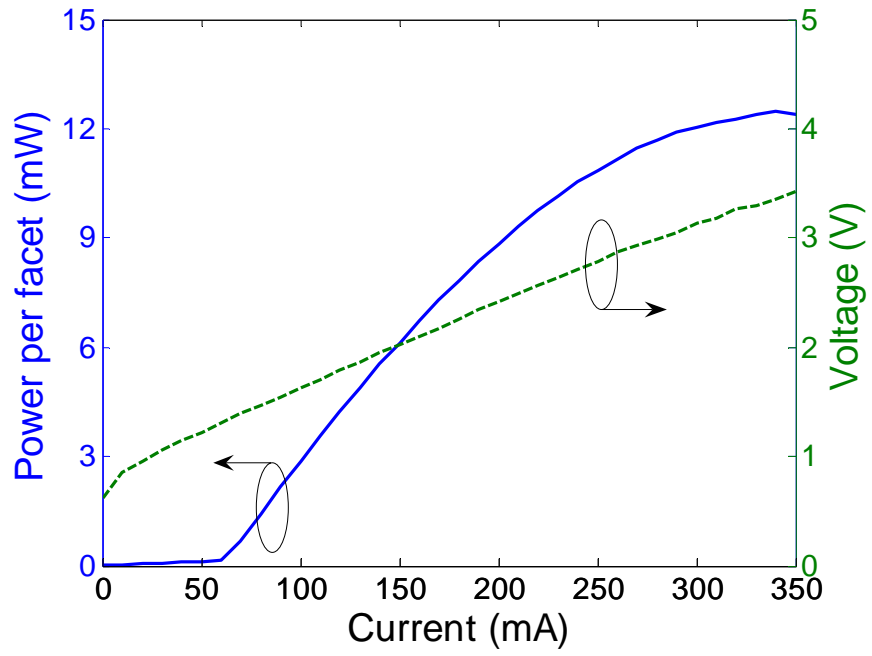
Using the setup shown in Fig. 4.7, the fabricated laser devices were rapidly annealed after cleaving facets. Typical annealing conditions are 400–420 °C for 10–15 s in hydrogen atmosphere. The annealing assists in the diffusion of Zn from the p -side metal contact into the p -side InGaAsP epilayers, and therefore reduces the resistance of that region. After annealing, the device was mounted on a thermoelectric cooler temperature controlled stage for testing.

Figure 5.7(a) shows an L – I – V curve of a 960- μm -long evanescent Si/InGaAsP laser device, with constant Si waveguide width of 1.0 μm , measured at 15 °C. The turn-on voltage was 0.8 V, and the lasing threshold voltage V_{th} was 1.3 V. The threshold current I_{th} was 60 mA, corresponding to a threshold current density J_{th} of 1.25 kA cm^{-2} . The maximum power output P_{max} from a single facet was 12.5 mW, and the external slope efficiency η_{ex} for a single facet was 8.4%. The series resistance of the laser was 8 Ω .

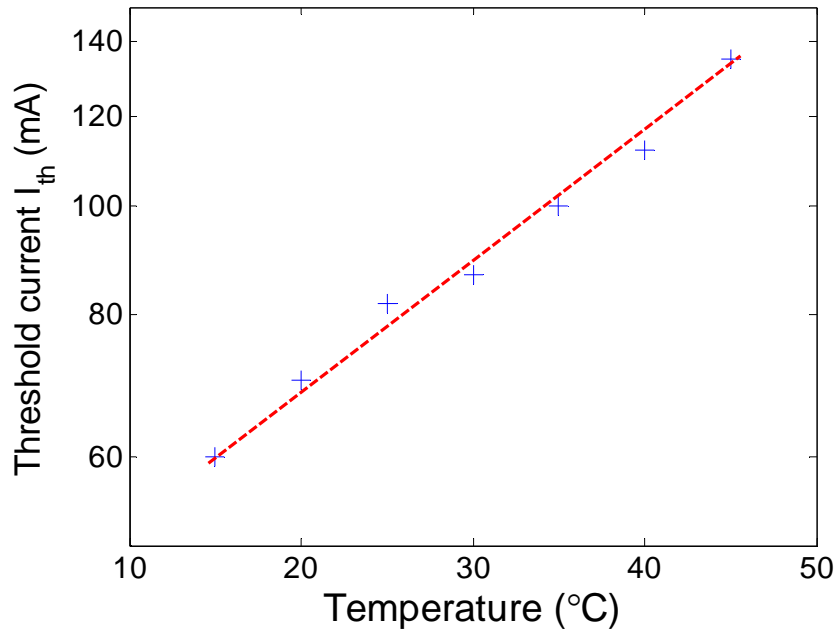
Figure 5.7(b) shows I_{th} as a function of temperature. Continuous-wave lasing could be obtained at temperatures up to 45 °C, and the characteristic temperature of the device was found to be 39 °K.

Figure 5.8(a) shows the laser spectrum of the device, whose central wavelength was 1490 nm. The modal loss α was estimated as 50–60 cm^{-1} and the internal quantum efficiency was bound above 0.83, using the Hakki–Paoli method [58] and the measured η_{ex} . Figure 5.8(b) plots evolution of the optical spectrum with the increased pump current: the emission lines shift to longer wavelength side while the envelope broadens. This is because of broadening and redshift of the gain spectrum of the quantum wells under higher pumping levels.

Evanescent lasers with various cavity lengths ranging between 300 and 1500 μm were also tested, and J_{th} of 1–1.5 kA cm^{-2} were obtained. I_{th} of the 300- μm -long devices was 24 mA at 15 °C, with P_{max} of 4.2 mW. J_{th} and V_{th} of the devices are about 35% lower than those of previously reported Fabry–Pérot hybrid Si/AlGaInAs lasers [20]. At the same time, the devices P_{max} is 70% higher, and their η_{ex} is 30% higher. As one of the key challenges facing hybrid Si/III–V active devices is the extent of heat generation [59], the reduction in threshold current and voltage may prove significant. These improved performances are due to either our different choice of III–V material, or the different fabrication processing.



(a)



(b)

Fig. 5.7. (a) L - I - V curve of a 960- μm -long evanescent laser under CW operation at 15 °C. (b) Lasing threshold current (in log scale) as a function of temperature (blue “+” signs) with a linear fit (red dashed line).

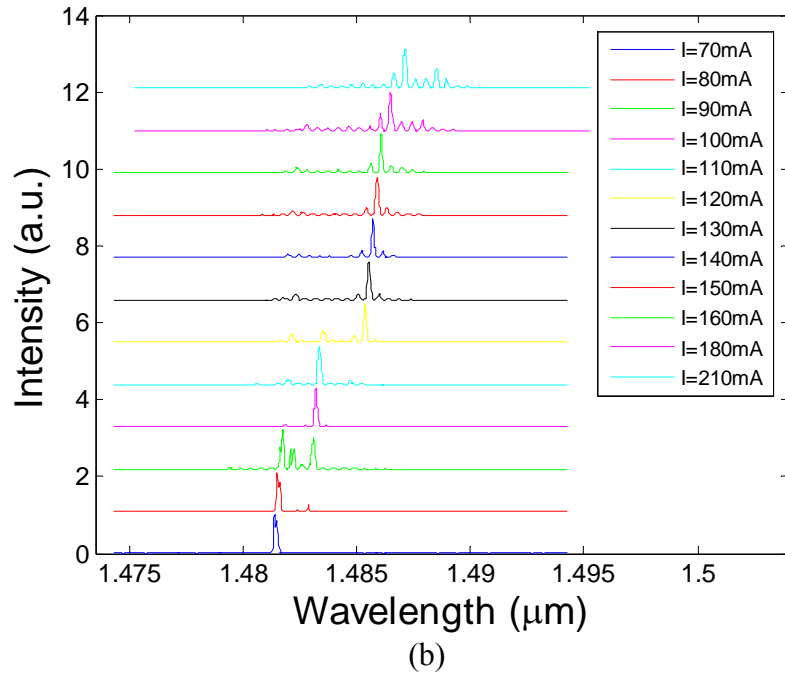
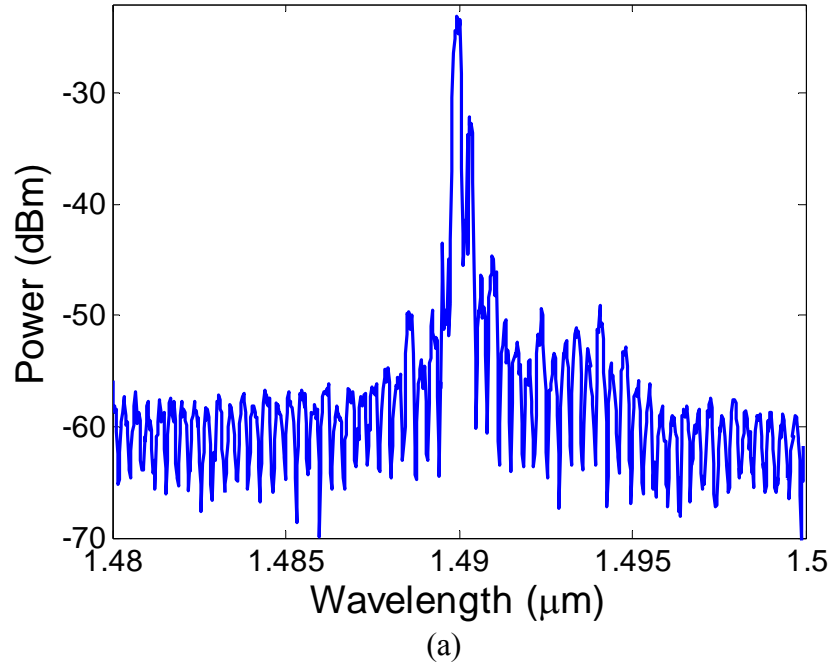


Fig. 5.8. (a) Optical spectrum of a Si/InGaAsP evanescent laser (in dB scale). (b) Evolution of the optical spectrum as the pump current increases. The emission lines shift to longer wavelength side and the envelope broadens with higher pump levels. Spectra in both (a) and (b) were measured with CW current injection.

Chapter 6

Conclusion and Outlook

Hybrid Si/III–V integration by using direct wafer bonding is considered the most promising avenue toward the next-generation high-speed intra- and interchip optical communication. We have proposed, using supermode theory and the adiabaticity theorem, to vary the Si waveguide width along the hybrid Si/III–V circuit so as to control the localization of the mode in the longitudinal direction. Careful design by taking advantage of this supermode control effectively enhances the modal confinement to quantum wells, yielding increased modal gain. We have also experimentally demonstrated the superiority of the supermode Si/InGaAsP hybrid lasers with an adiabatically varying Si waveguide width over the evanescent lasers with a constant Si waveguide width. Fabricated side by side on the same platform, the supermode lasers have substantially lower lasing thresholds and higher slope efficiencies. These advantages translate to lower power consumption and smaller device size in this technology that may hold the key to photonics/electronics integration.

Our process optimization yielded room-temperature, continuous-wave operation of Si/InGaAsP lasers. A 960- μm -long evanescent laser device achieved a maximal single-facet output power as high as 12.7 mW, a single-facet slope efficiency of 8.4%, and a

lasing threshold current density of 1 kA cm^{-2} . Continuous-wave laser operation was obtained up to 45°C . The threshold current density and the threshold voltage of the fabricated devices are 30%–40% lower than those of the corresponding, previously reported Fabry–Pérot laser devices having a similar geometry [20]. At the same time, the output power and differential slope efficiency observed are higher than previously reported. Injection current dependent optical spectra feature the redshift and broadening of the range of emission peaks. Near-field edge-emission patterns show that the output light comes mostly from the Si waveguide, indicating the mode inside the laser cavity is mostly confined to the Si waveguide near the output facet.

It is straightforward that the next step is to extend this “longitudinal supermode control” concept to other types of hybrid photonic devices such as optical amplifiers, modulators, detectors, and finally, integrated circuits with a combination of the individual functional devices, leading to the rise of a large-scale, high-efficiency Si/III–V hybrid circuitry.

Part II

Circular Bragg Lasers: Theory and Design for Large Area, High Power Surface Emission Applications

Chapter 7

Introduction

Surface-emitting lasers have been attracting people's interest over the past two decades because of their salient features such as low threshold current, single-mode operation, and wafer-scale integration [60]. Their low-divergence surface-normal emission also facilitates output coupling and packaging. Although vertical cavity surface emitting lasers (VCSELs) have already been commercially available, their single-modedness and good emission pattern are guaranteed only for devices with a small mode area (diameter of several microns). Attempts of further increase in the emission aperture have failed mostly because of the contradictory requirements of large-area emitting aperture and single modedness, which casts a shadow over the usefulness of VCSELs in high-power applications.

A highly desirable semiconductor laser will consist of a large aperture (say, diameter larger than 20 μm) emitting vertically (i.e., perpendicularly to the plane of the laser). It should possess the high efficiency typical of current-pumped, edge-emitting semiconductor lasers and, crucially, be single-moded. Taking a clue from the traditional edge-emitting distributed-feedback (DFB) semiconductor laser, we proposed employing transverse circular Bragg confinement mechanism to achieve the goals and those lasers are accordingly referred to as "circular Bragg lasers."

There have been intensive research activities in planar circular grating lasers since early 1990s. Erdogan and Hall were the first to analyze their modal behavior with a coupled-mode theory [61, 62]. Wu et al. were the first to experimentally realize such lasers in semiconductors [63, 64]. With a more rigorous theoretical framework, Shams-Zadeh-Amiri et al. analyzed their above-threshold properties and radiation fields [65, 66]. More recently, organic polymers are also used as the gain medium for these lasers due to their low fabrication cost [67-69].

The circular gratings in the above-referenced work are designed radially periodic. In 2003 we proposed using Hankel-phased, i.e., *radially chirped*, gratings to achieve optimal interaction with the optical fields [70], since the eigenmodes of the wave equation in cylindrical coordinates are Hankel functions. With their grating designed to follow the phases of Hankel functions, these circular Bragg lasers usually take three configurations as shown in Fig. 7.1: (a) circular DFB laser, in which the grating extends from the center to the exterior boundary x_b ; (b) disk Bragg laser, in which a center disk is surrounded by a radial Bragg grating extending from x_0 to x_b ; (c) ring Bragg laser, in which an annular defect is surrounded by both inner and outer gratings extending respectively from the center to x_L and from x_R to x_b . Including a second-order Fourier component, the gratings are able to provide in-plane feedback as well as couple laser emission out of the resonator plane in vertical direction.

In the following chapters we will present a comprehensive and systematic study on the surface-emitting Hankel-phased circular Bragg lasers. It is structured in the following manner: In Chapter 8 we derive a comprehensive coupled-mode theory for the Hankel-phased circular grating structure in an active medium. Solving the coupled-mode

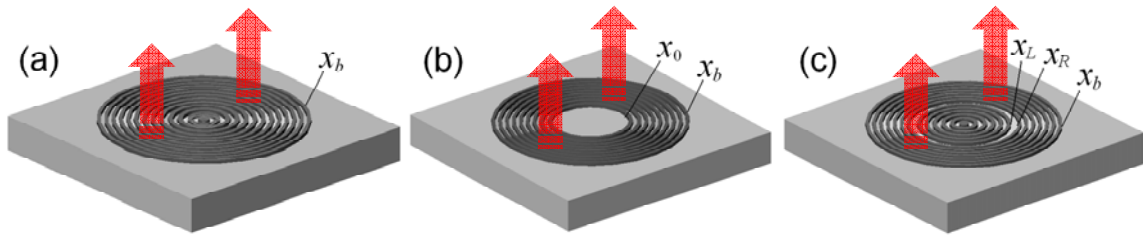


Fig. 7.1. Surface-emitting circular Bragg lasers: (a) circular DFB laser; (b) disk Bragg laser; (c) ring Bragg laser. Laser emission is coupled out of the resonator plane in the vertical direction via the Bragg gratings.

equations with the appropriate boundary conditions for each laser configuration, Chapter 9 focuses on every aspect in obtaining the laser modes: analytical method, numerical method, and mode-solving accuracy check. Chapter 10 gives near-threshold modal properties of the lasers; comparison of different types of lasers demonstrates the advantages of disk and ring Bragg lasers in high-efficiency surface laser emission. Chapter 11 discusses above-threshold modal behavior, nonuniform pumping effect, and optimal design for different types of lasers. Chapter 12 concludes Part II of the thesis and suggests directions for future research.

Chapter 8

Comprehensive Coupled-Mode Theory

This chapter is reproduced and adapted with permission from [71, 72], © 2007 IEEE, © 2008 SPIE.

8.1 Derivation of Comprehensive Coupled-Mode Theory for Circular Grating Structure in an Active Medium

We can start from the scalar Helmholtz equation for the z component of electric field in cylindrical coordinates,

$$\left[\frac{1}{\rho} \frac{\partial}{\partial \rho} \left(\rho \frac{\partial}{\partial \rho} \right) + \frac{1}{\rho^2} \frac{\partial^2}{\partial \varphi^2} + k_0^2 n^2(\rho, z) + \frac{\partial^2}{\partial z^2} \right] E_z(\rho, \varphi, z) = 0, \quad (8.1)$$

where ρ , φ , and z are respectively radial, azimuthal, and vertical coordinates, $k_0 = \omega/c = 2\pi/\lambda_0$ is the wave number in vacuum.

For an azimuthally propagating eigenmode, E_z in a passive uniform medium in which the dielectric constant $n^2(\rho, z) = \varepsilon_r(z)$ can be expressed as

$$E_z(\rho, \varphi, z) = E_z^{(m)}(\rho, z) \exp(im\varphi) = \left[AH_m^{(1)}(\beta\rho) + BH_m^{(2)}(\beta\rho) \right] Z(z) \exp(im\varphi), \quad (8.2)$$

with m the azimuthal mode number, $\beta = k_0 n_{\text{eff}}$ the in-plane propagation constant, and $Z(z)$ the fundamental mode profile of the planar slab waveguide satisfying

$$\left(k_0^2 \varepsilon_r(z) + \frac{\partial^2}{\partial z^2} \right) Z(z) = \beta^2 Z(z). \quad (8.3)$$

In a radially perturbed gain medium, the dielectric constant can be expressed as $n^2(\rho, z) = \varepsilon_r(z) + i\varepsilon_i(z) + \Delta\varepsilon(\rho, z)$ where $\varepsilon_i(z)$ with $|\varepsilon_i(z)| \ll \varepsilon_r(z)$ represents the medium gain or loss and $\Delta\varepsilon(\rho, z)$ is the perturbation profile that in a cylindrical geometry can be expanded in Hankel-phased plane wave series:

$$\begin{aligned} \Delta\varepsilon(\rho, z) &= -\Delta\varepsilon_0 \sum_{l=\pm 1, \pm 2} a_l(z) \exp\left(-il\Phi[H_m^{(1)}(\beta_{\text{design}}\rho)]\right) \\ &= -\Delta\varepsilon_0 \sum_{l=\pm 1, \pm 2} a_l(z) \exp\left(-il\Phi[H_m^{(1)}(x)]\right) \exp(-il\delta \cdot x) \\ &= -\Delta\varepsilon_0 \left[a_2(z) \frac{H_m^{(2)}}{H_m^{(1)}} e^{-2i\delta \cdot x} + a_{-2}(z) \frac{H_m^{(1)}}{H_m^{(2)}} e^{2i\delta \cdot x} + a_1(z) \frac{H_m^{(2)}}{|H_m^{(1)}|} e^{-i\delta \cdot x} + a_{-1}(z) \frac{H_m^{(1)}}{|H_m^{(1)}|} e^{i\delta \cdot x} \right]. \end{aligned} \quad (8.4)$$

In the above expression, $a_l(z)$ is the l th-order expansion coefficient of $\Delta\varepsilon(\rho, z)$ at a given z . x is the normalized radial coordinate defined as $x = \beta\rho$. $\delta = (\beta_{\text{design}} - \beta)/\beta$ ($|\delta| \ll 1$), the normalized frequency detuning factor, represents a relative frequency shift of a resonant mode from the designed value.

To account for the vertical radiation, an additional term $\Delta E(x, z)$ is introduced into the modal field so that

$$E_z^{(m)}(x, z) = \left[A(x) H_m^{(1)}(x) + B(x) H_m^{(2)}(x) \right] Z(z) + \Delta E(x, z). \quad (8.5)$$

Assuming that the radiation field $\Delta E(x, z)$ has an $\exp(\pm ik_0 z)$ dependence on z in free space, i.e.,

$$\left[\frac{1}{\rho} \frac{\partial}{\partial \rho} \left(\rho \frac{\partial}{\partial \rho} \right) - \frac{m^2}{\rho^2} \right] \Delta E = 0, \quad (8.6)$$

substituting Eqs. (8.4), (8.5), and (8.6) into Eq. (8.1), introducing the large-radius approximations [70]

$$\left| \frac{H_m^{(1,2)}(x)}{x} \right| \ll \left| \frac{dH_m^{(1,2)}(x)}{dx} \right|, \quad \frac{d^n H_m^{(1,2)}(x)}{dx^n} \approx (\pm i)^n H_m^{(1,2)}(x), \quad (8.7)$$

neglecting the second derivatives of $A(x)$ and $B(x)$, and applying the modal solution in the passive unperturbed case, one obtains

$$\begin{aligned} & 2iZ \left(\frac{dA}{dx} H_m^{(1)} - \frac{dB}{dx} H_m^{(2)} \right) + i \frac{k_0^2 \varepsilon_i}{\beta^2} (AH_m^{(1)} Z + BH_m^{(2)} Z) + \frac{1}{\beta^2} \left(k_0^2 \varepsilon_r + ik_0^2 \varepsilon_i + \frac{\partial^2}{\partial z^2} \right) \Delta E \\ &= \frac{k_0^2 \Delta \varepsilon_0}{\beta^2} \left[a_2 \frac{H_m^{(2)}}{H_m^{(1)}} e^{-2i\delta \cdot x} + a_{-2} \frac{H_m^{(1)}}{H_m^{(2)}} e^{2i\delta \cdot x} + a_1 \frac{H_m^{(2)}}{|H_m^{(1)}|} e^{-i\delta \cdot x} + a_{-1} \frac{H_m^{(1)}}{|H_m^{(1)}|} e^{i\delta \cdot x} \right] \\ & \times (AH_m^{(1)} Z + BH_m^{(2)} Z + \Delta E). \end{aligned} \quad (8.8)$$

The phase-matching condition requires that the source and wave have close phase dependence. Grouping the terms with the same kind of Hankel functions leads to the following set of coupled equations:

$$2i \frac{dA}{dx} H_m^{(1)} Z + i \frac{k_0^2 \varepsilon_i}{\beta^2} AH_m^{(1)} Z = \frac{k_0^2 \Delta \varepsilon_0}{\beta^2} \left(a_{-2} BH_m^{(1)} e^{2i\delta \cdot x} Z + a_{-1} \frac{\Delta E}{|H_m^{(1)}|} H_m^{(1)} e^{i\delta \cdot x} \right), \quad (8.9)$$

$$-2i \frac{dB}{dx} H_m^{(2)} Z + i \frac{k_0^2 \varepsilon_i}{\beta^2} BH_m^{(2)} Z = \frac{k_0^2 \Delta \varepsilon_0}{\beta^2} \left(a_2 AH_m^{(2)} e^{-2i\delta \cdot x} Z + a_1 \frac{\Delta E}{|H_m^{(1)}|} H_m^{(2)} e^{-i\delta \cdot x} \right), \quad (8.10)$$

$$\left(k_0^2 \varepsilon_r + \frac{\partial^2}{\partial z^2}\right) \Delta E = k_0^2 \Delta \varepsilon_0 \left(a_1 A \left|H_m^{(1)}\right| e^{-i\delta \cdot x} Z + a_{-1} B \left|H_m^{(1)}\right| e^{i\delta \cdot x} Z\right). \quad (8.11)$$

From Eq. (8.11), ΔE can be expressed as

$$\Delta E = \left(s_1 A e^{-i\delta \cdot x} + s_{-1} B e^{i\delta \cdot x}\right) \left|H_m^{(1)}\right|, \quad (8.12)$$

where

$$s_l(z) = k_0^2 \Delta \varepsilon_0 \int_{-\infty}^{+\infty} a_l(z') Z(z') G(z, z') dz', \quad (8.13)$$

and $G(z, z')$ is the Green's function satisfying

$$\left(k_0^2 \varepsilon_r(z) + \frac{\partial^2}{\partial z^2}\right) G(z, z') = \delta(z - z'). \quad (8.14)$$

Substituting Eq. (8.12) into Eqs. (8.9) and (8.10), multiplying both sides by $Z(z)$, and integrating over z yields

$$\frac{dA}{dx} = \left(g_A - h_{-1,1}\right) A - \left(h_{-1,-1} + i h_{-2}\right) B e^{2i\delta \cdot x}, \quad (8.15)$$

$$\frac{dB}{dx} = -\left(g_A - h_{1,-1}\right) B + \left(h_{1,1} + i h_2\right) A e^{-2i\delta \cdot x}, \quad (8.16)$$

where the gain coefficient

$$g_A \equiv -\frac{k_0^2}{2P\beta^2} \int_{-\infty}^{+\infty} \varepsilon_i(z) Z^2(z) dz, \quad (8.17)$$

the radiation coupling coefficients

$$h_{\pm 1, \pm 1} \equiv \frac{ik_0^2 \Delta \varepsilon_0}{2P\beta^2} \int_{-\infty}^{+\infty} a_{\pm 1}(z) s_{\pm 1}(z) Z(z) dz, \quad (8.18)$$

the feedback coupling coefficients

$$h_{\pm 2} \equiv \frac{k_0^2 \Delta \varepsilon_0}{2P\beta^2} \int_{-\infty}^{+\infty} a_{\pm 2}(z) Z^2(z) dz, \quad (8.19)$$

and the normalization constant

$$P \equiv \int_{-\infty}^{+\infty} Z^2(z) dz. \quad (8.20)$$

In the case of index grating, we can choose the phase of the grating such that $a_{-1} = a_1$, $a_{-2} = a_2$, then we denote $h_1 = h_{\pm 1, \pm 1}$, $h_2 = h_{\pm 2}$. By defining $u = g_A - h_1$ and $v = h_1 + ih_2$, Eqs. (8.15) and (8.16) become

$$\frac{dA(x)}{dx} = u(x) \cdot A(x) - v(x) \cdot B(x) \cdot e^{2i\delta \cdot x}, \quad (8.21)$$

$$\frac{dB(x)}{dx} = -u(x) \cdot B(x) + v(x) \cdot A(x) \cdot e^{-2i\delta \cdot x}. \quad (8.22)$$

Specifically, in the unperturbed (i.e., no-grating) region where $\Delta \varepsilon = 0$, h_1 and h_2 vanish, and Eqs. (8.21) and (8.22) reduce to

$$\frac{dA(x)}{dx} = g_A(x) \cdot A(x), \quad (8.23)$$

$$\frac{dB(x)}{dx} = -g_A(x) \cdot B(x). \quad (8.24)$$

8.2 Grating Design Procedure and Calculations of the Numerical Green's Function $G(z, z')$, Coefficients h_1 , h_2 , and s_1

Since we have previously fabricated such Hankel-phased circular Bragg lasers in InGaAsP active semiconductor material [73], we will use the layer structure therein as an example for our numerical study. The target lasing wavelength λ_0 is 1.55 μm . For simplicity, we approximate the complicated layer structure by an effective index profile

Table 8.1. Approximated layer structure for numerical study

Layer description	Refractive index n	Thickness
Upper cladding	1.54	∞
Third layer	3.281	60.5 nm
Second layer (active region)	3.4057	129 nm
First layer	3.281	60.5 nm
Lower cladding	1.54	∞

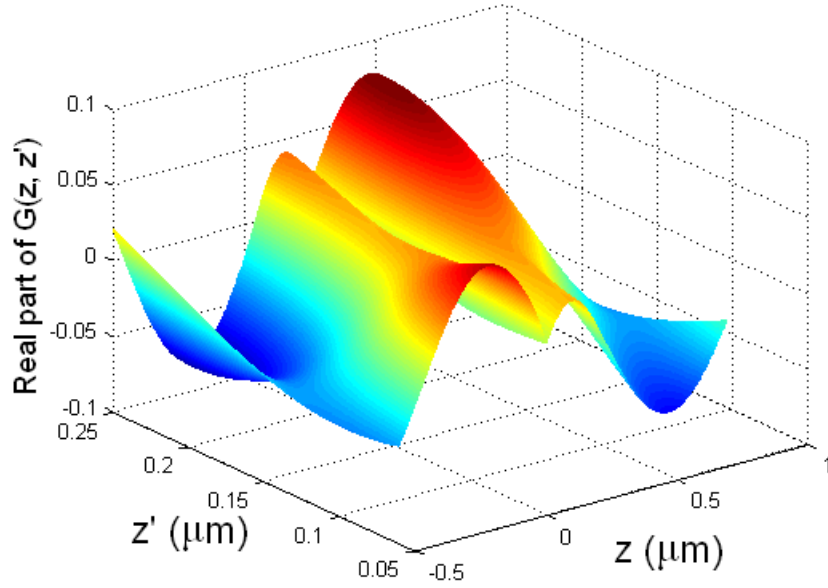


Fig. 8.1. Real part of the Green's function $G(z, z')$ with $-\infty < z < \infty$ and z' between the top and bottom surfaces of the laser resonator.

comprising five layers as illustrated in Table 8.1. The vertical mode profile $Z(z)$ and the effective index n_{eff} can be obtained numerically using a 1-D mode solver. The effective index n_{eff} was calculated to be 2.83 and the in-plane propagation constant $\beta = k_0 n_{\text{eff}} = 11.47 \mu\text{m}^{-1}$. Numerical calculations of the mode profile and effective index of the approximated layer structure indicate negligible deviations from those of the exact one.

We focus our analysis on the case of a partially etched grating with an etch depth of 185 nm. The numerical Green's function $G(z, z')$ that satisfies Eq. (8.14) with the given layer structure was calculated based on the recipe shown in Appendix B. A surface plot of the real part of $G(z, z')$ is displayed in Fig. 8.1.

To favor a circularly symmetric laser mode, $m = 0$ is specially chosen in the grating phase design. In such case, a Hankel-phased grating modulation with rectangular profile

$$\Theta(\Phi[H_m^{(1)}(x)], \alpha) = \begin{cases} 1, & \cos(\Phi[H_m^{(1)}(x)]) \geq \alpha, \\ 0, & \cos(\Phi[H_m^{(1)}(x)]) < \alpha, \end{cases} \quad (8.25)$$

can be expanded in Fourier series as

$$\begin{aligned} & \frac{\arccos \alpha}{\pi} + \frac{2}{\pi} \sum_{l=1}^{\infty} \frac{\sin(l \arccos \alpha)}{l} \cos(l \Phi[H_m^{(1)}(x)]) \\ &= \frac{\arccos \alpha}{\pi} + \frac{2}{\pi} \left[\sin(\arccos \alpha) \cos(\Phi[H_m^{(1)}(x)]) + \frac{\sin(2 \arccos \alpha)}{2} \cos(2 \Phi[H_m^{(1)}(x)]) + \dots \right] \\ &= d_c + \frac{1}{2\pi} \sin(2\pi d_c) \left[\exp(-i2\Phi[H_m^{(1)}(x)]) + \exp(i2\Phi[H_m^{(1)}(x)]) \right] \\ & \quad + \frac{1}{\pi} \sin(\pi d_c) \left[\exp(-i\Phi[H_m^{(1)}(x)]) + \exp(i\Phi[H_m^{(1)}(x)]) \right] + \dots \end{aligned} \quad (8.26)$$

The expansion yields the coefficients

$$a_2 = a_{-2} = \frac{\sin(2\pi d_c)}{2\pi},$$

and

$$a_1 = a_{-1} = \frac{\sin(\pi d_c)}{\pi},$$

where

$$d_c \equiv \frac{\arccos \alpha}{\pi} \quad (-1 < \alpha < 1, \quad 0 < d_c < 1)$$

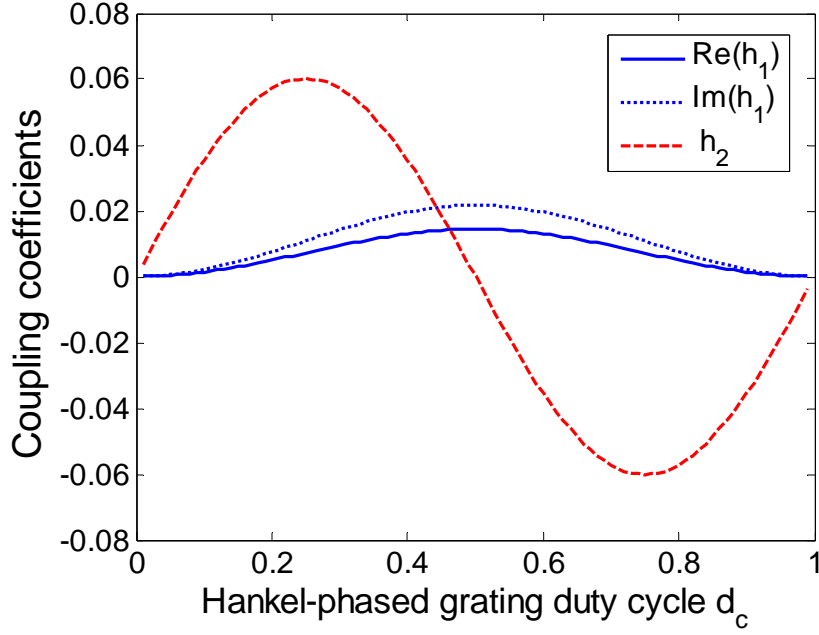


Fig. 8.2. Radiation coupling coefficient h_1 and feedback coupling coefficient h_2 as a function of the duty cycle d_c of the Hankel-phased rectangular grating.

is the duty cycle of the Hankel-phased rectangular grating. It should be emphasized that the duty cycle has a significant role in determining the coupling coefficients h_1 and h_2 [74]. Figure 8.2 plots h_1 and h_2 as a function of the duty cycle d_c . A judicious choice would be $d_c = 0.25$ where h_2 is maximal and $\text{Re}(h_1)$ is not small so that we can have a large ratio of vertical emission to power leakage, hence a high emission efficiency. Based on Eqs. (8.18) and (8.19), the grating's coupling coefficients were found to be $h_1 = 0.0072 + 0.0108i$ and $h_2 = 0.0601$. Calculated from Eq. (8.13), s_1 and s_{-1} at the emission surface (i.e., the top surface of the laser resonator) were found to be $0.1725 - 0.0969i$.

Chapter 9

Mode-Solving Methods

Taking into account the resonant vertical laser radiation, Section 8.1 presents a derivation of a comprehensive coupled-mode theory for the Hankel-phased circular grating structures in active media. The effect of vertical radiation is incorporated into the coupled in-plane wave equations by a numerical Green's function method. The in-plane (vertically confined) electric field is expressed as

$$E(x) = A(x)H_m^{(1)}(x) + B(x)H_m^{(2)}(x), \quad (9.1)$$

where $H_m^{(1)}(x)$ and $H_m^{(2)}(x)$ are the m th-order Hankel functions that represent respectively the in-plane outward and inward propagating cylindrical waves. A set of evolution equations for the amplitudes $A(x)$ and $B(x)$ is obtained:

$$\frac{dA(x)}{dx} = u(x) \cdot A(x) - v(x) \cdot B(x) \cdot e^{2i\delta \cdot x}, \quad (9.2)$$

$$\frac{dB(x)}{dx} = -u(x) \cdot B(x) + v(x) \cdot A(x) \cdot e^{-2i\delta \cdot x}, \quad (9.3)$$

where

$x = \beta\rho$: normalized radial coordinate with β being the in-plane propagation constant;

$\delta = (\beta_{\text{design}} - \beta)/\beta$: frequency detuning factor, representing a relative frequency shift of a resonant mode from the designed value;

$$u(x) = \begin{cases} g_A(x) - h_1, & \text{for } x \text{ in a grating region,} \\ g_A(x), & \text{for } x \text{ in a no-grating region;} \end{cases}$$

$$v(x) = \begin{cases} h_1 + ih_2, & \text{for } x \text{ in a grating region,} \\ 0, & \text{for } x \text{ in a no-grating region;} \end{cases}$$

$h_1 = h_{1r} + ih_{1i}$: grating's radiation coupling coefficient, representing the effect of vertical laser radiation on the in-plane modes;

h_2 : grating's feedback coupling coefficient, which can always be chosen real;

$g_A(x) = g(x) - \alpha$: space-dependent net gain coefficient, the minimum value of which required to achieve laser emission will be solved analytically or numerically;

α : nonsaturable internal loss, including absorption and nonradiative scattering losses;

$g(x) = g_0(x)/[1 + I(x)/I_{\text{sat}}]$: intensity-dependent saturated gain profile;

$g_0(x)$: unsaturated gain profile; and

$I(x)/I_{\text{sat}}$: field intensity distribution in units of saturation intensity.

It should be noted that, although Eqs. (9.2) and (9.3) appear to be a set of coupled equations for in-plane waves only, they implicitly include the effect of vertical radiation due to h_1 . As it will become clearer in Section 9.3, the vertical radiation can simply be treated as a loss term during the process of solving the in-plane laser modes.

This chapter is reproduced and adapted with permission from [75-77], © 2008, 2009 OSA.

9.1 Analytical Mode-Solving Method

When solving the modes at threshold with uniform gain (or pump) distribution across the device, the net gain coefficient g_A is x independent. The generic solutions of Eqs. (9.2) and (9.3) in no-grating regions are trivial:

$$A(x) = A_0 e^{g_A x}, \quad (9.4)$$

$$B(x) = B_0 e^{-g_A x}. \quad (9.5)$$

In grating regions, by introducing $\tilde{A}(x) = A(x)e^{-i\delta x}$ and $\tilde{B}(x) = B(x)e^{i\delta x}$, Eqs. (9.2) and (9.3) become

$$\frac{d\tilde{A}(x)}{dx} = (u - i\delta) \tilde{A}(x) - v \tilde{B}(x), \quad (9.6)$$

$$\frac{d\tilde{B}(x)}{dx} = -(u - i\delta) \tilde{B}(x) + v \tilde{A}(x), \quad (9.7)$$

whose generic solutions lead to

$$A(x) = A(0) e^{i\delta x} \frac{\sinh[S(x-L)] + \mathbb{C} \cosh[S(x-L)]}{-\sinh[SL] + \mathbb{C} \cosh[SL]}, \quad (9.8)$$

$$B(x) = \frac{A(0) e^{-i\delta x}}{v} \cdot \frac{[(u - i\delta) - \mathbb{C}S] \sinh[S(x-L)] + [\mathbb{C}(u - i\delta) - S] \cosh[S(x-L)]}{-\sinh[SL] + \mathbb{C} \cosh[SL]}, \quad (9.9)$$

where $S \equiv \sqrt{(u - i\delta)^2 - v^2}$, \mathbb{C} is a constant to be determined by specific boundary conditions, and L is a normalized length parameter (see Fig. 9.1). The determination of the constant \mathbb{C} in Eqs. (9.8) and (9.9) requires the specific boundary conditions be applied to the grating under investigation.

We focus on two typical boundary conditions to obtain \mathbb{C} and the corresponding field reflectivity in each case.

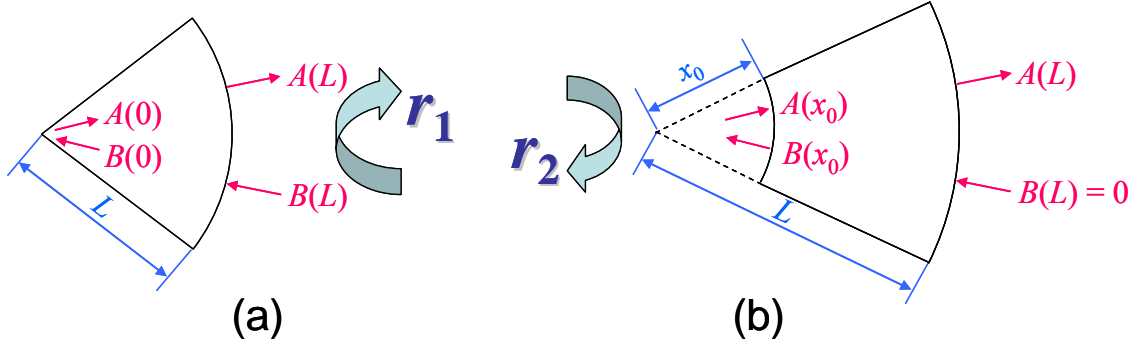


Fig. 9.1. Two types of boundary conditions for calculating reflectivities. (a) $A(0) = B(0)$, $r_1(L) = A(L)/B(L)$; (b) $B(L) = 0$, $r_2(x_0, L) = B(x_0)/A(x_0)$.

Case I: As shown in Fig. 9.1(a), the grating extends from the center $x = 0$ to $x = L$. An inward propagating wave with amplitude $B(L)$ impinges from outside on the grating. The reflectivity is defined as $r_1(L) = A(L)/B(L)$. The finiteness of $E(x)$ at the center $x = 0$ requires $A(0) = B(0)$, leading to

$$\mathbb{C} = \frac{(u - v - i\delta) \sinh[SL] + S \cosh[SL]}{S \sinh[SL] + (u - v - i\delta) \cosh[SL]}$$

and to the reflectivity

$$r_1(L) = \frac{A(L)}{B(L)} = e^{2i\delta L} \frac{(u - v - i\delta) \sinh[SL] + S \cosh[SL]}{-(u - v - i\delta) \sinh[SL] + S \cosh[SL]}. \quad (9.10)$$

Case II: As shown in Fig. 9.1(b), the grating extends from $x = x_0$ to $x = L$. An outward propagating wave with amplitude $A(x_0)$ impinges from inside on the grating. The reflectivity is defined as $r_2(x_0, L) = B(x_0)/A(x_0)$. No inward propagating wave comes from outside of the grating, i.e., $B(L) = 0$. This condition leads to $\mathbb{C} = S/(u - i\delta)$ and to the reflectivity

$$r_2(x_0, L) = \frac{B(x_0)}{A(x_0)} = e^{-2i\delta x_0} \frac{v \sinh[S(L - x_0)]}{(u - i\delta) \sinh[S(L - x_0)] - S \cosh[S(L - x_0)]}. \quad (9.11)$$

It should be noted that, as seen from their definitions, the above reflectivities Eqs. (9.10) and (9.11) include the propagation phase.

With the obtained reflectivities for the two types of boundary conditions, it is easy to derive the laser threshold condition for each circular Bragg laser configuration.

(1) Circular DFB laser:

The limiting cases $r_1(x_b) \rightarrow \infty$ or $r_2(0, x_b) = 1$ lead to the same result

$$\tanh[Sx_b] = \frac{S}{u - v - i\delta}. \quad (9.12)$$

(2) Disk Bragg laser:

Considering the radially propagating waves in the disk and taking the unity reflectivity at the center, the threshold condition is $1 \cdot e^{2g_A x_0} \cdot r_2(x_0, x_b) = 1$, which reads

$$\frac{e^{2(g_A - i\delta)x_0} \cdot v \cdot \sinh[S(x_b - x_0)]}{(u - i\delta) \sinh[S(x_b - x_0)] - S \cosh[S(x_b - x_0)]} = 1. \quad (9.13)$$

(3) Ring Bragg laser:

Considering the radially propagating waves in the annular defect, the threshold condition is $r_1(x_L) \cdot e^{2g_A(x_R - x_L)} \cdot r_2(x_R, x_b) = 1$, which reads

$$\frac{(u - v - i\delta) \sinh[Sx_L] + S \cosh[Sx_L]}{-(u - v - i\delta) \sinh[Sx_L] + S \cosh[Sx_L]} \cdot \frac{e^{2(g_A - i\delta)(x_R - x_L)} \cdot v \cdot \sinh[S(x_b - x_R)]}{(u - i\delta) \sinh[S(x_b - x_R)] - S \cosh[S(x_b - x_R)]} = 1. \quad (9.14)$$

The above threshold conditions Eqs. (9.12), (9.13), and (9.14) govern the modes of the lasers of each type and will be used to obtain their threshold gains (g_A) and corresponding detuning factors (δ). With these values, substituting Eqs. (9.4), (9.5), (9.8), and (9.9) into

Eq. (9.1) and then matching them at the interfaces yields the corresponding in-plane modal field patterns. Despite their much simpler and more direct forms, these threshold conditions automatically satisfy the requirements that $E(x)$ and $E'(x)$ be continuous at every interface between the grating and no-grating regions [78].

9.2 Numerical Mode-Solving Method

When solving the modes at threshold with uniform gain (or pump) distribution across the device, g_A is independent of x so that Eqs. (9.2) and (9.3) can have analytical solutions Eqs. (9.4) and (9.5), or (9.8) and (9.9). In the case of using a nonuniform pump profile and/or taking into account the gain saturation effect in above-threshold operation, g_A becomes dependent on x and Eqs. (9.2) and (9.3) have to be solved numerically. The modes are then obtained by identifying those satisfying the boundary conditions.

As explained in Section 9.1, the same boundary conditions (BCs) apply to all the three types of circular Bragg lasers: (i) $A(0) = B(0)$; (ii) $B(x_b) = 0$; (iii) $A(x)$ and $B(x)$ continuous for $0 < x < x_b$. In Eqs. (9.2) and (9.3), $g_0(x)$ for a certain gain distribution profile can be parameterized with a proportionality constant, say, its maximal value g_0 .

The mode-solving procedure is as follows: Having BC(i), we start with an amplitude set $[A \ B] = A(0)[1 \ 1]$ at the center, then numerically integrate Eqs. (9.2) and (9.3) along x to the exterior boundary x_b , during which both A and B values are kept continuous at every interface between grating and no-grating regions to satisfy BC(iii). After the integration, we have $B(x_b)$ whose absolute value marks a contour map in the 2-D plane of g_0 and δ . Now each minimum point in this contour map satisfies BC(ii) and thus

represents a mode with corresponding g_0 and δ . Retrieving $A(x)$ and $B(x)$ for this mode and substituting them into Eq. (9.1) give the modal field pattern.

We can also calculate the modal pump level using the obtained g_0 . Assuming a linear pump–gain relationship above transparency, the unsaturated gain $g_0(x)$ follows the profile of pump intensity $I_{\text{pump}}(x)$, and we may define the pump level $P_{\text{pump}} \equiv \int I_{\text{pump}}(x) \cdot 2\pi\rho \cdot d\rho = P_0 \int g_0(x) \cdot x \cdot dx$, where P_0 having a power unit is a proportionality constant determined by specific experimental setup. For simple $g_0(x)$ profiles, P_{pump} can have analytical expressions as will be shown in Section 11.2, otherwise, numerical integration always remains an option.

9.3 Mode-Solving Accuracy Check

In this section we derive an energy relation on which the examination of mode-solving accuracy is based. This energy relation is a direct result of the coupled-mode equations (9.2) and (9.3) combined with the boundary conditions and thus is exact.

Similar to the procedure in [79], multiplying Eq. (9.2) by A^* and Eq. (9.3) by B^* , then adding each equation to its complex conjugate, one obtains

$$\frac{d|A|^2}{dx} = 2(g_A - h_{1r})|A|^2 - v \cdot A^* B \cdot e^{2i\delta x} - v^* \cdot AB^* \cdot e^{-2i\delta x}, \quad (9.15)$$

$$\frac{d|B|^2}{dx} = -2(g_A - h_{1r})|B|^2 + v \cdot AB^* \cdot e^{-2i\delta x} + v^* \cdot A^* B \cdot e^{2i\delta x}. \quad (9.16)$$

Subtracting Eq. (9.16) from Eq. (9.15) yields

$$\frac{d}{dx}(|A|^2 - |B|^2) = 2g_A(|A|^2 + |B|^2) - 2h_{1r}|Ae^{-i\delta x} + Be^{i\delta x}|^2. \quad (9.17)$$

Integrating Eq. (9.17) from $x = 0$ to $x = x_b$ and applying the boundary conditions $A(0) = B(0)$ and $B(x_b) = 0$ leads to

$$\underbrace{\left|A(x_b)\right|^2}_{\text{peripheral leakage}} + \underbrace{2h_{1r} \int_{\text{grating}} \left|Ae^{-i\delta x} + Be^{i\delta x}\right|^2 dx}_{\text{vertical laser emission}} = \underbrace{2 \int_0^{x_b} g_A \left(|A|^2 + |B|^2\right) dx}_{\text{power generated in the gain medium}}, \quad (9.18)$$

which is interpreted as the energy conservation theorem for the surface-emitting circular Bragg lasers. This equation states that, in steady state, the net power generated in the gain medium is equal to the sum of peripheral leakage power and vertical emission power. Due to its exactness, we may use this relation to monitor the accuracy of mode solving by substituting into Eq. (9.18) the obtained modal $g_0(x)$, δ , $A(x)$, and $B(x)$ and comparing the left-hand and right-hand sides of the equation.

As an aside, it should be noted that all the power terms in Eq. (9.18) are in units of a saturation power defined by

$$P_{\text{sat}} \equiv E_{\text{sat}}^2 4D/\beta, \quad (9.19)$$

where E_{sat} is the saturation field that relates to the saturation intensity by $I_{\text{sat}} = cn\varepsilon_0|E_{\text{sat}}|^2/2$ (c , the speed of light; n , transverse effective index; ε_0 , the vacuum permittivity), and D is the thickness (vertical dimension) of the laser resonator.

Chapter 10

Near-Threshold Modal Properties

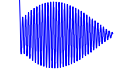
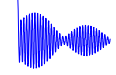
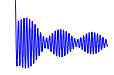


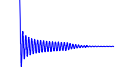
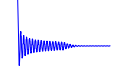
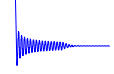
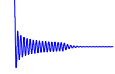
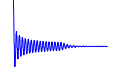
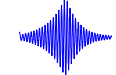
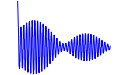

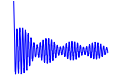
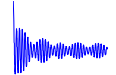
This chapter is reproduced and adapted with permission from [75, 76], © 2008, 2009 OSA.

10.1 Threshold, Frequency Detuning, and In-Plane Modal Pattern

For numerical demonstration, we assume all the lasers possess a vertical layer structure as described in [73] that was designed for 1.55- μm laser emission. The grating design procedure is detailed in Section 8.2. The effective index n_{eff} is calculated to be 2.83 and the in-plane propagation constant $\beta = k_0 n_{\text{eff}} = 11.47 \mu\text{m}^{-1}$. The circular grating is designed to follow the phase of Hankel functions with $m = 0$ to favor circularly symmetric modes. A quarter duty cycle is chosen to have both large feedback for in-plane waves while keeping a considerable amount of vertical emission. The coupling coefficients were found to be $h_1 = 0.0072 + 0.0108i$ and $h_2 = 0.0601$.

Since we would like to compare the modal properties of different types of lasers with a same footprint, a typical device size of $x_b = 200$ (corresponding to $\rho_b \approx 17.4 \mu\text{m}$) is assumed for all. For the disk Bragg laser, the inner disk radius x_0 is assumed to be $x_b/2 = 100$. For the ring Bragg laser, the annular defect is assumed to be located at the middle

Table 10.1. Modal field patterns, along with their threshold gains (g_A) and frequency detuning factors (δ), of the circular DFB, disk, and ring Bragg lasers. All the three types of lasers have an exterior boundary radius of $x_b = 200$

Mode number		1	2	3	4	5
Circular DFB laser	Modal field					
	$g_A (10^{-3})$	0.283	1.03	2.04	3.11	4.12
	$\delta (10^{-3})$	61.8	66.6	74.1	83.6	94.6
Disk Bragg laser	Modal field					
	$g_A (10^{-3})$	0.127	0.288	0.454	0.690	1.21
	$\delta (10^{-3})$	49.8	21.2	-8.09	-37.4	-66.5
Ring Bragg laser	Modal field					
	$g_A (10^{-3})$	0.457	1.06	1.92	3.14	4.09
	$\delta (10^{-3})$	55.9	66.9	71.0	84.4	91.6

$x_b/2 = 100$ and the defect width is set to be a wavelength of the cylindrical waves therein, yielding $x_L + x_R = x_b = 200$ and $x_R - x_L = 2\pi$. The calculated modal field patterns, along with the corresponding threshold gain values (g_A) and frequency detuning factors (δ), of the circular DFB, disk, and ring Bragg lasers are listed in Table 10.1.

A comparison of these modal properties concludes the following features of the three laser structures:

- (1) All the displayed modes of the circular DFB laser are in-band modes on one side of the bandgap (all $\delta > 0$). This is due to the radiation coupling induced mode selection mechanism [80]. Increased gain results in the excitation of higher-order modes.

- (2) All the displayed modes of the disk Bragg laser are confined to the center disk with negligible peripheral power leakage and thus possess very low thresholds and very small modal volumes as will be shown in Section 10.3.
- (3) All the displayed modes of the ring Bragg laser, with the exception of the fundamental defect mode, resemble their counterparts of the circular DFB laser. The defect mode has a larger threshold gain than the fundamental mode of the circular DFB laser, but the former possesses a much higher emission efficiency as will be shown in Section 10.3.

10.2 Radiation Field and Far-Field Pattern

As mentioned earlier, by implementing a second-order circular grating design, the gratings can not only provide feedback for the in-plane fields but also couple the laser emission vertically out of the resonator plane. As derived in Section 8.1, Eq. (8.12) relates the in-plane fields with the vertical radiation field in the grating regions. The radiation pattern at the emission surface is known as the near-field. For the grating design with $m = 0$, the near-field is expressed as

$$\Delta E = \left(s_1 A e^{-i\delta x} + s_{-1} B e^{i\delta x} \right) \left| H_0^{(1)} \right|, \quad (10.1)$$

where s_1 and s_{-1} at the emission surface can be obtained numerically according to Eq. (8.13) for a given grating structure. Following the design procedure in Section 8.2, both s_1 and s_{-1} at the emission surface were calculated to be $0.1725 - 0.0969i$. Using the Huygens–Fresnel principle, the diffracted far-field radiation pattern of light from a circular aperture can be calculated under the parallel ray approximation ($|\mathbf{r}| \gg |\mathbf{r}'|$) [81]:

$$\begin{aligned}
U(\mathbf{r}) &\propto \iint_{\text{aperture}} \Delta E(\rho, \varphi) \frac{\exp(ik|\mathbf{r} - \mathbf{r}'|)}{4\pi|\mathbf{r} - \mathbf{r}'|} d\mathbf{r}' \\
&\approx \frac{e^{ikr}}{4\pi r} \iint_{\text{aperture}} \Delta E(\rho, \varphi) \exp(-ik(\mathbf{r}' \cdot \hat{\mathbf{r}})) d\mathbf{r}' \\
&= \frac{e^{ikr}}{4\pi r} \int_{\varphi=0}^{2\pi} \int_{\rho=0}^{\rho_b} \Delta E(\rho) \exp[-ik\rho \sin\theta \cos(\varphi - \phi)] \rho d\rho d\varphi \\
&= \frac{e^{ikr}}{2r} \int_0^{\rho_b} \Delta E(\rho) J_0(k\rho \sin\theta) \rho d\rho,
\end{aligned} \tag{10.2}$$

where

$$\mathbf{r}' = \rho \cos \varphi \hat{\mathbf{x}} + \rho \sin \varphi \hat{\mathbf{y}}$$

is the source point and

$$\mathbf{r} = r \sin \theta \cos \phi \hat{\mathbf{x}} + r \sin \theta \sin \phi \hat{\mathbf{y}} + r \cos \theta \hat{\mathbf{z}}$$

is the field point. The far-field intensity pattern is then given by

$$I(\mathbf{r}) = U^*(\mathbf{r})U(\mathbf{r}) = |U(\mathbf{r})|^2 \tag{10.3}$$

and plotted in Fig. 10.1 for the fundamental mode of circular DFB, disk, and ring Bragg lasers.

In the far-field patterns, the different lobes correspond to different diffraction orders of the light emitted from the circular aperture. In the circular DFB and ring Bragg lasers, most of the energy is located in the first-order Fourier component thus their first-order diffraction peaks dominate. In the disk Bragg laser it is obvious that the zeroth-order peak dominates. These calculation results are similar to some of the experimental data for circular DFB and DBR lasers [82, 83].

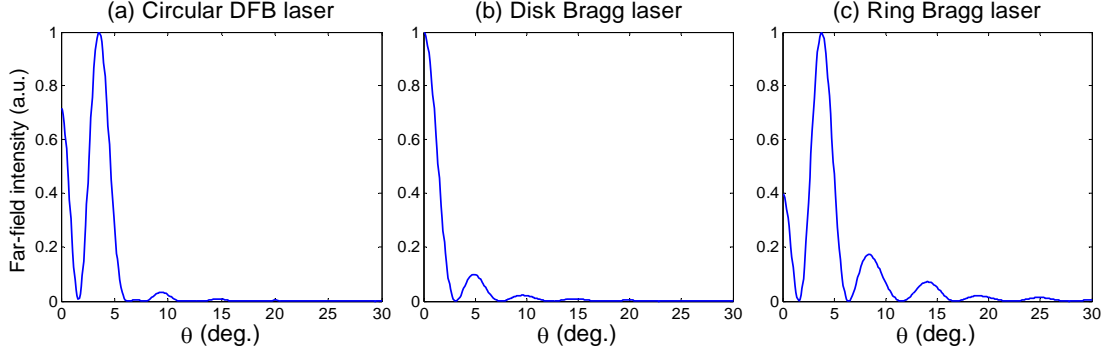


Fig. 10.1. Far-field intensity patterns of the fundamental mode of (a) circular DFB, (b) disk, and (c) ring Bragg lasers.

10.3 Single-Mode Range, Quality Factor, Modal Area, and Internal Emission Efficiency

In the previous sections we have compared the modal properties for devices with a fixed exterior boundary radius $x_b = 200$. In what follows we will vary the device size and investigate the size dependence of modal gains to determine the single-mode range for each laser type. Within each own single-mode range limit, the fundamental mode of these lasers will be used to calculate and compare the quality factor, modal area, and internal emission efficiency. Similar to the prior calculations with a fixed x_b , we still keep $x_0 = x_b/2$ for the disk Bragg laser and $x_L + x_R = x_b$, $x_R - x_L = 2\pi$ for the ring Bragg laser even as x_b varies.

Single-Mode Range

In the circular Bragg lasers, since a longer radial Bragg grating can provide stronger feedback for in-plane waves, larger devices usually require a lower threshold gain. The downside is that a larger size also results in smaller modal discrimination, which is

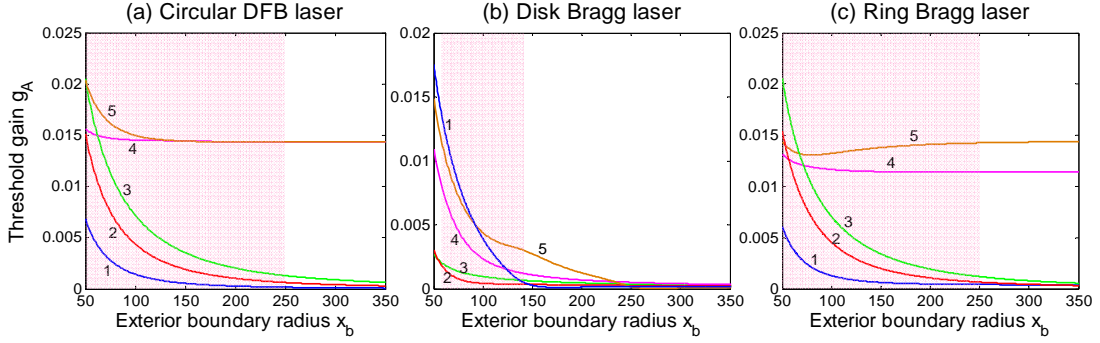


Fig. 10.2. Evolution of threshold gains of the 5 lowest-order modes of (a) circular DFB, (b) disk, and (c) ring Bragg lasers. The modes are labeled in accord with those shown in Table 10.1. The single-mode range for each laser type is marked in pink.

unfavorable for single-mode operation in these lasers. As a result, there exists a range of the exterior boundary radius x_b values for each laser type within which range the single-mode operation can be achieved. This range is referred to as the “single-mode range.” Figure 10.2 plots the evolution of threshold gains for the 5 lowest-order modes as x_b varies from 50 to 350. The single-mode ranges for the circular DFB, disk, and ring Bragg lasers are 50–250, 60–140, and 50–250, respectively, which are marked as the pink regions. Since single-mode operation is usually preferred in laser designs, in the rest of this section we will limit x_b to remain within each single-mode range and focus on the fundamental mode only.

Quality Factor

As a measure of the speed with which a resonator dissipates its energy, the quality factor Q for optical resonators is usually defined as $\omega\mathcal{E}/P$ where ω denotes the radian resonance frequency, \mathcal{E} the total energy stored in the resonator, and P the power loss. In

our surface-emitting circular Bragg lasers, the power loss P has two contributions: coherent vertical laser emission coupled out of the resonator due to the first-order Bragg diffraction, and peripheral power leakage due to the finite radial length of the Bragg reflector.

Jebali et al. recently developed an analytical formalism to calculate the Q factor for first-order circular grating resonators using a 2-D model in which the in-plane peripheral leakage was considered as the only source of power loss [84]. To include the vertical emission as another source of the power loss, a rigorous analytical derivation of the Q factor requires a 3-D model be established. This is much more complicated than the 2-D case. However, since we are interested in comparing different laser types, a relative Q value will be good enough. Considering that the energy stored in a volume is proportional to $\int |\mathbf{E}|^2 dV$ and that the outflow power through a surface is proportional to $\int |\mathbf{E}|^2 dS$, we define an unnormalized quality factor

$$\begin{aligned}
 Q' &= \frac{\int_0^D dz \int_0^{2\pi} d\varphi \int_0^{\rho_b} |E(\rho, z)|^2 \rho d\rho}{\iint_{\text{grating}} |\Delta E(\rho, z=0)|^2 \rho d\rho d\varphi + \int_0^D dz \int_0^{2\pi} |E(\rho = \rho_b, z)|^2 \rho_b d\varphi} \\
 &= \frac{\int_0^D Z^2(z) dz \cdot \int_0^{x_b} |E(x)|^2 x dx}{\int_{\text{grating}} |\Delta E(x, z=0)|^2 x dx + \int_0^D Z^2(z) dz \cdot |E(x = x_b)|^2 \beta x_b},
 \end{aligned} \tag{10.4}$$

where $Z(z)$ denotes the vertical mode profile for a given layer structure [see Eq. (8.3)] and D the thickness of the laser resonator. For a circularly symmetric mode, the angular integration factors are canceled out. The expressions for the in-plane field E and radiation field ΔE are given by Eqs. (9.1) and (10.1), respectively.

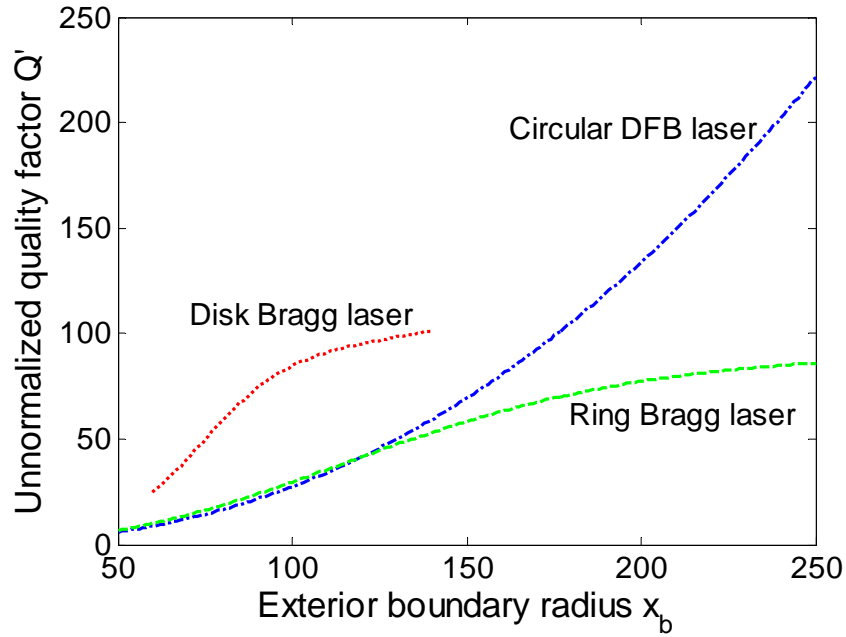


Fig. 10.3. Unnormalized quality factor of circular DFB, disk, and ring Bragg lasers.

The unnormalized quality factor Q' as defined in Eq. (10.4) is obviously proportional to an exact Q , and the former is more intuitive and convenient for calculational purposes. The Q' of the fundamental mode for the three laser types is calculated and displayed in Fig. 10.3. As expected, increase in the device size (x_b) results in an enhanced Q' value for all three types of lasers. Additionally, the disk Bragg laser exhibits a much higher Q' than the other two laser structures of identical dimensions. As an example, for $x_b = 100$, the Q' value of the disk Bragg laser is approximately 3 times greater than that of the circular DFB or ring Bragg lasers. This is consistent with their threshold behaviors shown in Table 10.1.

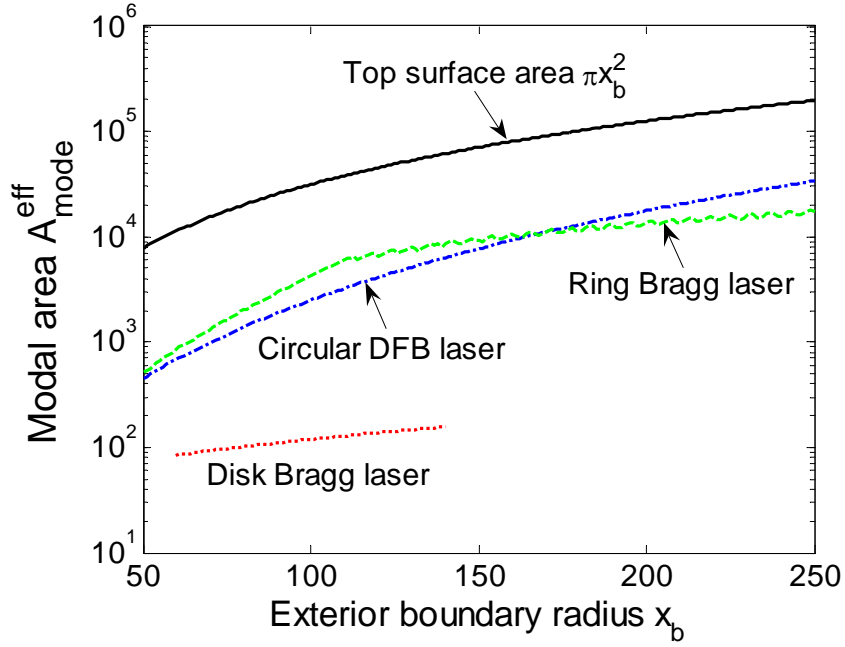


Fig. 10.4. Modal area of circular DFB, disk, and ring Bragg lasers. The top surface area of the laser resonator (πx_b^2) is also plotted as a reference.

Modal Area

Based on the definition of modal volume [85], an effective modal area is similarly defined:

$$A_{\text{mode}}^{\text{eff}} = \frac{\iint |\mathbf{E}|^2 x dx d\varphi}{\max\{|\mathbf{E}|^2\}}. \quad (10.5)$$

The modal area is a measure of how the modal field is distributed within the resonator. A highly localized mode having a small modal area can have strong interaction with the emitter. Figure 10.4 plots $A_{\text{mode}}^{\text{eff}}$ of the fundamental mode, within each single-mode range, for the three laser types. The top surface area of the laser resonator (πx_b^2) is also plotted to serve as a reference. The modal area of the disk Bragg laser is found to be at least one

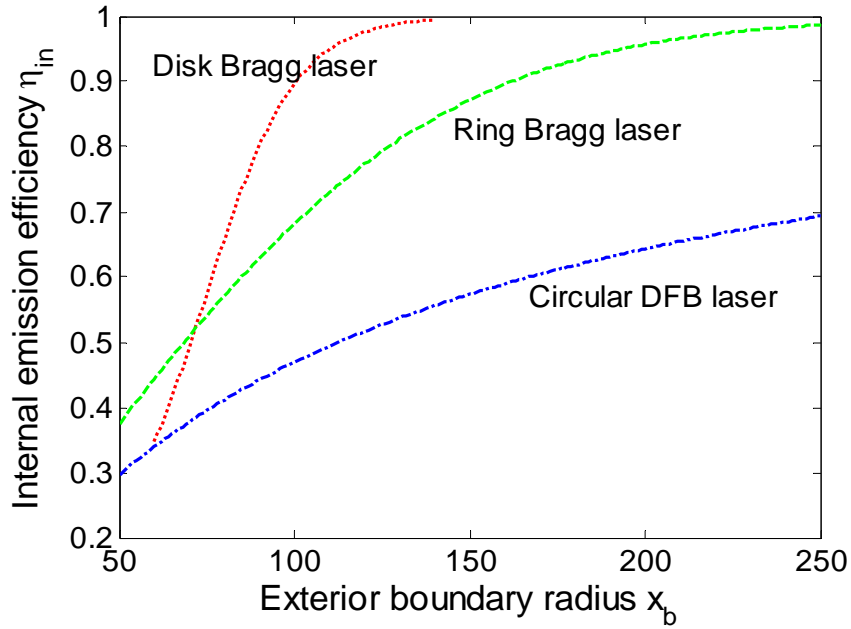


Fig. 10.5. Internal emission efficiency of circular DFB, disk, and ring Bragg lasers.

order of magnitude lower than those of the circular DFB and ring Bragg lasers. This is not surprising and can be inferred from their unique modal profiles listed in Table 10.1.

Internal Emission Efficiency

As mentioned earlier, the generated net power in the circular Bragg lasers is dissipated by two kinds of loss: vertical laser emission and peripheral power leakage. The internal emission efficiency η_{in} is thus naturally defined as the fraction of the total power loss that is represented by the useful vertical laser emission. Figure 10.5 depicts the η_{in} of the fundamental mode, within each single-mode range, for the three laser types. As expected, all the lasers possess a larger η_{in} with a larger device size. Comparing devices of identical dimensions, only the disk and ring Bragg lasers achieve high emission efficiencies. This

is a result of their fundamental modes being located in a bandgap while the circular DFB laser's fundamental mode is at a band edge, i.e., in a band. Bandgap modes experience much stronger reflection from the Bragg gratings, yielding less peripheral power leakage than in-band modes.

Summary of Comparison

In this section, by varying the device size we have obtained the single-mode range and compared the quality factor, modal area, and internal emission efficiency of the three types of lasers. It is demonstrated that, under similar conditions, disk Bragg laser has the highest quality factor, the smallest modal area, and the highest internal emission efficiency, indicating its suitability in high-efficiency, low-threshold, ultracompact laser design, while ring Bragg laser has a large single-mode range, large modal area, and high internal emission efficiency, indicating its wide application as a high-efficiency, large-area laser.

Chapter 11

Above-Threshold Modal Properties

In Chapter 10 we have solved the modes and compared the near-threshold modal properties of the three types of surface-emitting circular Bragg lasers. This chapter focuses on an above-threshold modal analysis that includes the gain saturation effect. The coupled-mode equations (9.2) and (9.3) will be solved numerically with boundary conditions. The relation of surface emission power versus pump power will be simulated. The laser threshold and external emission efficiency will be compared for these lasers under different pump profiles. Last, with the device size varying in a large range, the evolution curve of pump level for several lowest-order modes will be generated and the optimal design guidelines for these lasers will be suggested.

This chapter is reproduced and adapted with permission from [76, 77], © 2009 OSA.

11.1 Surface Emission Power versus Pump Power Relation

The numerical mode-solving recipe is described in detail in Section 9.2. Simply put, Eqs. (9.2) and (9.3) are integrated along x from $x = 0$ to $x = x_b$ with the initial boundary condition $[A \ B] = A(0)[1 \ 1]$. By identifying those satisfying the final boundary condition $B(x_b) = 0$ one finds the modes with corresponding g_0 and δ . The modal pump level is then

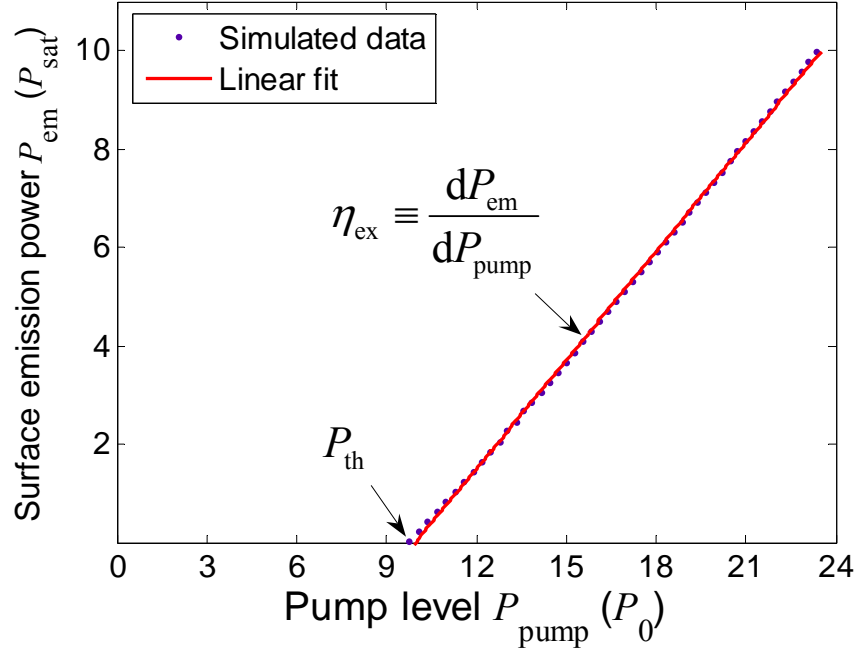


Fig. 11.1. Surface emission power P_{em} (in units of P_{sat}) versus pump power level P_{pump} for the fundamental mode of circular DFB laser ($x_b = 200$) under uniform pumping. The laser threshold P_{th} is defined as the pump level at the onset of surface laser emission. The external emission efficiency η_{ex} is defined as the slope of the linear fit of the simulated data points up to $P_{\text{em}} = 10P_{\text{sat}}$.

given by $P_{\text{pump}} = \int g_0(x) \cdot x \cdot dx$ in units of a proportionality constant P_0 . Explained in Section 9.3, the surface emission power P_{em} from the laser is just the second term on the left-hand side of Eq. (9.18). By varying the value of $A(0)$ at the beginning of the integration process, we are able to get the $(P_{\text{pump}}, P_{\text{em}})$ pairs, which basically form the typical input–output relation for a laser mode.

As an example, we consider the circular DFB laser with $x_b = 200$ and the other structural parameters the same as those used in Chapter 10. The additional parameter used in the numerical integration, the nonsaturable internal loss α , is assumed to be

0.2×10^{-3} (already normalized by β) for typical III–V quantum well lasers. With the simulated $(P_{\text{pump}}, P_{\text{em}})$ pairs, the typical laser input–output relation is obtained for the fundamental mode and plotted in Fig. 11.1. The laser threshold P_{th} is defined as the pump level at the onset of surface laser emission. The external emission efficiency (or, energy conversion efficiency) η_{ex} is defined as the slope $dP_{\text{em}}/dP_{\text{pump}}$ of the linear fit of the simulated data points up to $P_{\text{em}} = 10P_{\text{sat}}$. As can be seen, the output power varies linearly with the pump power above threshold, which is in agreement with the theoretical and experimental results for typical laser systems (see, e.g., Section 9.3 of [54]).

11.2 Nonuniform Pumping Effects

So far our studies on the circular Bragg lasers have assumed a uniform pumping profile and thus a uniform gain distribution across the devices. In practical situations, the pumping profile is usually nonuniform, distributed either in a Gaussian shape in optical pumping [73, 86] or in an annular shape in electrical pumping [87]. The effects of nonuniform pumping have been investigated theoretically [88, 89] and experimentally [68] for circular DFB lasers. In this section we will study and compare the nonuniform effects on the three types

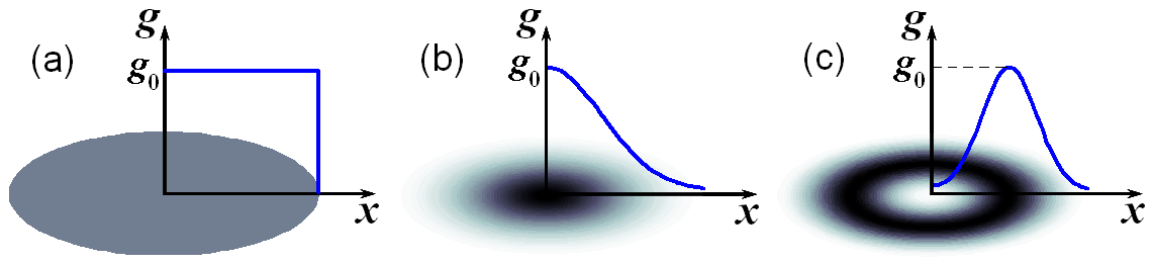


Fig. 11.2. Illustration of different pump profiles: (a) uniform; (b) Gaussian; (c) annular.

of surface-emitting circular Bragg lasers.

Let us focus on three typical pumping profiles—uniform, Gaussian, and annular—as shown in Fig. 11.2. The pump level P_{pump} can be expressed analytically in terms of the pump profile parameters:

(a) Uniform:

$$g_0(x) = g_0, \quad 0 \leq x \leq x_b, \quad P_{\text{pump}} = \int_0^{x_b} g_0 \cdot x \cdot dx = \frac{1}{2} g_0 x_b^2, \quad (11.1)$$

(b) Gaussian:

$$g_0(x) = g_0 \exp\left(-\frac{x^2}{w_p^2}\right), \quad x \geq 0, \quad P_{\text{pump}} = \int_0^\infty g_0 \exp\left(-\frac{x^2}{w_p^2}\right) \cdot x \cdot dx = \frac{1}{2} g_0 w_p^2, \quad (11.2)$$

(c) Annular:

$$g_0(x) = g_0 \left[\exp\left(-\frac{(x-x_p)^2}{w_p^2}\right) + \exp\left(-\frac{(x+x_p)^2}{w_p^2}\right) \right], \quad x \geq 0,$$

$$P_{\text{pump}} = \int_0^\infty g_0 \left[\exp\left(-\frac{(x-x_p)^2}{w_p^2}\right) + \exp\left(-\frac{(x+x_p)^2}{w_p^2}\right) \right] \cdot x \cdot dx = g_0 \left[w_p^2 \exp\left(-\frac{x_p^2}{w_p^2}\right) + \sqrt{\pi} w_p x_p \operatorname{erf}\left(\frac{x_p}{w_p}\right) \right], \quad (11.3)$$

where the error function $\operatorname{erf}(x) \equiv \frac{2}{\sqrt{\pi}} \int_0^x \exp(-t^2) dt$.

To compare the nonuniform pumping effects, the typical exterior boundary radius $x_b = 200$ is again assumed for all the circular DFB, disk, and ring Bragg lasers. In addition, for the disk Bragg laser the inner disk radius is set to be $x_0 = x_b/2$, and for the ring Bragg laser the two interfaces separating the grating and no-grating regions are located at $x_L = x_b/2 - \pi$ and $x_R = x_b/2 + \pi$. Following the calculation procedure in Section 11.1, the threshold pump level P_{th} and the external emission efficiency η_{ex} of the fundamental mode of the three types of lasers were calculated with the uniform, Gaussian, and annular

Table 11.1. Threshold pump level P_{th} (in units of P_0) and external emission efficiency η_{ex} (in units of P_{sat}/P_0) of circular DFB, disk, and ring Bragg lasers under different pump profiles

Pump profile	Circular DFB laser		Disk Bragg laser		Ring Bragg laser	
	P_{th}	η_{ex}	P_{th}	η_{ex}	P_{th}	η_{ex}
Uniform	9.760	0.7369	6.565	0.4374	13.162	0.9278
Gaussian	5.967	0.9961	2.373	0.8741	8.570	1.379
Annular	6.382	0.9742	5.855	0.7358	7.010	1.500

pump profiles, respectively, and the results are listed in Table 11.1. Without loss of generality, the Gaussian profile was assumed to follow Eq. (11.2) with $w_p = x_b/2 = 100$, and the annular profile was assumed to follow Eq. (11.3) with $x_p = x_b/2 = 100$ and $w_p = x_b/4 = 50$. The numbers shown in Table 11.1 indicate an inverse relation between P_{th} and η_{ex} . The lowest P_{th} and the highest η_{ex} are achieved with the Gaussian pump for the circular DFB and disk Bragg lasers and with the annular pump for the ring Bragg laser.

These observations can actually be understood with fundamental laser physics: In any laser system the overlap factor between the gain spatial distribution and that of the modal intensity is crucial and proportionate. In semiconductor lasers once the pump power is strong enough to induce the population inversion the medium starts to amplify light. The lasing threshold is determined by equating the modal loss with the modal gain, which is the exponential gain constant experienced by the laser mode. This modal gain is proportional to the overlap integral between the spatial distribution of the gain and that of the modal intensity. Therefore if one assumes that, to the first order, the gain is proportional to the excess pump power over the transparency, then the threshold pump level P_{th} is inversely proportional to the above overlap integral (see, e.g., Section 11.3 of

[54]). On the other hand, since the rate of simulated emission per electron and thus the gain are proportional to the modal intensity as seen by the electron (see, e.g., Section 8.3 of [54]), this leads to a direct proportion between the external emission efficiency η_{ex} and the overlap integral. The bottom line is that a larger overlap between the pump profile and the modal intensity distribution results in more efficient energy conversion in the gain medium, which consequently leads to a lower P_{th} and a higher η_{ex} .

11.3 Considerations in Optimal Design

To obtain the optimal design for these circular Bragg lasers, we will again vary their device size in a large range and inspect their size-dependent behavior. Like what we have done in Section 10.3, we will vary the exterior boundary radius x_b for all the lasers while keeping $x_0 = x_b/2$ for the disk Bragg laser and $x_L = x_b/2 - \pi$, $x_R = x_b/2 + \pi$ for the ring Bragg laser.

Figure 11.3 shows the dependence of the pump level P_{pump} and the frequency detuning factor δ on the device size x_b for the 3 lowest-order modes, under uniform pump profile, of the three types of lasers. In each subfigure, the modes are numbered in accord with those shown in Table 10.1. For both P_{pump} and δ , dashed lines mark their values obtained at threshold and solid lines at $P_{\text{em}} = 10P_{\text{sat}}$.

Seen from the upper left and right subplots of Fig. 11.3, the circular DFB and ring Bragg lasers still possess large discrimination between the modes even when operated in above-threshold regime (e.g., at $P_{\text{em}} = 10P_{\text{sat}}$), which ensures them a large single-mode range of at least 50–250. Additionally, we have identified low-pump ranges for their Mode 1 at $P_{\text{em}} = 10P_{\text{sat}}$, which are 100–160 for the circular DFB laser and 80–130 for the

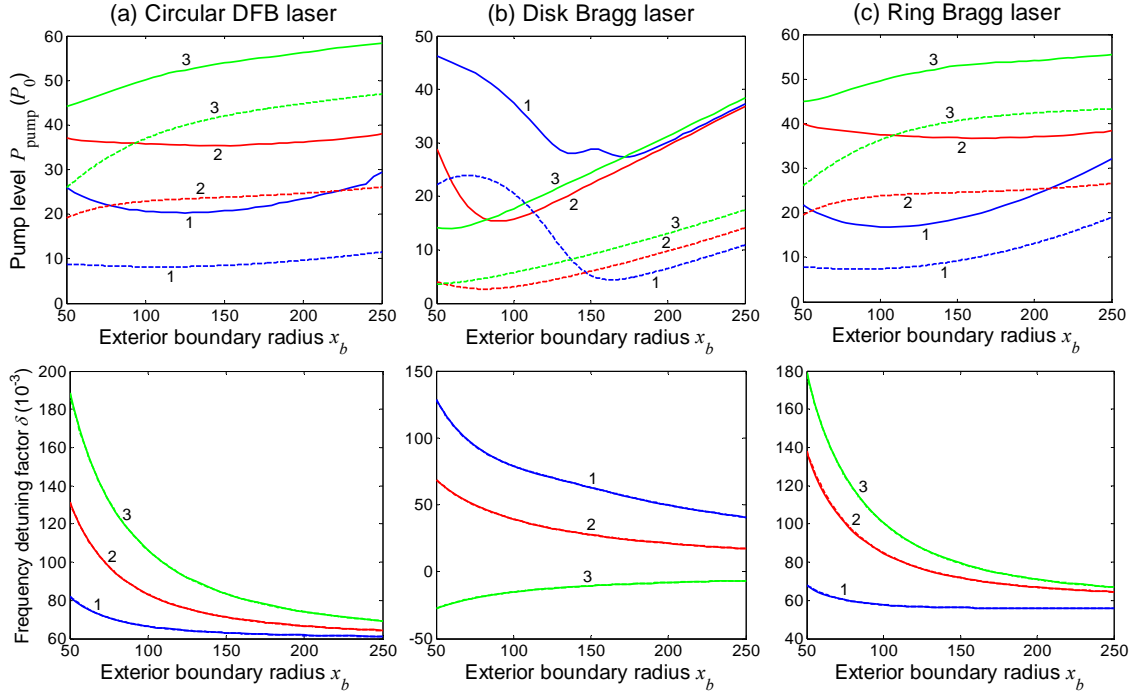


Fig. 11.3. Device-size-dependent pump level P_{pump} and frequency detuning factor δ of the 3 lowest-order modes, under uniform pump profile, of (a) circular DFB, (b) disk, and (c) ring Bragg lasers. x_b is the exterior boundary radius for all types of lasers. The inner disk radius x_0 of the disk Bragg laser is set to be $x_b/2$. The inner and outer edges of the annular defect of the ring Bragg laser are set to be $x_L = x_b/2 - \pi$ and $x_R = x_b/2 + \pi$, mark the values obtained at threshold and solid lines at $P_{\text{em}} = 10P_{\text{sat}}$.

ring Bragg laser. The low-pump range is another important factor in designing such lasers for high-efficiency, high-power applications. The existence of this low-pump range is a result of competition between the pumped area and the required gain level: although larger devices require a larger area to be pumped, their longer radial Bragg gratings reduce the needed gain because of stronger reflection of the optical fields from the gratings.

Seen from the upper middle subplot of Fig. 11.3, the P_{pump} for the disk Bragg laser exhibits interesting behaviors: (1) at $x_b = 200$, the order of Modes 1 and 2 exchanges from at threshold to above threshold due to the gain saturation effects; (2) the single-mode range (for Mode 2) shifts from 60–140 at threshold to 90–175 at high surface emission level $P_{\text{em}} = 10P_{\text{sat}}$. Therefore the single-mode range for designing the disk Bragg laser should be the overlap of these two ranges, i.e., 90–140.

Seen from the lower subplots of Fig. 11.3, all the laser modes have overlapped dashed and solid lines, which means their frequency detuning factors δ are unaffected by the surface emission level. This is because of δ being an intrinsic property of a laser mode.

Chapter 12

Conclusion and Outlook

We have described and analyzed a type of on-chip microlasers whose surface emission is very useful for many applications. The main advantage of these lasers would be the relative high (say, more than tens of milliwatts), single-mode optical power emitted broadside and coupled directly into a fiber or telescopic optics. Other areas of applications that can benefit from such lasers include ultrasensitive biochemical sensing [90], all-optical gyroscopes [91], and coherent beam combination [92] for high-power, high-radiance sources in communications and display technology. Furthermore, a thorough investigation of such lasers may also lead to a better understanding in designing and fabricating a nanosized analogue, if a surface-plasmon approach is employed.

We have studied the circular Bragg lasers for their applications as high-efficiency, high-power, surface-emitting lasers. We have covered the basic concepts, calculation methods, near- and above-threshold modal properties, and design strategies for such lasers.

Three typical configurations of such circular Bragg lasers—namely, circular DFB laser, disk Bragg laser, and ring Bragg laser are investigated. Following the grating design principle for linear DFB lasers, the gratings of circular Bragg lasers have to be in sync with the phases of optical waves in a circular (or cylindrical) geometry. Since the

eigensolutions of wave equation in a circular geometry are Hankel functions, this leads to a varying period of the gratings in radial direction, i.e., radially chirped gratings. To obtain efficient output coupling in vertical direction, a second-order scheme has been employed, and a quarter duty cycle has proven to be a good choice.

After a series of comparison of the modal properties, it becomes clear that disk and ring Bragg lasers have superiority over circular DFB lasers in high-efficiency surface emission. More specifically, disk Bragg lasers are most useful in low-threshold, ultracompact laser design while ring Bragg lasers are excellent candidates for high-power, large-area lasers.

Considering above-threshold operation with a nonuniform pump profile, it has been numerically demonstrated and theoretically explained that a larger overlap between the pump profile and modal intensity distribution leads to a lower threshold and a higher energy conversion efficiency. To achieve the same level of surface emission, disk Bragg laser still requires the lowest pump power, even though its single-mode range is modified because of the gain saturation induced mode transition. Circular DFB and ring Bragg lasers find their low-pump ranges at high surface emission level. These results provide us useful information for designing these lasers for single-mode, high-efficiency, high-power applications.

Looking ahead, there is still more work to be done on this special topic. For example, it would be interesting to further investigate how the grating design effects on the modal far-field pattern and what design results in a pattern having all, or almost all, of the energy located in the zeroth-order lobe with narrow divergence. This will be useful for applications that require highly directional, narrow-divergence laser beams. On the other hand, since the

above study is mainly theoretical analysis oriented, experimental work, of course, has to develop to verify the theoretical predictions. In the field of optoelectronics, a single-mode, high-power laser having controllable beam shape and being compatible with on-chip integration is still being highly sought. Due to the many salient features that have been described, it is our belief that the surface-emitting circular Bragg lasers will take the place of the prevailing VCSELs and make the ideal on-chip light source for next-generation optical communications and many other areas.

Appendix A

Derivation of Coupled Local Mode Equations

In this appendix we derive the coupled local mode equations for the optical modes in waveguides with index profile variation in the lightwave propagation direction. The derivation draws upon the analogy to the time-dependent perturbation theory in quantum mechanics. The results for both vector field and scalar field are in agreement with those derived from coupled local mode theory in standard textbooks [93].

A.1 Vector Field

In a linear, time-invariant medium, the vector electromagnetic field can be decomposed by time-harmonic modes

$$\begin{aligned}\vec{E}(\vec{r}, t) &= \vec{E}(\vec{r})e^{i\omega t} = (\vec{E}_t + \hat{z}E_z)e^{i\omega t}, \\ \vec{H}(\vec{r}, t) &= \vec{H}(\vec{r})e^{i\omega t} = (\vec{H}_t + \hat{z}H_z)e^{i\omega t}.\end{aligned}\tag{A.1}$$

Substituting (A.1) into the Maxwell equations,

$$\begin{aligned}\nabla \times \vec{E} &= -\mu\dot{\vec{H}}, \\ \nabla \times \vec{H} &= \varepsilon\dot{\vec{E}},\end{aligned}\tag{A.2}$$

yields

$$\nabla_t \times \hat{z} E_z + \partial_z \hat{z} \times \bar{E}_t = -i\omega\mu \bar{H}_t, \quad (\text{A.3})$$

$$\nabla_t \times \bar{E}_t = -i\omega\mu \hat{z} H_z, \quad (\text{A.4})$$

$$\nabla_t \times \hat{z} H_z + \partial_z \hat{z} \times \bar{H}_t = i\omega\varepsilon \bar{E}_t, \quad (\text{A.5})$$

$$\nabla_t \times \bar{H}_t = i\omega\varepsilon \hat{z} E_z. \quad (\text{A.6})$$

Insert (A.4) into (A.5), (A.6) into (A.3), it follows

$$i\partial_z \begin{pmatrix} 0 & -\hat{z} \times \\ \hat{z} \times & 0 \end{pmatrix} \begin{pmatrix} \bar{E}_t \\ \bar{H}_t \end{pmatrix} = \begin{pmatrix} \omega\varepsilon - \frac{1}{\omega} \nabla_t \times \frac{1}{\mu} \nabla_t \times & 0 \\ 0 & \omega\mu - \frac{1}{\omega} \nabla_t \times \frac{1}{\varepsilon} \nabla_t \times \end{pmatrix} \begin{pmatrix} \bar{E}_t \\ \bar{H}_t \end{pmatrix}. \quad (\text{A.7})$$

If we define

$$\hat{A} = \begin{pmatrix} \omega\varepsilon - \frac{1}{\omega} \nabla_t \times \frac{1}{\mu} \nabla_t \times & 0 \\ 0 & \omega\mu - \frac{1}{\omega} \nabla_t \times \frac{1}{\varepsilon} \nabla_t \times \end{pmatrix},$$

$$\hat{B} = \begin{pmatrix} 0 & -\hat{z} \times \\ \hat{z} \times & 0 \end{pmatrix},$$

$$\mathbb{F} = \begin{pmatrix} \bar{E}_t \\ \bar{H}_t \end{pmatrix},$$

(A.7) is expressible as

$$i\partial_z \hat{B} \mathbb{F} = \hat{A} \mathbb{F}. \quad (\text{A.8})$$

In the space of $\{\bar{E}_t, \bar{H}_t\}$, we define the inner product as

$$(\mathbb{F}, \mathbb{F}') \equiv \int_{A_\infty} dA \mathbb{F}^* \cdot \mathbb{F}' = \int_{A_\infty} dA \left(\bar{E}_t^* \cdot \bar{E}_t' + \bar{H}_t^* \cdot \bar{H}_t' \right), \quad (\text{A.9})$$

where the integral is over the infinite cross section A_∞ at a fixed z . It is easy to verify that under the above definition of inner product, \hat{A} and \hat{B} are both Hermitian as long as ε and μ are real.¹

If the nonuniformity of the waveguide along the propagation direction (z) varies slowly enough, then \mathbb{F} depends on z only through a phase factor $e^{-i\beta(z)z}$ where $\beta(z)$ depending on z is the “local propagation constant.” To the lowest order, we ignore the dependence of β on position z , then $i\partial_z \hat{B}\mathbb{F} = i\hat{B}\partial_z \mathbb{F} = i\hat{B}(-i\beta)\mathbb{F} = \beta\hat{B}\mathbb{F}$, resulting in

$$\hat{A}\mathbb{F} = \beta\hat{B}\mathbb{F}, \quad (\text{A.10})$$

which is a generalized Hermitian eigenproblem. Considering $\hat{B}\hat{B} = \mathbb{I}$, we get $\hat{B}\hat{A}\mathbb{F} = \beta\hat{B}\hat{B}\mathbb{F} = \beta\mathbb{F}$. Even though we can write $\hat{H}\mathbb{F} = \beta\mathbb{F}$ in form by defining $\hat{H} = \hat{B}\hat{A}$, \hat{H} is *not* Hermitian since \hat{A} and \hat{B} do not commute!

The orthogonality relation, which follows from the properties of Hermitian eigenproblems, is expressible as

$$\left(\mathbb{F}^{(i)}, \hat{B}\mathbb{F}^{(j)}\right) = \int_{A_\infty} dA \hat{z} \cdot \left(\bar{E}_t^{(i)*} \times \bar{H}_t^{(j)} + \bar{E}_t^{(j)} \times \bar{H}_t^{(i)*}\right) = 4P^{(i)}\delta_{ij}, \quad (\text{A.11})$$

¹ Proof: $\left(\mathbb{F}, \hat{B}\mathbb{F}'\right) \equiv \int_{A_\infty} dA \mathbb{F}^* \cdot \hat{B}\mathbb{F}' = \int_{A_\infty} dA \left[\bar{E}_t^* \cdot (-\hat{z}) \times \bar{H}' + \bar{H}_t^* \cdot \hat{z} \times \bar{E}'\right]$
 $= \int_{A_\infty} dA \left[(-\hat{z}) \times \bar{H}_t^* \cdot \bar{E}' + \hat{z} \times \bar{E}_t^* \cdot \bar{H}'\right] = \int_{A_\infty} dA \left(\hat{B}\mathbb{F}\right)^* \cdot \mathbb{F}' = \left(\hat{B}\mathbb{F}, \mathbb{F}'\right),$
 $\left(\bar{E}_t, \nabla_t \times \frac{1}{\mu} \nabla_t \times \bar{E}_t'\right) = \int_{A_\infty} dA \bar{E}_t^* \cdot \left(\nabla_t \times \frac{1}{\mu} \nabla_t \times \bar{E}_t'\right) = \int_{A_\infty} dA \left(\nabla_t \times \bar{E}_t\right)^* \cdot \frac{1}{\mu} \left(\nabla_t \times \bar{E}_t'\right)$
 $= \int_{A_\infty} dA \left(\nabla_t \times \frac{1}{\mu} \nabla_t \times \bar{E}_t\right)^* \cdot \bar{E}_t' = \left(\nabla_t \times \frac{1}{\mu} \nabla_t \times \bar{E}_t, \bar{E}_t'\right),$

where $\nabla \cdot (\bar{a} \times \bar{b}) = (\nabla \times \bar{a}) \cdot \bar{b} - \bar{a} \cdot (\nabla \times \bar{b})$ and $\nabla_t = \nabla_t^*$ have been used and a real μ has been assumed. Since \hat{A} is block diagonal, it is then obvious that $\left(\mathbb{F}, \hat{A}\mathbb{F}'\right) = \left(\hat{A}\mathbb{F}, \mathbb{F}'\right).$

where $P^{(i)}$ denotes the power carried in the i th mode. This orthogonality relation agrees with that derived from the Lorentz reciprocity theorem in electromagnetic theory.

So far we have shown that the time-harmonic Maxwell equation in a lossless (real ε and μ), time-invariant medium is analogous to the time-independent Schrödinger equation in quantum mechanics. By the famous adiabatic approximation, if the Hamiltonian \hat{H} (or \hat{A} , equivalently) varies very slowly along the propagation direction (z), we expect to be able to approximate the solutions of the Maxwell equations in the real configuration by means of “stationary” eigenfunctions of the local Hamiltonian, so that a particular eigenfunction at a z plane goes over continuously into the corresponding eigenfunction at a later z plane.

At each z plane, the bound solutions of the eigenvalue equation (A.10) are assumed to be known,

$$\hat{A}(z)f^{(n)}(z) = \beta_n(z)\hat{B}f^{(n)}(z), \quad (\text{A.12})$$

where $\beta_n(z)$ are real and the dependence of $f^{(n)}(z)$ on transverse coordinates is implicitly included. Suppose we know the field at $z = 0$ plane,

$$\mathbb{F}(z) = \sum_n a_n(z) f^{(n)}(z) \exp \left[-i \int_0^z \beta_n(z') dz' \right]. \quad (\text{A.13})$$

Substituting (A.13) into (A.8) and employing (A.12), in first-order approximation, yields

$$i\hat{B} \sum_n \left[\frac{da_n(z)}{dz} f^{(n)}(z) + a_n(z) \frac{\partial f^{(n)}(z)}{\partial z} \right] \exp \left[-i \int_0^z \beta_n(z') dz' \right] = 0. \quad (\text{A.14})$$

Multiply by $f^{(k)*}(z)$ and integrate over the infinite cross section A_∞ , using the orthogonality relation (A.11),

$$\frac{da_k(z)}{dz} = -\sum_n a_n(z) \frac{\left(f^{(k)}(z), \hat{B} \frac{\partial f^{(n)}(z)}{\partial z} \right)}{4P^{(k)}} \exp \left[-i \int_0^z (\beta_n(z') - \beta_k(z')) dz' \right]. \quad (\text{A.15})$$

Next we seek a doable expression for $\left(f^{(k)}(z), \hat{B} \frac{\partial f^{(n)}(z)}{\partial z} \right)$. Differentiate (A.12) with

respect to z ,

$$\frac{\partial \hat{A}(z)}{\partial z} f^{(n)}(z) + \hat{A}(z) \frac{\partial f^{(n)}(z)}{\partial z} = \frac{\partial \beta_n(z)}{\partial z} \hat{B} f^{(n)}(z) + \beta_n(z) \hat{B} \frac{\partial f^{(n)}(z)}{\partial z}. \quad (\text{A.16})$$

Multiply by $f^{(k)*}(z)$ ($k \neq n$) and integrate over the infinite cross section A_∞ ,

$$\left(f^{(k)}(z), \frac{\partial \hat{A}}{\partial z} f^{(n)}(z) \right) + \left(f^{(k)}(z), \hat{A} \frac{\partial f^{(n)}(z)}{\partial z} \right) = \beta_n(z) \left(f^{(k)}(z), \hat{B} \frac{\partial f^{(n)}(z)}{\partial z} \right), \quad (\text{A.17})$$

where

$$\begin{aligned} \left(f^{(k)}(z), \hat{A} \frac{\partial f^{(n)}(z)}{\partial z} \right) &= \left(\hat{A} f^{(k)}(z), \frac{\partial f^{(n)}(z)}{\partial z} \right) \\ &= \beta_k^*(z) \left(\hat{B} f^{(k)}(z), \frac{\partial f^{(n)}(z)}{\partial z} \right) = \beta_k(z) \left(f^{(k)}(z), \hat{B} \frac{\partial f^{(n)}(z)}{\partial z} \right). \end{aligned}$$

Therefore for $k \neq n$,

$$\left(f^{(k)}(z), \hat{B} \frac{\partial f^{(n)}(z)}{\partial z} \right) = \frac{\left(f^{(k)}(z), \frac{\partial \hat{A}}{\partial z} f^{(n)}(z) \right)}{\beta_n(z) - \beta_k(z)}.$$

For $k = n$, we can set it zero by choosing a proper phase of $f^{(k)}(z)$. The argument follows:

From (A.11),

$$\begin{aligned}
0 &= \frac{\partial}{\partial z} \left(f^{(k)}(z), \hat{B} f^{(k)}(z) \right) = \left(\frac{\partial f^{(k)}(z)}{\partial z}, \hat{B} f^{(k)}(z) \right) + \left(f^{(k)}(z), \hat{B} \frac{\partial f^{(k)}(z)}{\partial z} \right) \\
&= \left(f^{(k)}(z), \hat{B} \frac{\partial f^{(k)}(z)}{\partial z} \right)^* + \left(f^{(k)}(z), \hat{B} \frac{\partial f^{(k)}(z)}{\partial z} \right),
\end{aligned}$$

which means $\left(f^{(k)}(z), \hat{B} \frac{\partial f^{(k)}(z)}{\partial z} \right)$ must be pure imaginary.

Let $\left(f^{(k)}(z), \hat{B} \frac{\partial f^{(k)}(z)}{\partial z} \right) = i\alpha(z)$, we can change the phase of $f^{(k)}(z)$ by an amount of $\gamma(z)$

such that $f^{(k)'}(z) = f^{(k)}(z)e^{i\gamma(z)}$, so

$$\begin{aligned}
\left(f^{(k)'}(z), \hat{B} \frac{\partial f^{(k)'}(z)}{\partial z} \right) &= \left(f^{(k)}(z)e^{i\gamma}, \hat{B} \frac{\partial f^{(k)}(z)}{\partial z} e^{i\gamma} \right) \\
&\quad + \left(f^{(k)}(z)e^{i\gamma}, \hat{B} f^{(k)}(z)e^{i\gamma} \right) i \frac{d\gamma}{dz} = i\alpha(z) + 4P^{(k)} i \frac{d\gamma}{dz}.
\end{aligned}$$

We are free to choose $\gamma(z)$ such that $\frac{d\gamma}{dz} = -\frac{\alpha(z)}{4P^{(k)}}$ to make $\left(f^{(k)'}(z), \hat{B} \frac{\partial f^{(k)'}(z)}{\partial z} \right) = 0$.

Since $f^{(k)}(z)$ and $f^{(k)}(z)e^{i\gamma(z)}$ denote the same eigenstate, we proved that

$\left(f^{(k)}(z), \hat{B} \frac{\partial f^{(k)}(z)}{\partial z} \right)$ can be set zero.

Furthermore, from the definition of \hat{A} , we have

$$\begin{aligned}
\frac{\partial \hat{A}}{\partial z} &= \begin{pmatrix} \omega \frac{\partial \varepsilon}{\partial z} + \frac{1}{\omega} \nabla_t \times \frac{1}{\mu^2} \frac{\partial \mu}{\partial z} \nabla_t \times & 0 \\ 0 & \omega \frac{\partial \mu}{\partial z} + \frac{1}{\omega} \nabla_t \times \frac{1}{\varepsilon^2} \frac{\partial \varepsilon}{\partial z} \nabla_t \times \end{pmatrix} \\
&= \begin{pmatrix} \omega \frac{\partial \varepsilon}{\partial z} & 0 \\ 0 & 0 \end{pmatrix} + \begin{pmatrix} 0 & 0 \\ 0 & \omega \frac{\partial \mu}{\partial z} \end{pmatrix} + \begin{pmatrix} \frac{1}{\omega} \nabla_t \times \frac{1}{\mu^2} \frac{\partial \mu}{\partial z} \nabla_t \times & 0 \\ 0 & 0 \end{pmatrix} + \begin{pmatrix} 0 & 0 \\ 0 & \frac{1}{\omega} \nabla_t \times \frac{1}{\varepsilon^2} \frac{\partial \varepsilon}{\partial z} \nabla_t \times \end{pmatrix}.
\end{aligned} \tag{A.18}$$

It is obvious from the definition of inner product that

$$\begin{aligned}
\left(\bar{e}_t^{(k)}, \nabla_t \times \frac{1}{\mu^2} \nabla_t \times \bar{e}_t^{(n)}\right) &= \int_{A_\infty} dA \bar{e}_t^{(k)*} \cdot \left(\nabla_t \times \frac{1}{\mu^2} \nabla_t \times \bar{e}_t^{(n)}\right) = \int_{A_\infty} dA \left(\nabla_t \times \bar{e}_t^{(k)}\right)^* \cdot \frac{1}{\mu^2} \left(\nabla_t \times \bar{e}_t^{(n)}\right) \\
&= \int_{A_\infty} dA \left(-i\omega\mu\hat{z}h_z^{(k)}\right)^* \cdot \frac{1}{\mu^2} \left(-i\omega\mu\hat{z}h_z^{(n)}\right) = \omega^2 \int_{A_\infty} dA \left(\hat{z}h_z^{(k)}\right)^* \cdot \left(\hat{z}h_z^{(n)}\right) = \omega^2 \left(\hat{z}h_z^{(k)}, \hat{z}h_z^{(n)}\right).
\end{aligned}$$

Likewise, $\left(\bar{h}_t^{(k)}, \nabla_t \times \frac{1}{\varepsilon^2} \nabla_t \times \bar{h}_t^{(n)}\right) = \omega^2 \left(\hat{z}e_z^{(k)}, \hat{z}e_z^{(n)}\right).$

As a result, $\left(f^{(k)}(z), \frac{\partial \hat{A}}{\partial z} f^{(n)}(z)\right) = \omega \int_{A_\infty} dA \left[\frac{\partial \varepsilon}{\partial z} \bar{e}^{(k)*} \cdot \bar{e}^{(n)} + \frac{\partial \mu}{\partial z} \bar{h}^{(k)*} \cdot \bar{h}^{(n)} \right],$

where $\bar{e}^{(i)} = \bar{e}_t^{(i)} + \hat{z}e_z^{(i)}$, $\bar{h}^{(i)} = \bar{h}_t^{(i)} + \hat{z}h_z^{(i)}$.

Now we get

$$\left(f^{(k)}(z), \hat{B} \frac{\partial f^{(n)}(z)}{\partial z}\right) = \frac{\omega \int_{A_\infty} dA \left[\frac{\partial \varepsilon}{\partial z} \bar{e}^{(k)*} \cdot \bar{e}^{(n)} + \frac{\partial \mu}{\partial z} \bar{h}^{(k)*} \cdot \bar{h}^{(n)} \right]}{\beta_n(z) - \beta_k(z)}. \quad (\text{A.19})$$

Inserting (A.19) into (A.15) leads to the coupled local mode equation,

$$\frac{da_k(z)}{dz} = - \sum_{n \neq k} a_n(z) \mathbb{C}_{kn}(z) \exp \left[-i \int_0^z (\beta_n(z') - \beta_k(z')) dz' \right], \quad (\text{A.20})$$

where $\mathbb{C}_{kn}(z) = \frac{\omega \int_{A_\infty} dA \left[\frac{\partial \varepsilon}{\partial z} \bar{e}^{(k)*} \cdot \bar{e}^{(n)} + \frac{\partial \mu}{\partial z} \bar{h}^{(k)*} \cdot \bar{h}^{(n)} \right]}{4P^{(k)} [\beta_n(z) - \beta_k(z)]}.$

In dielectric materials, $\mu = \mu_0$, $\varepsilon = \varepsilon_0 n^2$, $\frac{\partial \mu}{\partial z} = 0$, $\frac{\partial \varepsilon}{\partial z} = \varepsilon_0 \frac{\partial n^2}{\partial z}$, and if \bar{e} and \bar{h} are

power normalized, i.e., $P^{(k)} = 1$,

$$\mathbb{C}_{kn}(z) = \frac{k}{4} \left(\frac{\varepsilon_0}{\mu_0} \right)^{\frac{1}{2}} \frac{1}{\beta_n(z) - \beta_k(z)} \int_{A_\infty} dA \bar{e}^{(k)*} \cdot \bar{e}^{(n)} \frac{\partial n^2}{\partial z}. \quad (\text{A.21})$$

We arrive at the same result as that derived from the first-order vectorial coupled local mode theory [93].

A.2 Scalar Field

In the case that the polarization effects due to the waveguide structure are unimportant, we can introduce the “weak guidance approximation,” under which the local modal fields $\bar{e} \simeq \bar{e}_t$, $\bar{h} \simeq \bar{h}_t$, and the Cartesian components of \bar{e}_t are approximated by the solutions of the scalar wave equation,

$$\bar{E}(x, y, z) = \bar{e}(x, y)e^{-i\beta z} \simeq \bar{e}_t(x, y)e^{-i\beta z} = (\hat{x}e_x(x, y) + \hat{y}e_y(x, y))e^{-i\beta z}.$$

Let Ψ denote $e_x(x, y)$ or $e_y(x, y)$, then Ψ satisfies the scalar wave equation,

$$\left[\nabla_t^2 + k^2 n^2(x, y, z) \right] \Psi = \beta^2(z) \Psi. \quad (\text{A.22})$$

In the space of $\{\Psi\}$, the inner product is defined as $(\Psi, \Psi') \equiv \int_{A_\infty} dA \Psi^* \Psi'$. It is obvious

that under this definition, the operator $\hat{H}(z) \equiv \nabla_t^2 + k^2 n^2(x, y, z)$ is Hermitian, and positive definite. Therefore (A.22) is a typical Hermitian eigenvalue problem.

The orthogonality relation is thus

$$\begin{aligned} (\Psi^{(i)}, \Psi^{(j)}) &\equiv \int_{A_\infty} dA \Psi^{(i)*} \Psi^{(j)} = \int_{A_\infty} dA \bar{e}_t^{(i)*} \cdot \bar{e}_t^{(j)} = \int_{A_\infty} dA \bar{e}_t^{(i)*} \cdot \left[-\hat{z} \times \bar{h}_t^{(j)} \left(\frac{\mu_0}{\varepsilon_0} \right)^{\frac{1}{2}} \frac{k}{\beta_j} \right] \\ &= \left(\frac{\mu_0}{\varepsilon_0} \right)^{\frac{1}{2}} \frac{k}{\beta_j} \int_{A_\infty} dA \hat{z} \cdot [\bar{e}_t^{(i)*} \times \bar{h}_t^{(j)}] = \left(\frac{\mu_0}{\varepsilon_0} \right)^{\frac{1}{2}} \frac{k}{\beta_j} \int_{A_\infty} dA \hat{z} \cdot [\bar{e}^{(i)*} \times \bar{h}^{(j)}] = 2 \left(\frac{\mu_0}{\varepsilon_0} \right)^{\frac{1}{2}} \frac{k}{\beta_i} P^{(i)} \delta_{ij}, \end{aligned} \quad (\text{A.23})$$

where we have used $\bar{h}_t = \left(\frac{\varepsilon_0}{\mu_0} \right)^{\frac{1}{2}} \frac{\beta}{k} \hat{z} \times \bar{e}_t$ under the weak guidance approximation.

Let us follow the standard time independent perturbation theory. Assuming at some z plane, we have found a set of eigenstates $\{\Psi_n(z)\}$ satisfying (A.22),

$$\hat{H}(z)\Psi^{(n)}(z) = \beta_n^2(z)\Psi^{(n)}(z), \quad (\text{A.24})$$

we need the new set of eigenwave functions at $z + dz$ plane. We may write

$$\begin{aligned} \beta_n^2(z + dz) &= \beta_n^2(z) + dz\partial_z\beta_n^2, \\ \Psi^{(n)}(z + dz) &= \Psi^{(n)}(z) + dz\partial_z\Psi^{(n)}, \\ \hat{H}(z + dz) &= \hat{H}(z) + dz\partial_z\hat{H}. \end{aligned} \quad (\text{A.25})$$

Substituting them into $\hat{H}(z + dz)\Psi^{(n)}(z + dz) = \beta_n^2(z + dz)\Psi^{(n)}(z + dz)$ then equating the coefficients of term dz leads to

$$\hat{H}(z)\partial_z\Psi^{(n)} + (\partial_z\hat{H})\Psi^{(n)}(z) = \beta_n^2(z)\partial_z\Psi^{(n)} + (\partial_z\beta_n^2)\Psi^{(n)}(z). \quad (\text{A.26})$$

Generally, we may well assume $\partial_z\Psi^{(n)} = \sum_j \mathbb{C}_{nj}(z)\Psi^{(j)}(z)$ and introduce (A.24) into

(A.26),

$$\sum_j \mathbb{C}_{nj}(z)\beta_j^2(z)\Psi^{(j)}(z) + (\partial_z\hat{H})\Psi^{(n)}(z) = \beta_n^2(z)\sum_j \mathbb{C}_{nj}(z)\Psi^{(j)}(z) + (\partial_z\beta_n^2)\Psi^{(n)}(z). \quad (\text{A.27})$$

Multiply by $\Psi^{(k)*}(z)$ then integrate over the infinite cross section A_∞ , then

$$\begin{aligned} \mathbb{C}_{nk}(z)\beta_k^2(z) \cdot 2\left(\frac{\mu_0}{\varepsilon_0}\right)^{\frac{1}{2}} \frac{k}{\beta_k} P^{(k)} + (\Psi^{(k)}(z), (\partial_z\hat{H})\Psi^{(n)}(z)) \\ = \beta_n^2(z)\mathbb{C}_{nk}(z) \cdot 2\left(\frac{\mu_0}{\varepsilon_0}\right)^{\frac{1}{2}} \frac{k}{\beta_k} P^{(k)} + (\partial_z\beta_n^2) \cdot 2\left(\frac{\mu_0}{\varepsilon_0}\right)^{\frac{1}{2}} \frac{k}{\beta_k} P^{(k)} \delta_{kn}. \end{aligned} \quad (\text{A.28})$$

For $k \neq n$,

$$\mathbb{C}_{nk}(z) = \frac{(\Psi^{(k)}(z), (\partial_z\hat{H})\Psi^{(n)}(z))}{2\left(\frac{\mu_0}{\varepsilon_0}\right)^{\frac{1}{2}} \frac{k}{\beta_k} P^{(k)} [\beta_n^2(z) - \beta_k^2(z)]}. \quad (\text{A.29})$$

By the same argument as in Section A.1 we can set $\mathbb{C}_{nn}(z) = 0$.

Recall $\hat{H}(z) \equiv \nabla_t^2 + k^2 n^2(x, y, z)$, $\partial_z \hat{H} = k^2 \frac{\partial n^2}{\partial z}$, therefore

$$\mathbb{C}_{nk}(z) = \frac{k^2}{\beta_n^2(z) - \beta_k^2(z)} \cdot \frac{\left(\Psi^{(k)}(z), \frac{\partial n^2}{\partial z} \Psi^{(n)}(z) \right)}{2 \left(\frac{\mu_0}{\varepsilon_0} \right)^{\frac{1}{2}} \frac{k}{\beta_k} P^{(k)}}.$$

If $\Psi^{(k)}(z)$ and $\Psi^{(n)}(z)$ are power normalized, i.e.,

$$\begin{aligned} \left(\Psi^{(k)}, \Psi^{(k)} \right) &= 2 \left(\frac{\mu_0}{\varepsilon_0} \right)^{\frac{1}{2}} \frac{k}{\beta_k} P^{(k)} = 1, \\ \left(\Psi^{(n)}, \Psi^{(n)} \right) &= 2 \left(\frac{\mu_0}{\varepsilon_0} \right)^{\frac{1}{2}} \frac{k}{\beta_n} P^{(n)} = 1, \end{aligned}$$

by requiring $P^{(k)} = P^{(n)}$ and assuming $\beta_k \simeq \beta_n$ under weak guidance approximation, we get

$$\mathbb{C}_{nk}(z) = \frac{k^2}{\beta_n^2(z) - \beta_k^2(z)} \left(\Psi^{(k)}(z), \frac{\partial n^2}{\partial z} \Psi^{(n)}(z) \right). \quad (\text{A.30})$$

Being dependent on z , the wave function is generally expanded as

$$\Phi(z) = \sum_n a_n(z) \Psi^{(n)}(z) \exp \left[-i \int_0^z \beta_n(z') dz' \right]. \quad (\text{A.31})$$

After $\Phi(z)$ propagates a small distance of dz ,

$$\begin{aligned} \Phi(z + dz) &= \sum_n (a_n(z) + da_n) \Psi^{(n)}(z + dz) \exp \left[-i \int_0^{z+dz} \beta_n(z') dz' \right] \\ &= \sum_n \left\{ a_n(z) \Psi^{(n)}(z) \exp \left[-i \int_0^z \beta_n(z') dz' \right] + dz \sum_{k \neq n} \mathbb{C}_{nk}(z) a_k(z) \Psi^{(k)}(z) \exp \left[-i \int_0^z \beta_k(z') dz' \right] \right\}, \end{aligned} \quad (\text{A.32})$$

we arrive at

$$\frac{da_n(z)}{dz} = \sum_{k \neq n} a_k(z) \mathbb{C}_{nk}(z) \exp \left[-i \int_0^z (\beta_k(z') - \beta_n(z')) dz' \right], \quad (\text{A.33})$$

which is exactly the same as that from the scalar coupled local mode theory [93].

Appendix B

Calculation of the Green's Function

In this appendix we present the detailed procedure of calculating the numerical Green's function $G(z, z')$ for a given wafer layer structure $n(z)$.

Assuming a refractive index profile of layer structure

$$\varepsilon_r(z) = n^2(z) = \begin{cases} n_l^2 & \text{region } i \ (-\infty < z < z_1), \\ n_1^2 & \text{region } ii \ (z_1 < z < z_2), \\ n_2^2 & \text{region } iii \ (z_2 < z < z_3), \\ n_u^2 & \text{region } iv \ (z_3 < z < +\infty), \end{cases} \quad (\text{B.1})$$

we want to obtain the Green's Function $G(z, z')$ that satisfies

$$\left(k_0^2 \varepsilon_r(z) + \frac{\partial^2}{\partial z^2} \right) G(z, z') = \delta(z - z'), \quad (\text{B.2})$$

with z' located in region *iii* ($z_2 < z' < z_3$). The Green's function for $-\infty < z' < +\infty$ has to be obtained piecewise according to different locations of z' . Using the same recipe, the $G(z, z')$ with z' in other regions can also be obtained.

In different z regions, Eq. (B.2) takes different forms: (Recall in the open regions *i* and *iv*, $G(z, z')$ has to take the form of outward propagating plane waves.)

$$\text{region } i \ (-\infty < z < z_1): \quad k_0^2 n_l^2 G_i + \ddot{G}_i = 0 \Rightarrow G_i = A_i(z') \cos(k_0 n_l z) - i A_i(z') \sin(k_0 n_l z);$$

region ii ($z_1 < z < z_2$): $k_0^2 n_1^2 G_{ii} + \ddot{G}_{ii} = 0 \Rightarrow G_{ii} = A_{ii}(z') \cos(k_0 n_1 z) + B_{ii}(z') \sin(k_0 n_1 z)$;

region iii ($z_2 < z < z_3$): $k_0^2 n_2^2 G_{iii} + \ddot{G}_{iii} = \delta(z - z') \Rightarrow$

$$G_{iii} = \begin{cases} A_{iii}(z') \cos(k_0 n_2 z) + B_{iii}(z') \sin(k_0 n_2 z), & z_2 < z < z', \\ A'_{iii}(z') \cos(k_0 n_2 z) + B'_{iii}(z') \sin(k_0 n_2 z), & z' < z < z_3; \end{cases}$$

region iv ($z_3 < z < +\infty$): $k_0^2 n_u^2 G_{iv} + \ddot{G}_{iv} = 0 \Rightarrow G_{iv} = A_{iv}(z') \cos(k_0 n_u z) + iA_{iv}(z') \sin(k_0 n_u z)$.

The remaining boundary conditions are

$$(1) \quad G_i(z_1, z') = G_{ii}(z_1, z'),$$

$$A_i \cos(k_0 n_l z_1) - iA_i \sin(k_0 n_l z_1) = A_{ii} \cos(k_0 n_1 z_1) + B_{ii} \sin(k_0 n_1 z_1);$$

$$(2) \quad \dot{G}_i(z_1, z') = \dot{G}_{ii}(z_1, z'),$$

$$-A_i n_l \sin(k_0 n_l z_1) - iA_i n_l \cos(k_0 n_l z_1) = -A_{ii} n_1 \sin(k_0 n_1 z_1) + B_{ii} n_1 \cos(k_0 n_1 z_1);$$

$$(3) \quad G_{ii}(z_2, z') = G_{iii}(z_2, z'),$$

$$A_{ii} \cos(k_0 n_1 z_2) + B_{ii} \sin(k_0 n_1 z_2) = A_{iii} \cos(k_0 n_2 z_2) + B_{iii} \sin(k_0 n_2 z_2);$$

$$(4) \quad \dot{G}_{ii}(z_2, z') = \dot{G}_{iii}(z_2, z'),$$

$$-A_{ii} n_1 \sin(k_0 n_1 z_2) + B_{ii} n_1 \cos(k_0 n_1 z_2) = -A_{iii} n_2 \sin(k_0 n_2 z_2) + B_{iii} n_2 \cos(k_0 n_2 z_2);$$

$$(5) \quad G_{iii}(z' -, z') = G_{ii}(z' +, z'),$$

$$A_{iii} \cos(k_0 n_2 z') + B_{iii} \sin(k_0 n_2 z') = A'_{iii} \cos(k_0 n_2 z') + B'_{iii} \sin(k_0 n_2 z');$$

$$(6) \quad \dot{G}_{iii}(z' -, z') = \dot{G}_{iii}(z' +, z') - 1,$$

$$-A_{iii} k_0 n_2 \sin(k_0 n_2 z') + B_{iii} k_0 n_2 \cos(k_0 n_2 z') = -A'_{iii} k_0 n_2 \sin(k_0 n_2 z') + B'_{iii} k_0 n_2 \cos(k_0 n_2 z') - 1;$$

$$(7) \quad G_{iii}(z_3, z') = G_{iv}(z_3, z'),$$

$$A'_{iii} \cos(k_0 n_2 z_3) + B'_{iii} \sin(k_0 n_2 z_3) = A_{iv} \cos(k_0 n_u z_3) + iA_{iv} \sin(k_0 n_u z_3);$$

$$(8) \quad \dot{G}_{iii}(z_3, z') = \dot{G}_{iv}(z_3, z'),$$

$$-A'_{iii}n_2 \sin(k_0 n_2 z_3) + B'_{iii}n_2 \cos(k_0 n_2 z_3) = -A_{iv}n_u \sin(k_0 n_u z_3) + iA_{iv}n_u \cos(k_0 n_u z_3).$$

Technically, the coefficients $A_i, A_{ii}, B_{ii}, A_{iii}, B_{iii}, A'_{iii}, B'_{iii}, A_{iv}$ (note they also depend on z') can be solved by rewriting the above 8 equations

$$\begin{cases} A_i [\cos(k_0 n_l z_1) - i \sin(k_0 n_l z_1)] - A_{ii} \cos(k_0 n_l z_1) - B_{ii} \sin(k_0 n_l z_1) = 0, \\ A_i [-n_l \sin(k_0 n_l z_1) - i n_l \cos(k_0 n_l z_1)] + A_{ii} n_l \sin(k_0 n_l z_1) - B_{ii} n_l \cos(k_0 n_l z_1) = 0, \\ A_{ii} \cos(k_0 n_1 z_2) + B_{ii} \sin(k_0 n_1 z_2) - A_{iii} \cos(k_0 n_2 z_2) - B_{iii} \sin(k_0 n_2 z_2) = 0, \\ -A_{ii} n_1 \sin(k_0 n_1 z_2) + B_{ii} n_1 \cos(k_0 n_1 z_2) + A_{iii} n_2 \sin(k_0 n_2 z_2) - B_{iii} n_2 \cos(k_0 n_2 z_2) = 0, \\ A_{iii} \cos(k_0 n_2 z') + B_{iii} \sin(k_0 n_2 z') - A'_{iii} \cos(k_0 n_2 z') - B'_{iii} \sin(k_0 n_2 z') = 0, \\ -A_{iii} n_2 \sin(k_0 n_2 z') + B_{iii} n_2 \cos(k_0 n_2 z') + A'_{iii} n_2 \sin(k_0 n_2 z') - B'_{iii} n_2 \cos(k_0 n_2 z') = -\frac{1}{k_0}, \\ A'_{iii} \cos(k_0 n_2 z_3) + B'_{iii} \sin(k_0 n_2 z_3) - A_{iv} [\cos(k_0 n_u z_3) + i \sin(k_0 n_u z_3)] = 0, \\ -A'_{iii} n_2 \sin(k_0 n_2 z_3) + B'_{iii} n_2 \cos(k_0 n_2 z_3) + A_{iv} [n_u \sin(k_0 n_u z_3) - i n_u \cos(k_0 n_u z_3)] = 0, \end{cases}$$

in matrix form

$$\begin{pmatrix} M_{11} & M_{12} \\ M_{21} & M_{22} \end{pmatrix} \begin{pmatrix} A_i \\ A_{ii} \\ B_{ii} \\ A_{iii} \\ B_{iii} \\ A'_{iii} \\ B'_{iii} \\ A_{iv} \end{pmatrix} = \begin{pmatrix} 0 \\ 0 \\ 0 \\ 0 \\ 0 \\ -\frac{1}{k_0} \\ 0 \\ 0 \end{pmatrix}, \quad (\text{B.3})$$

where

$$M_{11} = \begin{pmatrix} \exp(-ik_0 n_l z_1) & -\cos(k_0 n_l z_1) & -\sin(k_0 n_l z_1) & 0 \\ -in_l \exp(-ik_0 n_l z_1) & n_l \sin(k_0 n_l z_1) & -n_l \cos(k_0 n_l z_1) & 0 \\ 0 & \cos(k_0 n_1 z_2) & \sin(k_0 n_1 z_2) & -\cos(k_0 n_2 z_2) \\ 0 & -n_1 \sin(k_0 n_1 z_2) & n_1 \cos(k_0 n_1 z_2) & n_2 \sin(k_0 n_2 z_2) \end{pmatrix},$$

$$M_{12} = \begin{pmatrix} 0 & 0 & 0 & 0 \\ 0 & 0 & 0 & 0 \\ -\sin(k_0 n_2 z_2) & 0 & 0 & 0 \\ -n_2 \cos(k_0 n_2 z_2) & 0 & 0 & 0 \end{pmatrix},$$

$$M_{21} = \begin{pmatrix} 0 & 0 & 0 & \cos(k_0 n_2 z') \\ 0 & 0 & 0 & -n_2 \sin(k_0 n_2 z') \\ 0 & 0 & 0 & 0 \\ 0 & 0 & 0 & 0 \end{pmatrix},$$

$$\text{and } M_{22} = \begin{pmatrix} \sin(k_0 n_2 z') & -\cos(k_0 n_2 z') & -\sin(k_0 n_2 z') & 0 \\ n_2 \cos(k_0 n_2 z') & n_2 \sin(k_0 n_2 z') & -n_2 \cos(k_0 n_2 z') & 0 \\ 0 & \cos(k_0 n_2 z_3) & \sin(k_0 n_2 z_3) & -\exp(ik_0 n_u z_3) \\ 0 & -n_2 \sin(k_0 n_2 z_3) & n_2 \cos(k_0 n_2 z_3) & -in_u \exp(ik_0 n_u z_3) \end{pmatrix}.$$

The coefficients array $[A_i \ A_{ii} \ B_{ii} \ A_{iii} \ B_{iii} \ A'_{iii} \ B'_{iii} \ A_{iv}]^T$ can easily be solved by matrix manipulations of (B.3). Then we get $G(z, z')$ with $-\infty < z < +\infty$ and $z_2 < z' < z_3$. Using the same recipe, the $G(z, z')$ with z' in other regions can also be obtained. With the z' regions stitched together, the Green's function for $-\infty < z' < +\infty$ is then obtained.

Bibliography

1. B. Jalali, "Teaching silicon new tricks," *Nat. Photonics* **1**, 193–195 (2007).
2. H. Kroemer, T. Y. Liu, and P. M. Petroff, "GaAs on Si and related systems: problems and prospects," *J. Cryst. Growth* **95**, 96–102 (1989).
3. O. Boyraz and B. Jalali, "Demonstration of a silicon Raman laser," *Opt. Express* **12**, 5269–5273 (2004).
4. S. Lombardo, S. U. Campisano, G. N. van den Hoven, A. Cacciato, and A. Polman, "Room-temperature luminescence from Er-implanted semi-insulating polycrystalline silicon," *Appl. Phys. Lett.* **63**, 1942–1944 (1993).
5. L. Pavesi, L. Dal Negro, C. Mazzoleni, G. Franzo, and F. Priolo, "Optical gain in silicon nanocrystals," *Nature* **408**, 440–444 (2000).
6. S. J. Pearton, C. R. Abernathy, and F. Ren, *Topics in Growth and Device Processing of III-V Semiconductors*, International Series on Advances in Solid State Electronics and Technology (World Scientific, 1996).
7. B. Kunert, A. Klehr, S. Reinhard, K. Volz, and W. Stolz, "Near room temperature electrical injection lasing for dilute nitride Ga(NAsP)/GaP quantum-well structures grown by metal organic vapour phase epitaxy," *Electron. Lett.* **42**, 601–603 (2006).
8. B. Kunert, S. Zinnkann, I. Németh, G. Lukin, R. Fritz, K. Volz, W. Stolz, C. Lange, N. S. Koester, D. J. Franzbach, S. Chatterjee, W. W. Rühle, N. C. Gerhardt, and M. R. Hofmann, "Lasing of lattice-matched Ga(NAsP) quantum well heterostructures

monolithically integrated on (001) Si substrate," in *SPIE Photonics West 2009*, (San Jose, CA, USA, 2009), pp. 7220-26.

9. J. F. Liu, X. C. Sun, L. C. Kimerling, and J. Michel, "Direct-gap optical gain of Ge on Si at room temperature," *Opt. Lett.* **34**, 1738–1740 (2009).
10. X. C. Sun, J. F. Liu, L. C. Kimerling, and J. Michel, "Direct gap photoluminescence of *n*-type tensile-strained Ge-on-Si," *Appl. Phys. Lett.* **95**, 011911 (2009).
11. J. F. Liu, X. C. Sun, R. Camacho-Aguilera, L. C. Kimerling, and J. Michel, "Ge-on-Si laser operating at room temperature," *Opt. Lett.* **35**, 679–681 (2010).
12. C. G. Fonstad, J. J. Rumpler, E. R. Barkley, J. M. Perkins, and S. Famenini, "Recess integration of micro-cleaved laser diode platelets with dielectric waveguides on silicon," *Proc. SPIE* **6909**, 69090O (2008).
13. G. Roelkens, D. Van Thourhout, R. Baets, R. Notzel, and M. Smit, "Laser emission and photodetection in an InP/InGaAsP layer integrated on and coupled to a Silicon-on-Insulator waveguide circuit," *Opt. Express* **14**, 8154–8159 (2006).
14. J. Van Campenhout, P. Rojo-Romeo, P. Regreny, C. Seassal, D. Van Thourhout, S. Verstuyft, L. Di Cioccio, J. M. Fedeli, C. Lagahe, and R. Baets, "Electrically pumped InP-based microdisk lasers integrated with a nanophotonic silicon-on-insulator waveguide circuit," *Opt. Express* **15**, 6744–6749 (2007).
15. A. Berthold, B. Jakoby, and M. J. Vellekoop, "Wafer-to-wafer fusion bonding of oxidized silicon to silicon at low temperatures," *Sens. Actuator A* **68**, 410–413 (1998).
16. G. Krauter, A. Schumacher, U. Gosele, T. Jaworek, and G. Wegner, "Room temperature silicon wafer bonding with ultra-thin polymer films," *Adv. Mater.* **9**, 417–420 (1997).

17. H. Takagi, K. Kikuchi, R. Maeda, T. R. Chung, and T. Suga, "Surface activated bonding of silicon wafers at room temperature," *Appl. Phys. Lett.* **68**, 2222–2224 (1996).
18. H. Huang, X. M. Ren, W. J. Wang, H. L. Song, Q. Wang, S. W. Cai, and Y. Q. Huang, "Low temperature InP/Si wafer bonding using boride treated surface," *Appl. Phys. Lett.* **90**, 161102 (2007).
19. D. Pasquariello and K. Hjort, "Plasma-assisted InP-to-Si low temperature wafer bonding," *IEEE J. Sel. Top. Quantum Electron.* **8**, 118–131 (2002).
20. A. W. Fang, H. Park, O. Cohen, R. Jones, M. J. Paniccia, and J. E. Bowers, "Electrically pumped hybrid AlGaInAs-silicon evanescent laser," *Opt. Express* **14**, 9203–9210 (2006).
21. A. W. Fang, R. Jones, H. Park, O. Cohen, O. Raday, M. J. Paniccia, and J. E. Bowers, "Integrated AlGaInAs-silicon evanescent racetrack laser and photodetector," *Opt. Express* **15**, 2315–2322 (2007).
22. A. W. Fang, E. Lively, Y. H. Kuo, D. Liang, and J. E. Bowers, "A distributed feedback silicon evanescent laser," *Opt. Express* **16**, 4413–4419 (2008).
23. E. Kapon, J. Katz, and A. Yariv, "Supermode analysis of phase-locked arrays of semiconductor lasers," *Opt. Lett.* **9**, 125–127 (1984).
24. A. Yariv, *Optical Electronics in Modern Communications*, 5th ed. (Oxford Univ. Press, New York, 1997), pp. 526–531.
25. A. Yariv and X. K. Sun, "Supermode Si/III-V hybrid lasers, optical amplifiers and modulators: a proposal and analysis," *Opt. Express* **15**, 9147–9151 (2007).

26. X. K. Sun and A. Yariv, "Engineering supermode silicon/III–V hybrid waveguides for laser oscillation," *J. Opt. Soc. Am. B* **25**, 923–926 (2008).
27. X. K. Sun and A. Yariv, "Supermode control in integrated hybrid Si/III–V optoelectronic circuits for modal gain enhancement," in *The 8th Pacific Rim Conference on Lasers and Electro-Optics (CLEO/Pacific Rim 2009)*, (IEEE, Shanghai, China, 2009), pp. WD4-5.
28. X. K. Sun, H. C. Liu, and A. Yariv, "Adiabaticity criterion and the shortest adiabatic mode transformer in a coupled-waveguide system," *Opt. Lett.* **34**, 280–282 (2009).
29. D. Marcuse, "Mode conversion in optical fibers with monotonically increasing core radius," *J. Lightwave Technol.* **5**, 125–133 (1987).
30. J. D. Love, W. M. Henry, W. J. Stewart, R. J. Black, S. Lacroix, and F. Gonthier, "Tapered single-mode fibres and devices. Part 1: adiabaticity criteria," *IEE Proc.-J* **138**, 343–354 (1991).
31. I. F. Lealman, L. J. Rivers, M. J. Harlow, S. D. Perrin, and M. J. Robertson, "1.56 μm InGaAsP/InP tapered active layer multiquantum well laser with improved coupling to cleaved singlemode fiber," *Electron. Lett.* **30**, 857–859 (1994).
32. K. Kasaya, Y. Kondo, M. Okamoto, O. Mitomi, and M. Naganuma, "Monolithically integrated DBR lasers with simple tapered waveguide for low-loss fibre coupling," *Electron. Lett.* **29**, 2067–2068 (1993).
33. U. Koren, R. Benmichael, B. I. Miller, M. G. Young, M. Chien, H. H. Yaffe, G. Raybon, and K. Dreyer, "Electroabsorption modulator with passive waveguide spotsizer converters," *Electron. Lett.* **30**, 1852–1853 (1994).

34. N. Yoshimoto, K. Kawano, Y. Hasumi, H. Takeuchi, S. Kondo, and Y. Noguchi, "InGaAlAs/InAlAs multiple quantum well phase modulator integrated with spot size conversion structure," *IEEE Photon. Technol. Lett.* **6**, 208–210 (1994).
35. D. Sigogne, A. Ougazzaden, D. Meichenin, B. Mersali, A. Carencu, J. C. Simon, I. Valiente, C. Vassallo, and L. Billes, "1.55 μ m polarisation insensitive InGaAsP strained MQW optical amplifier integrated with short spot-size converters," *Electron. Lett.* **32**, 1403–1405 (1996).
36. A. S. Kewitsch, G. A. Rakuljic, P. A. Willems, and A. Yariv, "All-fiber zero-insertion-loss add-drop filter for wavelength-division multiplexing," *Opt. Lett.* **23**, 106–108 (1998).
37. K. Kawano, M. Kohtoku, N. Yoshimoto, S. Sekine, and Y. Noguchi, "2 \times 2 InGaAlAs/InAlAs multiquantum well (MQW) directional coupler waveguide switch modules integrated with spotsize converters," *Electron. Lett.* **30**, 353–355 (1994).
38. G. Roelkens, D. Van Thourhout, and R. Baets, "Coupling schemes for heterogeneous integration of III-V membrane devices and silicon-on-insulator waveguides," *J. Lightwave Technol.* **23**, 3827–3831 (2005).
39. R. Sun, M. Beals, A. Pomerene, J. Cheng, C. Y. Hong, L. Kimerling, and J. Michel, "Impedance matching vertical optical waveguide couplers for dense high index contrast circuits," *Opt. Express* **16**, 11682–11690 (2008).
40. M. Galarza, D. Van Thourhout, R. Baets, and M. Lopez-Amo, "Compact and highly-efficient polarization independent vertical resonant couplers for active-passive monolithic integration," *Opt. Express* **16**, 8350–8358 (2008).

41. S. G. Johnson, P. Bienstman, M. A. Skorobogatiy, M. Ibanescu, E. Lidorikis, and J. D. Joannopoulos, "Adiabatic theorem and continuous coupled-mode theory for efficient taper transitions in photonic crystals," *Phys. Rev. E* **66**, 066608 (2002).
42. F. Xia, V. M. Menon, and S. R. Forrest, "Photonic integration using asymmetric twin-waveguide (ATG) technology: part I—concepts and theory," *IEEE J. Sel. Top. Quantum Electron.* **11**, 17–29 (2005).
43. J. D. Love and W. M. Henry, "Quantifying loss minimisation in single-mode fibre tapers," *Electron. Lett.* **22**, 912–914 (1986).
44. T. Bakke, C. T. Sullivan, and S. D. Mukherjee, "Polymeric optical spot-size transformer with vertical and lateral tapers," *J. Lightwave Technol.* **20**, 1188–1197 (2002).
45. B. Hubner, G. Vollrath, R. Ries, C. Greus, H. Janning, E. Ronneberg, E. Kuphal, B. Kempf, R. Gobel, F. Fiedler, R. Zengerle, and H. Burkhard, "Laser diodes with integrated spot-size transformer as low-cost optical transmitter elements for telecommunications," *IEEE J. Sel. Top. Quantum Electron.* **3**, 1372–1383 (1997).
46. S. R. Park and B. H. O, "Novel design concept of waveguide mode adapter for low-loss mode conversion," *IEEE Photon. Technol. Lett.* **13**, 675–677 (2001).
47. A. Yariv, "Coupled-mode theory for guided-wave optics," *IEEE J. Quantum Electron.* **9**, 919–933 (1973).
48. G. Lifante, *Integrated Photonics: Fundamentals* (John Wiley & Sons, West Sussex, 2003).
49. X. K. Sun, A. Zadok, M. J. Shearn, K. A. Diest, A. Ghaffari, H. A. Atwater, A. Scherer, and A. Yariv, "Electrically pumped hybrid evanescent Si/InGaAsP lasers," *Opt. Lett.* **34**, 1345–1347 (2009).

50. X. K. Sun, M. J. Shearn, A. Zadok, M. S. Leite, S. T. Steger, H. A. Atwater, A. Scherer, and A. Yariv, "Electrically pumped supermode Si/InGaAsP hybrid lasers," in *Conference on Lasers and Electro-Optics/Quantum Electronics and Laser Science Conference (CLEO/QELS 2010)*, (OSA, San Jose, CA, USA, 2010), p. CTuO6.
51. C. E. Zah, R. Bhat, B. N. Pathak, F. Favire, W. Lin, M. C. Wang, N. C. Andreadakis, D. M. Hwang, M. A. Koza, T. P. Lee, Z. Wang, D. Darby, D. Flanders, and J. J. Hsieh, "High-performance uncooled 1.3 μm $\text{Al}_x\text{Ga}_y\text{In}_{1-x-y}\text{As}/\text{InP}$ strained-layer quantum-well lasers for subscriber loop applications," *IEEE J. Quantum Electron.* **30**, 511–523 (1994).
52. M. Fukuda, *Optical Semiconductor Devices* (Wiley, New York, NY, 1999), p. Chap. 7.
53. M. A. Parker, *Physics of Optoelectronics* (CRC Press, Boca Raton, FL, 2005).
54. A. Yariv, *Quantum Electronics*, 3rd ed. (Wiley, New York, 1989).
55. M. Shearn, X. K. Sun, M. D. Henry, A. Yariv, and A. Scherer, "Advanced plasma processing: etching, deposition, and wafer bonding techniques for semiconductor applications," in *Semiconductor Technologies*, J. Grym, ed. (Intech, 2010).
56. H. Boudinov, H. H. Tan, and C. Jagadish, "Electrical isolation of n -type and p -type InP layers by proton bombardment," *J. Appl. Phys.* **89**, 5343–5347 (2001).
57. M. Shearn, K. Diest, X. K. Sun, A. Zadok, H. Atwater, A. Yariv, and A. Scherer, "Advanced silicon processing for active planar photonic devices," *J. Vac. Sci. Technol. B* **27**, 3180–3182 (2009).
58. B. W. Hakki and T. L. Paoli, "cw degradation at 300 °K of GaAs double-heterostructure junction lasers. II. electronic gain," *J. Appl. Phys.* **44**, 4113–4119 (1973).

59. M. N. Sysak, H. Park, A. W. Fang, J. E. Bowers, R. Jones, O. Cohen, O. Raday, and M. Paniccia, "Experimental and theoretical thermal analysis of a hybrid silicon evanescent laser," *Opt. Express* **15**, 15041–15046 (2007).
60. K. Iga, "Surface-emitting laser—its birth and generation of new optoelectronics field," *IEEE J. Sel. Top. Quantum Electron.* **6**, 1201–1215 (2000).
61. T. Erdogan and D. G. Hall, "Circularly symmetric distributed feedback semiconductor laser: an analysis," *J. Appl. Phys.* **68**, 1435–1444 (1990).
62. T. Erdogan and D. G. Hall, "Circularly symmetric distributed feedback laser: coupled mode treatment of TE vector fields," *IEEE J. Quantum Electron.* **28**, 612–623 (1992).
63. C. Wu, M. Svilans, M. Fallahi, T. Makino, J. Glinski, C. Maritan, and C. Blaauw, "Optical pumped surface-emitting DFB GaInAsP/InP lasers with circular grating," *Electron. Lett.* **27**, 1819–1821 (1991).
64. C. Wu, M. Svilans, M. Fallahi, I. Templeton, T. Makino, J. Glinski, R. Maciejko, S. I. Najafi, C. Maritan, C. Blaauw, and G. Knight, "Room temperature operation of electrically pumped surface-emitting circular grating DBR laser," *Electron. Lett.* **28**, 1037–1039 (1992).
65. A. M. Shams-Zadeh-Amiri, X. Li, and W. P. Huang, "Above-threshold analysis of second-order circular-grating DFB lasers," *IEEE J. Quantum Electron.* **36**, 259–267 (2000).
66. A. M. Shams-Zadeh-Amiri, X. Li, and W. P. Huang, "Hankel transform-domain analysis of scattered fields in multilayer planar waveguides and lasers with circular gratings," *IEEE J. Quantum Electron.* **39**, 1086–1098 (2003).

67. A. Jebali, R. F. Mahrt, N. Moll, D. Erni, C. Bauer, G.-L. Bona, and W. Bachtold, "Lasing in organic circular grating structures," *J. Appl. Phys.* **96**, 3043–3049 (2004).
68. G. A. Turnbull, A. Carleton, A. Tahraoui, T. F. Krauss, I. D. W. Samuel, G. F. Barlow, and K. A. Shore, "Effect of gain localization in circular-grating distributed feedback lasers," *Appl. Phys. Lett.* **87**, 201101 (2005).
69. Y. Chen, Z. Li, Z. Zhang, D. Psaltis, and A. Scherer, "Nanoimprinted circular grating distributed feedback dye laser," *Appl. Phys. Lett.* **91**, 051109 (2007).
70. J. Scheuer and A. Yariv, "Coupled-waves approach to the design and analysis of Bragg and photonic crystal annular resonators," *IEEE J. Quantum Electron.* **39**, 1555–1562 (2003).
71. X. K. Sun, J. Scheuer, and A. Yariv, "Optimal design and reduced threshold in vertically emitting circular Bragg disk resonator lasers," *IEEE J. Sel. Top. Quantum Electron.* **13**, 359–366 (2007).
72. X. K. Sun, J. Scheuer, and A. Yariv, "Optimal design of vertically emitting circular Bragg disk resonator lasers," *Proc. SPIE* **6896**, 689604 (2008).
73. J. Scheuer, W. M. J. Green, G. A. DeRose, and A. Yariv, "InGaAsP annular Bragg lasers: theory, applications, and modal properties," *IEEE J. Sel. Top. Quantum Electron.* **11**, 476–484 (2005).
74. G. F. Barlow, A. Shore, G. A. Turnbull, and I. D. W. Samuel, "Design and analysis of a low-threshold polymer circular-grating distributed-feedback laser," *J. Opt. Soc. Am. B* **21**, 2142–2150 (2004).

75. X. K. Sun and A. Yariv, "Surface-emitting circular DFB, disk-, and ring- Bragg resonator lasers with chirped gratings: a unified theory and comparative study," *Opt. Express* **16**, 9155–9164 (2008).
76. X. K. Sun and A. Yariv, "Surface-emitting circular DFB, disk-, and ring- Bragg resonator lasers with chirped gratings. II: nonuniform pumping and far-field patterns," *Opt. Express* **17**, 1–6 (2009).
77. X. K. Sun and A. Yariv, "Surface-emitting circular DFB, disk-, and ring- Bragg resonator lasers with chirped gratings. III: gain saturation effects and above-threshold analysis," *Opt. Express* **17**, 10119–10125 (2009).
78. X. K. Sun and A. Yariv, "A unified theory for surface emitting chirped circular grating lasers," *Proc. SPIE* **7218**, 72180H (2009).
79. H. A. Haus, "Gain saturation in distributed feedback lasers," *Appl. Opt.* **14**, 2650–2652 (1975).
80. X. K. Sun and A. Yariv, "Modal properties and modal control in vertically emitting annular Bragg lasers," *Opt. Express* **15**, 17323–17333 (2007).
81. E. Hecht, *Optics*, 3rd ed. (Addison-Wesley, 1998).
82. R. H. Jordan, D. G. Hall, O. King, G. Wicks, and S. Rishton, "Lasing behavior of circular grating surface-emitting semiconductor lasers," *J. Opt. Soc. Am. B* **14**, 449–453 (1997).
83. M. Fallahi, M. Dion, F. Chatenoud, I. M. Templeton, R. Barber, and J. Sedivy, "Low threshold CW operation of circular-grating surface-emitting DBR lasers using MQW and a self-aligned process," *IEEE Photon. Technol. Lett.* **6**, 1280–1282 (1994).

84. A. Jebali, D. Erni, S. Gulde, R. F. Mahrt, and W. Bachtold, "Analytical calculation of the Q factor for circular-grating microcavities," *J. Opt. Soc. Am. B* **24**, 906–915 (2007).
85. R. Coccioli, M. Boroditsky, K. W. Kim, Y. Rahmat-Samii, and E. Yablonovitch, "Smallest possible electromagnetic mode volume in a dielectric cavity," *IEE Proc.-Optoelectron.* **145**, 391–397 (1998).
86. C. Olson, P. L. Greene, G. W. Wicks, D. G. Hall, and S. Rishton, "High-order azimuthal spatial modes of concentric-circle-grating surface-emitting semiconductor lasers," *Appl. Phys. Lett.* **72**, 1284–1286 (1998).
87. C. Wu, T. Makino, M. Fallahi, R. G. A. Craig, G. Knight, I. Templeton, and C. Blauw, "Novel circular grating surface-emitting lasers with emission from center," *Jpn. J. Appl. Phys.* **33-Pt. 2**, L427–L429 (1994).
88. P. L. Greene and D. G. Hall, "Effects of radiation on circular-grating DFB lasers—part II: device and pump-beam parameters," *IEEE J. Quantum Electron.* **37**, 364–371 (2001).
89. K. J. Kasunic, E. M. Wright, and N. Peyghambarian, "Numerical modeling of inhomogeneously-pumped circular-grating DFB lasers," *Proc. SPIE* **2398**, 125–134 (1995).
90. J. Scheuer, W. M. Green, G. DeRose, and A. Yariv, "Ultra-sensitive biochemical sensor based on circular Bragg micro-cavities," in *Conference on Lasers and Electro-Optics/Quantum Electronics and Laser Science and Photonic Applications Systems Technologies*, (Optical Society of America, Baltimore, MD, 2005), p. CPDA7.
91. J. Scheuer, "Direct rotation-induced intensity modulation in circular Bragg micro-lasers," *Opt. Express* **15**, 15053–15059 (2007).

92. U. Brauch, P. Loosen, and H. Opower, "High-Power Diode Lasers for Direct Applications," in *High-Power Diode Lasers: Fundamentals, Technology, Applications*, R. Diehl, ed. (Springer, Berlin/Heidelberg, 2000), pp. 303–368.
93. A. W. Snyder and J. D. Love, *Optical Waveguide Theory* (Chapman and Hall, New York, 1983).